Rapid Prediction of Tsunamis and Storm Surges Using Machine Learning

Jun-Whan (Michael) Lee

Dissertation submitted to the Faculty of the
Virginia Polytechnic Institute and State University
in partial fulfillment of the requirements for the degree of

Doctor of Philosophy
in
Civil Engineering

Jennifer L. Irish, Chair
Kyle B. Strom
Nina Stark
Robert Weiss

April 7, 2021
Blacksburg, Virginia

Keywords: Tsunami, Storm Surge, Surrogate Modeling, Response Surface Methodology, Convolutional Neural Network, Earthquake, Tropical Cyclone, Coastal Resilience

Rapid Prediction of Tsunamis and Storm Surges Using Machine Learning

Jun-Whan (Michael) Lee

ABSTRACT

Tsunami and storm surge are two of the main destructive and costly natural hazards faced by coastal communities around the world. To enhance coastal resilience and to develop effective risk management strategies, accurate and efficient tsunami and storm surge prediction models are needed. However, existing physics-based numerical models have the disadvantage of being difficult to satisfy both accuracy and efficiency at the same time. In this dissertation, several surrogate models are developed using statistical and machine learning techniques that can rapidly predict a tsunami and storm surge without substantial loss of accuracy, with respect to high-fidelity physics-based models. First, a tsunami run-up response function (TRRF) model is developed that can rapidly predict a tsunami run-up distribution from earthquake fault parameters. This new surrogate modeling approach reduces the number of simulations required to build a surrogate model by separately modeling the leading order contribution and the residual part of the tsunami run-up distribution. Secondly, a TRRF-based inversion (TRRF-INV) model is developed that can infer a tsunami source and its impact from tsunami run-up records. Since this new tsunami inversion model is based on the TRRF model, it can perform a large number of tsunami forward simulations in tsunami inversion modeling, which is impossible with physics-based models. And lastly, a one-dimensional convolutional neural network combined with principal component analysis and k-means clustering (C1PKNet) model is developed that can rapidly predict the peak storm surge from tropical cyclone track time series. Because the C1PKNet model uses the

tropical cyclone track time series, it has the advantage of being able to predict more diverse tropical cyclone scenarios than the existing surrogate models that rely on a tropical cyclone condition at one moment (usually at or near landfall). The surrogate models developed in this dissertation have the potential to save lives, mitigate coastal hazard damage, and promote resilient coastal communities.

Rapid Prediction of Tsunamis and Storm Surges Using Machine Learning

Jun-Whan (Michael) Lee

GENERAL AUDIENCE ABSTRACT

Tsunami and storm surge can cause extensive damage to coastal communities; to reduce this damage, accurate and fast computer models are needed that can predict the water level change caused by these coastal hazards. The problem is that existing physics-based computer models are either accurate but slow or less accurate but fast. In this dissertation, three new computer models are developed using statistical and machine learning techniques that can rapidly predict a tsunami and storm surge without substantial loss of accuracy compared to the accurate physics-based computer models. Three computer models are as follows: (1) A computer model that can rapidly predict the maximum ground elevation wetted by the tsunami along the coastline from earthquake information, (2) A computer model that can reversely predict a tsunami source and its impact from the observations of the maximum ground elevation wetted by the tsunami, (3) A computer model that can rapidly predict peak storm surges across a wide range of coastal areas from the tropical cyclone's track position over time. These new computer models have the potential to improve forecasting capabilities, advance understanding of historical tsunami and storm surge events, and lead to better preparedness plans for possible future tsunamis and storm surges.

Acknowledgments

I would like to express my sincere gratitude to my advisor Dr. Jennifer Irish for providing me with the opportunity to obtain this degree and for granting me sufficient flexibility to pursue various research ideas during my Ph.D. study. I also appreciate her invaluable guidance, unwavering support, and encouragement throughout this process. The quality of this dissertation work has significantly benefited from her input.

My sincere thanks must also go to my committee members: Dr. Kyle Strom, Dr. Nina Stark, and Dr. Robert Weiss. They generously took their time to offer me valuable comments on improving my dissertation work.

I would also like to thank Mr. Doug Marcy (NOAA Office for Coastal Management) and Dr. Michelle Bensi (University of Maryland) for their thoughtful discussions and suggestions regarding my work.

This dissertation would not have been possible without the support of colleagues and friends in the Coastal Hazards group, the Department of Civil and Environmental Engineering, the New Horizon Graduate Scholars program, and the Advanced Research Computing at Virginia Tech. I also want to thank the Disaster Resilience and Risk Management program at Virginia Tech for opening my eyes to the world of interdisciplinary research and for inspiring me to step out of my comfort zone and to expand research horizons. I thank Virginia Sea Grant for financially supporting my research as well as for providing me with various professional development opportunities.

Finally, my deepest gratitude goes to my family. Their tremendous understanding, encouragement, and love have made this study possible.

Contents

List of Figures

List of Tables

Chapter 1

Introduction

1.1 Background and motivation

Tsunami and storm surge are destructive and costly natural hazards for coastal communities around the world. The 2004 Indian Ocean tsunami and the 2011 Tohoku tsunami, which caused more than 225,000 and 19,800 fatalities and more than $9.9 billion and $210 billion in losses, respectively, are prime examples of how tsunamis can cause extensive damage to coastal communities [140, 148]. Hurricane Katrina (2005), which generated storm surge exceeding 7.5 m above sea level, is recorded as the costliest natural hazard in U.S. history, causing about 2,000 fatalities and at least $170 billion in losses [10, 103]. Over the past decade, interest in sustainable development for socioeconomic and cultural resources in coastal areas has grown as not only the coastal hazards have been increasing in their frequency and destruction but also human activity in coastal areas has expanded [29]. To enhance coastal resilience and to develop effective risk management strategies, several studies have emphasized the need for a rapid and accurate model that can support not only a probabilistic forecast but also a probabilistic hazard assessment where a large number of simulations is required to account for the uncertainty in hazard characterization [22, 39, 115, 125].

Physics-based numerical models have been widely developed to predict tsunamis and storm surges [e.g., 60, 86, 88, 112]. Significant advances in physics-based numerical models over the last several decades allow accurate simulation at high resolution. The problem, how-

ever, is that high-fidelity physics-based models are computationally intensive, even though several computational techniques are employed to improve the efficiency, such as adaptive mesh refinement and parallelization. Due to the computational burden of the high-fidelity physics-based model, tsunami/storm surge forecasting and hazard assessment are performed as follows:

- For tsunami forecasting, a pre-computed simulation database, which can rapidly provide tsunami information once the earthquake occurs, is widely used around the world [e.g., 6, 15, 141]. The problem, however, is that the tsunami prediction can have substantial errors in real-world scenarios that do not exist in the database. For storm surge forecasting, the National Hurricane Center's operational probabilistic forecast system (P-Surge) relies on a large number of coarse-grid simulations based on a low-fidelity model that neglects key physical components such as waves and nonlinear advection [66].

- Most of the probabilistic tsunami hazard assessments rely on a logic-tree approach, which limits the number of scenarios based on historical earthquake records, but requires expert judgment, which is difficult to justify reliability [e.g., 37, 107]. Most of the probabilistic storm surge hazard assessments have been relying on a large number of simulations based on low-fidelity models [e.g., 82] or only on a few simulations based on high-fidelity models [e.g., 70].

- To better understand a tsunami source, which is vital to assess a tsunami hazard, several tsunami inversion models have been developed that can infer a tsunami source from measured data such as seismic waveform and tide gauge data [e.g. 53, 75]. However, tsunami run-up records have not been widely used because they require many high-fidelity simulations to find a tsunami source that best matches the tsunami run-

up records. Thus, the tsunami inversion models based on tsunami run-up records have relied on a large number of simulations based on low-fidelity models [33, 111] or only on a few simulations based on high-fidelity models [87].

Data-driven surrogate modeling based on the high-fidelity simulation database is an effective way to complement the complex physics-based models to reduce the computational burden. The surrogate models are usually called black-box models because they find a relationship between input and output without knowing any mechanism of a physics-based model [45]. Several statistical and machine learning techniques can be used to develop a surrogate model, such as response surface methodology, kriging, and artificial neural network. Every method follows the same procedure: (1) selection of input/output, (2) optimization of model parameters, and (3) evaluation of the accuracy of a surrogate model. Once the surrogate model is trained to represent the input/output relationship of the limited number of high-fidelity simulations, the output can be rapidly estimated across the continuum of input spaces.

However, the surrogate model has not been widely developed to predict a tsunami because of the high-dimensional input that requires a large number of simulations to apply a surrogate modeling approach. In tsunami modeling, the input is usually represented by nine earthquake fault parameters: epicenter latitude, epicenter longitude, fault length, fault width, fault depth, strike angle, dip angle, rake angle, and slip. For this reason, several studies have only considered a few fault parameters while fixing the other parameters in surrogate modeling [69, 118]. On the other hand, the storm surge model's input dimensionality is relatively smaller than that of the tsunami model. In storm surge modeling, the input is usually represented by six tropical cyclone parameters: latitude, longitude, heading direction, central pressure, radius of maximum winds, and translation speed. Moreover, several studies have developed a high-fidelity simulation database based on systemically designed synthetic tropical cyclone scenarios over the last decade [e.g., 20, 58, 65]. For this reason, there are relatively more

studies that applied the surrogate modeling approach in storm surge research compared to tsunami research [e.g., 9, 61, 62, 72, 134, 135, 154]. However, none of the studies has incorporated the variation of tropical cyclone conditions over time in surrogate modeling. Instead, the previous studies relied on a tropical cyclone condition at one moment (usually at or near landfall), which is not always most correlated with the peak storm surge.

1.2 Goal and objectives

This dissertation's overarching goal is to develop new surrogate models that can rapidly predict a tsunami and storm surge to overcome the limitations of existing tsunami and storm surge surrogate models. The specific objectives are to:

- Develop a new methodology that can reduce the input dimensionality in tsunami surrogate modeling, and apply the new surrogate modeling approach to northern Puerto Rico, where a significant tsunami generated by an earthquake along the Puerto Rico Trench could devastate coastal communities on the northern shore, especially socially vulnerable populations (Chapter 2).

- Develop a new tsunami inversion model that can infer a tsunami source and its impact from tsunami run-up records using surrogate modeling, and apply the new surrogate modeling approach to the northern Chile coastal region that is exposed to significant tsunami risk considering its inhabitants and critical coastal infrastructures (Chapter 3).

- Develop a new surrogate model incorporating the variation of tropical cyclone conditions that can rapidly predict peak storm surge, and develop a web mapping application to raise the communities' awareness of storm surge hazard and to support decision and policy makers (Chapter 4).

1.3 Attribution

In this manuscript-based dissertation, authors and affiliations are listed at the beginning of each chapter. Here, the author's contributions are summarized as follows.

- For Chapter 2 and Chapter 3, Jun-Whan Lee designed the details of the methodology, performed the research, analyzed the data, and drafted the manuscript. Dr. Jennifer Irish and Dr. Robert Weiss conceptualized the research, provided overall guidance on research direction, and contributed to manuscript preparation.

- For Chapter 4, Jun-Whan Lee conceptualized the research, designed the details of the methodology, performed the research, analyzed the data, and drafted the manuscript. Dr. Jennifer Irish conceptualized the research, provided overall guidance on research direction, and contributed to manuscript preparation. Dr. Michel Bensi proposed a method to analyze the results and contributed to the writing of the manuscript. Mr. Doug Marcy provided feedback on the web mapping application and contributed to manuscript preparation.

Chapter 2

Rapid prediction of alongshore run-up distribution from near-field tsunamis

Jun-Whan Lee [1], Jennifer L. Irish [1,3], Robert Weiss [2,3]

[1] Department of Civil and Environmental Engineering, Virginia Tech, 750 Drillfield Dr, Blacksburg, VA, 24061, USA

[2] Department of Geosciences, Virginia Tech, 926 W Campus Dr, Blacksburg, VA, 24061, USA

[3] Center for Coastal Studies, Virginia Tech, 926 W Campus Dr, Blacksburg, VA 24061, USA

2.1 Abstract

Rapid prediction of the spatial distribution of the run-up from near-field tsunamis is critically important for tsunami hazard characterization. Even though significant advances have been made over the last decade, physics-based numerical models are still computationally intensive. Here, we present a response surface methodology (RSM)-based model called the tsunami run-up response function (TRRF). Derived from a discrete set of tsunami simulations, TRRF can produce a rapid prediction of a near-field tsunami run-up distribution that takes into account the influence of variable local topographic and bathymetric characteristics in a given region. This new method reduces the number of simulations required to build an RSM model by separately modeling the leading order contribution and the residual part of the tsunami run-up distribution. Using the northern region of Puerto Rico as a case study, we investigated the performance (accuracy, computational time) of the TRRF. The results reveal that the TRRF achieves reliable prediction while reducing the prediction time by six orders of magnitude (computational time: < 1 *second* per earthquake).

2.2 Introduction

Tsunamis are some of the most destructive and costly natural hazards for coastal areas around the world. The 2004 Indian Ocean tsunami and the 2011 Tohoku tsunami are prime examples of how tsunamis can cause extensive damage to coastal communities, especially in near-field areas [140, 148]. A near-field tsunami, which is a tsunami generated close to the coastline, involves a high risk for coastal communities because the first waves can arrive on shore in minutes [97]. To mitigate damage and build resilient coastal communities, it is critically important to develop rapid prediction capacities for a near-field tsunami run-up

distribution along the coastlines. Physics-based numerical simulation is currently the most accurate method for predicting a tsunami run-up distribution. Though significant advances have been made over the last decade [78, 83, 112, 129], these physics-based numerical models still remain time consuming. For example, robust probabilistic tsunami hazard assessment (PTHA) requires tsunami run-up estimates for a large number of scenarios to allow for accurate quantification of the hazard and related uncertainty [91]. However, due to the computational burden associated with physics-based numerical simulation, a logic-tree approach is typically employed: it limits the number of scenarios based on historical earthquake characteristics (e.g., magnitude, recurrence interval) used to evaluate uncertainty in tsunami hazard [5, 108, 109]. The issue with the logic-tree approach is that it relies on expert judgment, which is difficult to quantify reliability. On the other hand, to carry out a large number of scenario simulations, several studies applied an amplification factor method that can rapidly estimate the maximum inundation height from the simulated offshore tsunami amplitude [26, 40]. However, limitations of the amplification factor approach are that the choice of the offshore reference point is somewhat subjective and that the approach still requires numerical simulation to obtain offshore tsunami amplitude. The computational burden associated with physics-based numerical simulation—especially for near-field tsunami forecasting—is a major obstacle. For this reason, pre-computed simulation databases are widely used. These databases can provide fast prediction by selecting the best-matched simulation or by interpolating between simulations immediately after the source mechanism is known [63, 92, 126]. A problem with the database approach is that it can have substantial errors in real-world scenarios that do not exist in the selected databases.

The response surface methodology (RSM) is an effective statistical-based approach for establishing a relationship between a set of input variables and the output of a system [12, 93]. Once the RSM model is built, output can be rapidly estimated across the continuum of input

spaces. However, because high-dimensional input requires a large number of simulations—which is prohibitively expensive—the RSM has not been used to predict a tsunami run-up distribution. For example, a tsunamigenic-earthquake (the input in an RSM model) is usually represented by nine fault parameters (Fig. 2.1). A full factorial design is one of the most widely employed designs of experiments (DoE) used to measure the response of every possible combination of independent variables. If we design the synthetic tsunami scenarios using a three-level full factorial approach with nine fault parameters, 19,683 ($= 3^9$) simulations are required. Moreover, if the input/output relationship shows large nonlinearity, a higher level of DoE may be needed, which would necessitate exponentially more simulations.

Here, we present a new methodology to rapidly predict the near-field tsunami run-up distribution: the tsunami run-up response function (TRRF). It is based on RSM but requires only 729 ($= 3^6$) simulations through reducing input dimensionality. Input dimensionality is reduced through a decomposition of the leading order tsunami run-up contribution and the residual part of the run-up distribution. We demonstrated the TRRF approach in northern Puerto Rico, where a significant tsunami generated by an earthquake along the Puerto Rico Trench could devastate coastal communities on the northern shore [43, 85, 114] (Fig. 2.2).

2.3 Tsunami run-up response function (TRRF)

The main concept of TRRF is to decompose the tsunami run-up distribution $R(x)$ into source run-up $S(x)$ and topographic run-up $T(x)$ (Fig. 2.3):

$$R(x) = S(x) + T(x) \tag{2.1}$$

where the x-axis is parallel to the coastline.

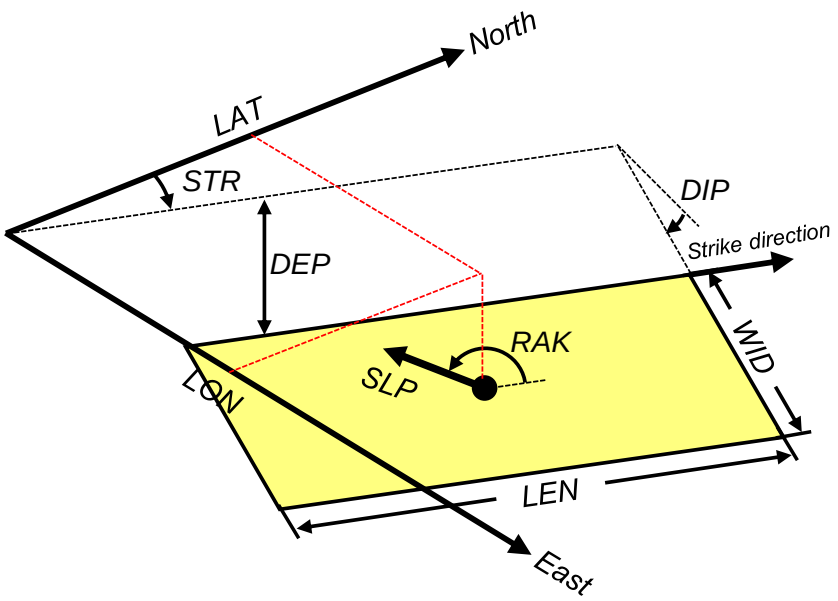

Figure 2.1: Schematic sketch of earthquake fault parameters: epicenter latitude (LAT), epicenter longitude (LON), fault length (LEN), fault width (WID), top-edge fault depth (DEP), strike angle (STR), dip angle (DIP), rake angle (RAK), and slip (SLP).

The source run-up $S(x)$ is a leading order contribution that can be represented by Okal and Synolakis [105]'s empirical formula (hereafter OS formula):

$$S(x) = \frac{b}{\left[\frac{x-c}{a}\right]^2 + 1} \tag{2.2}$$

where the coefficient a is related to the width of the source run-up, b is the maximum source run-up, and c is the distance from the x-axis origin to the location of the maximum source run-up.

The topographic run-up $T(x)$ is the residual run-up remaining after subtracting $S(x)$ from $R(x)$. It represents the local (de)amplification of the incoming tsunami wave and the resulting run-up arising from topographic variation. The $T(x)$ can be normalized as follows,

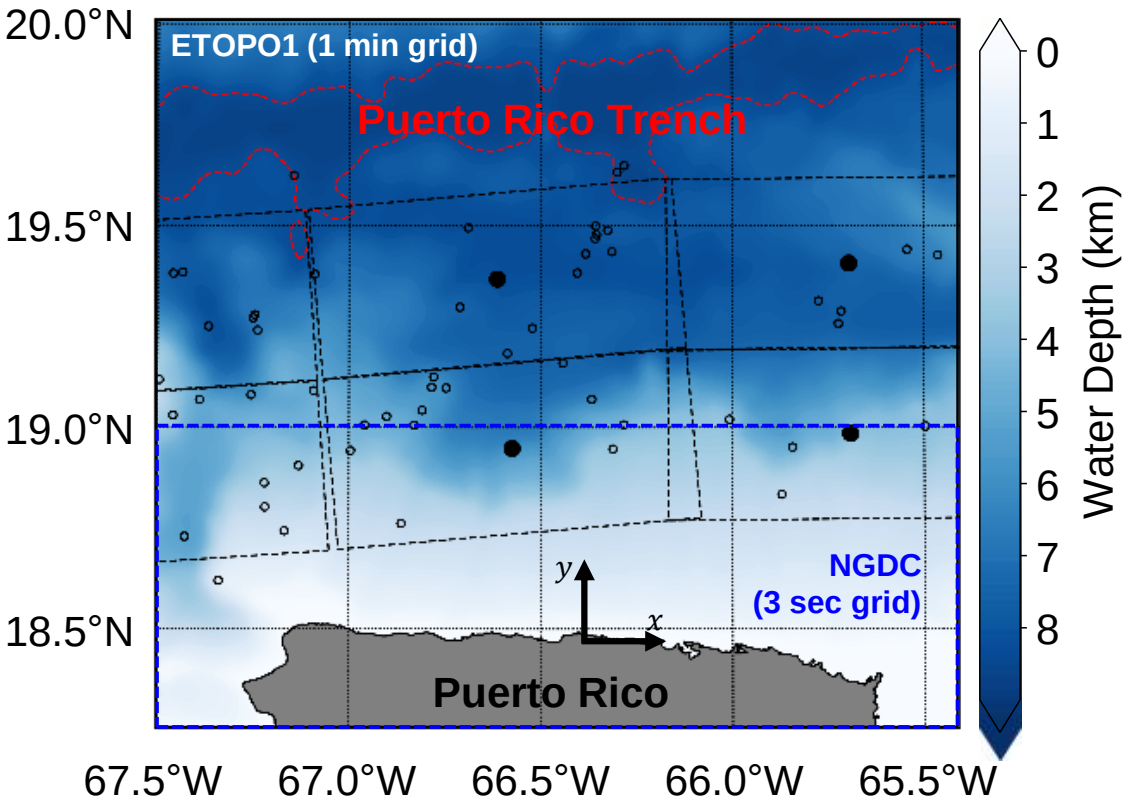

Figure 2.2: Map of northern Puerto Rico. Open black circles represent the epicenters of historical earthquakes ($M_w \geq 4.5$, [145]). The filled black circles and dashed black lines represent the epicenters of NOAA's pre-defined unit sources and fault orientation, respectively (Gica, 2008). The dashed red line represents the contour line where the water depth is 8 km. The blue dashed square represents the region where the National Geophysical Data Center (NGDC)'s 3-second topographic grid [100] is used for numerical simulation.

hereafter called normalized topographic run-up $NT(x)$.

$$NT(x) = \frac{T(x)}{S(x)} \tag{2.3}$$

The default axis of the TRRF approach is oriented as follows: x-axis is east-west direction (x_E) and y-axis is north-south direction (y_N). Thus, if the coastline is not aligned east-west, the axis should be rotated based on the east-west direction until the x-axis is parallel to the

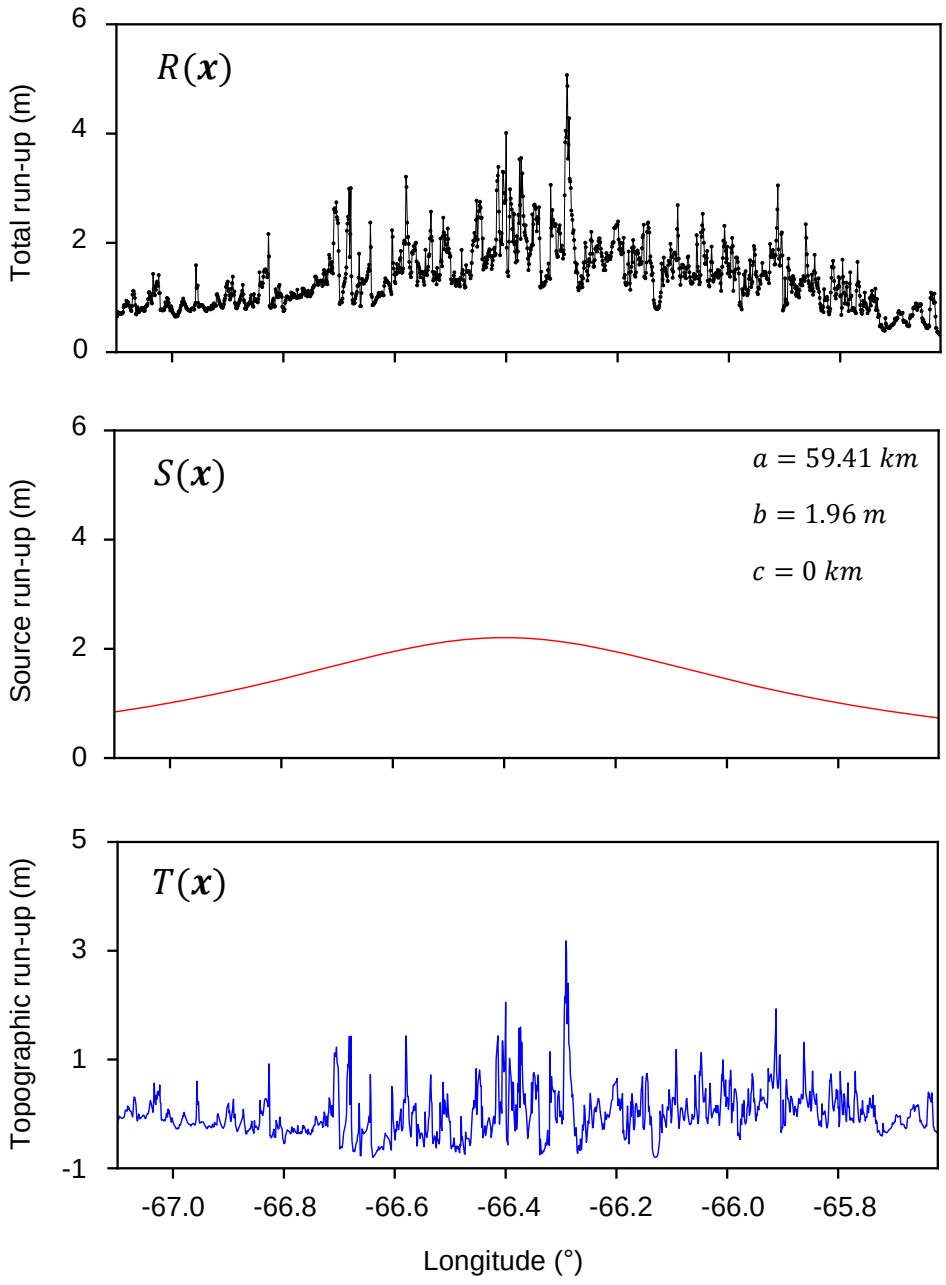

Figure 2.3: Example of (a) tsunami run-up distribution, (b) source run-up, and (c) topographic run-up. The fault parameter condition is as follows: $LON = 66.4°W$, $LAT = 19.3°N$, $STR = 90°$, $DIP = 20°$, $RAK = 90°$, $LEN = 90\ km$, $WID = 40\ km$, $SLP = 2\ m$, $DEP = 30\ km$. The a, b and c on the second panel are the coefficients of the OS formula (Eq. 2.2).

coastline as follows:

$$x = x_E \cos\delta + y_N \sin\delta \tag{2.4}$$

$$y = -x_E \sin\delta + y_N \cos\delta \tag{2.5}$$

where δ is an angle between the east-west direction and the coastline in a counterclockwise direction from East, x is a rotated x-axis, and y is a rotated y-axis. Also, the TRRF approach is defined based on a Cartesian coordinate system while the epicenters are defined in a spherical coordinate system. To align the coordinate systems, the unit of the epicenter should be converted from degrees (LON, LAT) to kilometers (X, Y) where X is shortest distance from the rotated y-axis to the epicenter and Y is shortest distance from the rotated x-axis to the epicenter.

Based on the main concept, the TRRF can predict a tsunami run-up distribution $R^p(x)$ by putting the source run-up $S^p(x)$ and the normalized topographic run-up $NT^p(x)$ (where superscript p represents prediction) to the following equation:

$$R^p(x) = S^p(x)\,[1 + NT^p(x)] \tag{2.6}$$

where $NT^p(x)$ is the 50th percentile (or median) of $NT(x)$ among all the simulations used to build the TRRF. Note that the $NT^p(x)$ is independent of the earthquake fault parameters. The source run-up $S^p(x)$ can be estimated by inputting the OS formula coefficients a, b, and c into Eq. 2.2. The RSM approach is applied to estimate the OS formula coefficients a and b from six parameters (hereafter RSM parameters):

$$a = f_a(Y, LEN, WID, DIP, SLP, DEP) \tag{2.7}$$

$$b = f_b(Y, LEN, WID, DIP, SLP, DEP) \tag{2.8}$$

where f_a and f_b are the best-fitting curves to these coefficients; hereafter, these curves are called RSM functions. Since the RSM function inputs consist of six parameters, 729 ($= 3^6$) simulations are required to derive RSM functions following a three-level full factorial design.

The epicenter location along the x-axis, X, is excluded in the RSM function inputs because x-axis runs parallel to the coastline. In this condition, the coefficients a and b are independent of X, and the coefficient c is equal to X by the definition of the OS formula (see Eq. 2.2):

$$c = X \tag{2.9}$$

The strike angle STR and rake angle RAK are also not included in the RSM function inputs because the OS formula [105] is only applicable to an earthquake fault oriented in shore-parallel strike direction with 90° rake angle. Since this is not the only case that occurs in nature, we developed a method that can represent a fault where strike direction is not parallel to the coastline and rake angle is not 90° as a series of hypothetical faults where the strike direction is parallel to the coastline and the rake angle is 90°, hereafter called the angle projection (AP) method.

Section 2.3.1 will describe the procedures of building a TRRF. Section 2.3.2 will explain the AP method and Section 2.3.3 will describe the procedures of predicting a tsunami run-up distribution once the TRRF is built.

2.3.1 TRRF development

Fig. 2.4 shows the procedure of TRRF development. The first step is to simulate 729 tsunamigenic-earthquake scenarios using a physics-based numerical model. The second step is to extract the run-up and apply the OS formula (Eq. 2.2) to obtain the normalized

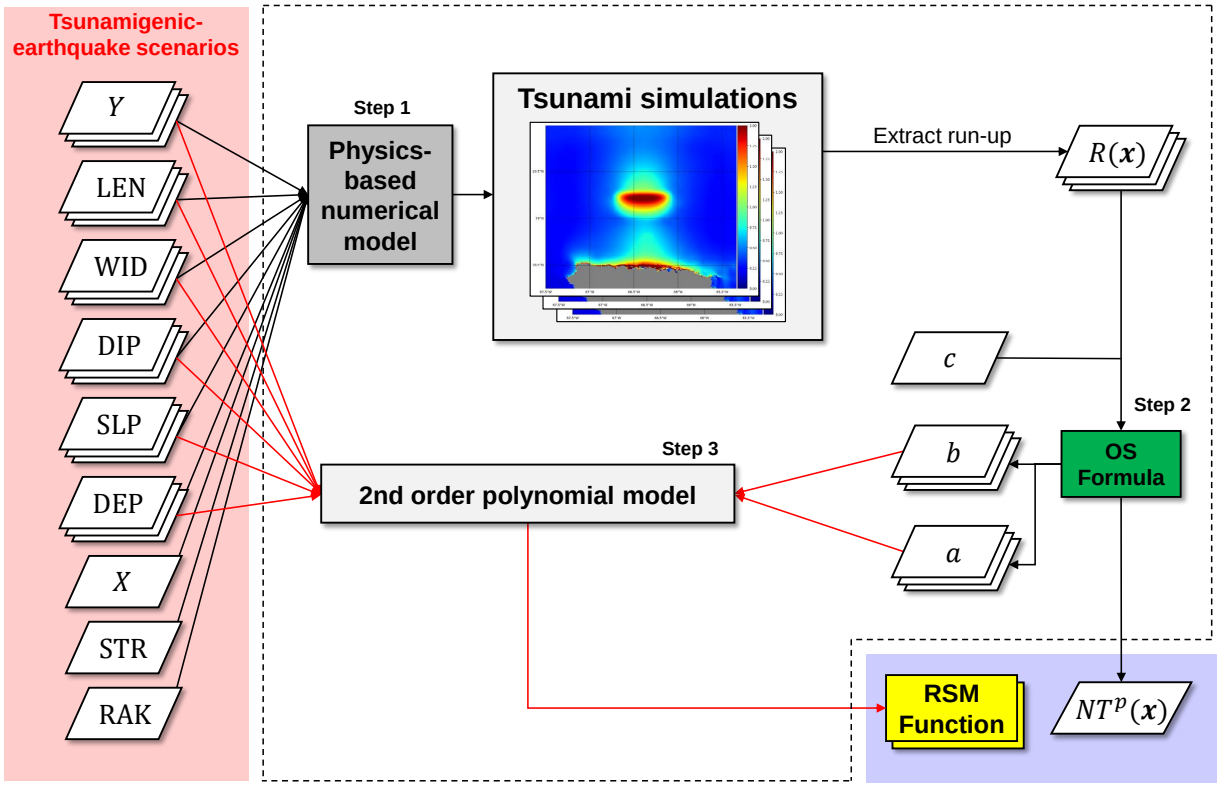

Figure 2.4: Computational flow of TRRF development. The inputs, the processing steps, and the outputs are represented in light red box, white dashed box, and light blue box, respectively. The red lines represent the process where the response surface methodology (RSM) approach is applied.

topographic run-up $NT^p(x)$ (Eq. 2.3). The last step is to fit the earthquake fault parameters and the OS formula coefficients (a and b) to the 2nd order polynomial model to obtain the RSM functions (Eqs. 2.7 and 2.8). Once the $NT^p(x)$ and the RSM functions are derived, this procedure does not have to be repeated to predict the tsunami run-up distribution.

2.3.2 Angle projection (AP) method

The AP method comprises three steps: adjustment of strike angle and rake angle, fault rotation, and decomposition of slip.

Adjustment of strike angle and rake angle

The direction of near-field tsunami propagation is related to the interaction between the strike angle STR and the rake angle RAK. To consider the interaction between STR and RAK, the first step involves adjusting the STR and the RAK as follows (Fig. 2.5):

$$\theta = \alpha[f_{AP}(STR, \delta) - 90^\circ] + 90^\circ + \beta(RAK - 90^\circ) \tag{2.10}$$

$$\lambda = \gamma(RAK - 90^\circ) + 90^\circ \tag{2.11}$$

where θ is the adjusted strike angle ($0 < \theta < 180$) and λ is the adjusted rake angle ($0 < \lambda < 180$) based on the rotated axes. The α, β, and γ are the site-specific coefficients that should be calibrated in advance (see Section 2.5). The f_{AP} is a function of STR ($0^\circ - 360^\circ$) and δ ($0^\circ - 360^\circ$) defined as follows:

$$f_{AP}(STR, \delta) = \begin{cases} STR + \delta, \ 0^\circ \leq STR + \delta < 360^\circ \\ STR + \delta - 360^\circ, \ 360^\circ \leq STR + \delta \end{cases} \tag{2.12}$$

Fault rotation

If the adjusted strike direction is parallel to the coastline ($\theta = 90^\circ$) and the adjusted rake angle λ is 90°, the maximum source run-up will be located at the epicenter location along the x-axis, X. On the other hand, if the adjusted strike direction is not parallel to the coastline ($\theta \neq 90^\circ$), the location of the maximum source run-up will be shifted to a direction perpendicular to the adjusted strike direction. To consider the location of the maximum source run-up depending on the adjusted strike angle, the second step involves rotating the

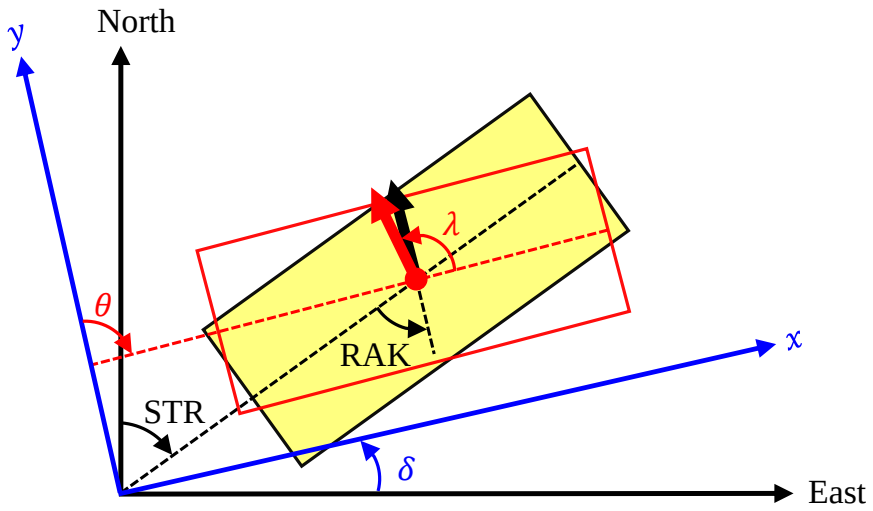

Figure 2.5: Schematic sketch of step 1 of AP method. The yellow-filled rectangle is the original fault where STR is strike angle and RAK is rake angle. The red rectangle represents the adjusted fault where θ is the adjusted strike angle and λ is the adjusted rake angle based on the rotated axis (blue). The arrows represent the slip direction.

adjusted fault ($\theta \neq 90°$) until θ becomes 90° (Fig. 2.6). The epicenter of the rotated fault (X_1^p, Y_1^p) can be calculated as follows:

$$X_1^p = X + \frac{Y}{tan\ (\theta)} \tag{2.13}$$

$$Y_1^p = \frac{Y}{|sin\ (\theta)|} \tag{2.14}$$

Decomposition of slip

If the adjusted rake angle λ is not 90°, the run-up will be spread in the slip direction. To consider the spread of run-ups depending on the adjusted rake angle, the third step involves representing the rotated fault ($\lambda \neq 90°$) as a series of hypothetical faults having slips perpendicular to the coastline ($\lambda = 90°$) (Fig. 2.7). Since the tsunami energy is

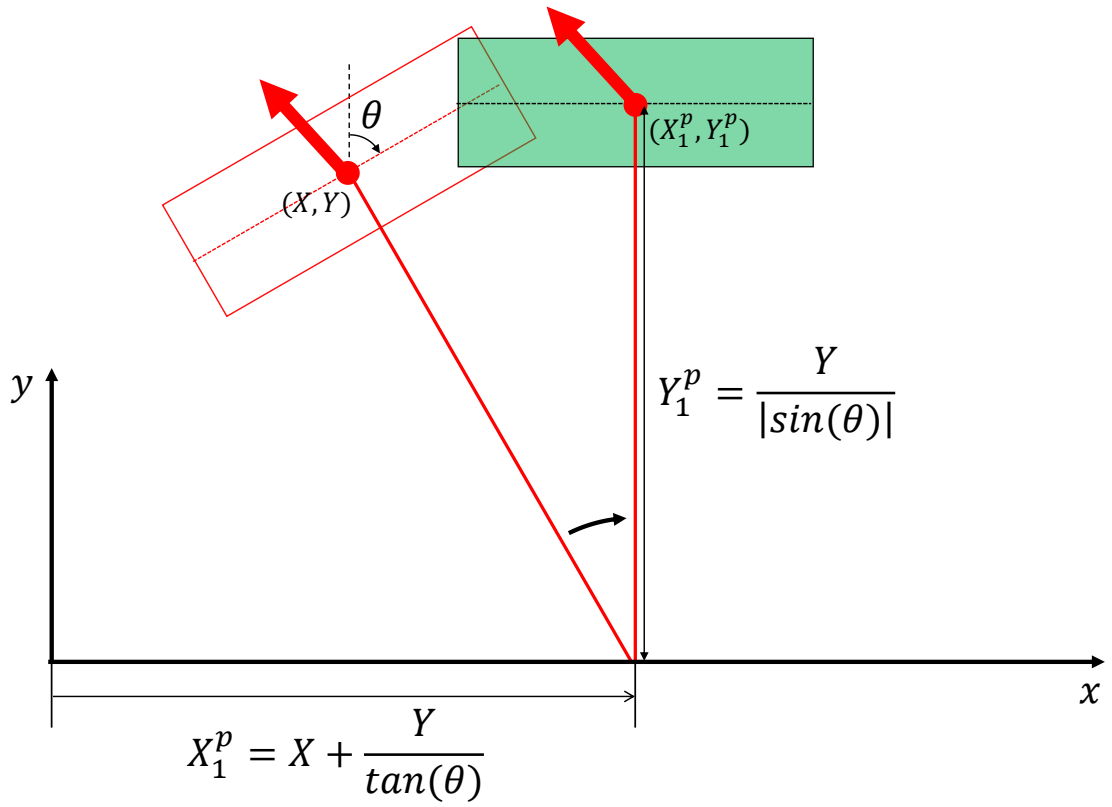

Figure 2.6: Schematic sketch of step 2 of AP method. The red rectangle is the adjusted fault where the epicenter is $(X,\ Y)$. The green rectangle represents the rotated fault where the epicenter is $(X_1^p,\ Y_1^p)$. The two red lines are of the same length. One line is perpendicular to the strike direction spanning from the epicenter of the adjusted fault to the point where it meets the coastline. The other line is the vertical distance from the epicenter of the rotated fault to the coastline.

proportional to SLP, we assume that the source run-up will be spread proportionally to a component of SLP parallel to the coastline. Based on this assumption, while the LEN, WID, DEP, and DIP are identical to the original fault, the epicenter (X_i^p, Y_i^p) and SLP_i^p of the ith hypothetical fault ($i = 1, 2...n$) are defined as follows:

$$X_i^p = X_1^p + \frac{X_n^p - X_1^p}{n-1}(i-1) \tag{2.15}$$

$$Y_i^p = Y_1^p + \frac{Y_n^p - Y_1^p}{n-1}(i-1) \tag{2.16}$$

$$SLP_i^p = SLP_1^p + \frac{SLP_n^p - SLP_1^p}{n-1}(i-1) \tag{2.17}$$

where n is the total number of hypothetical faults, which should be calibrated in advance (see Section 2.5). The SLP_1^p and SLP_n^p are the slips of the first and last hypothetical faults, respectively, defined as follows:

$$SLP_1^p = SLP|sin(\lambda)| \tag{2.18}$$

$$SLP_n^p = SLP|cos\ (\lambda)| \tag{2.19}$$

The (X_n^p, Y_n^p) are the epicenter of the last hypothetical fault and can be calculated based on a geometric setup (see two red lines in Fig. 2.7):

$$X_n^p = X_1^p - \frac{Y_1^p}{tan(\lambda)} \tag{2.20}$$

$$Y_n^p = \frac{Y_1^p}{|sin\ (\lambda)|} \tag{2.21}$$

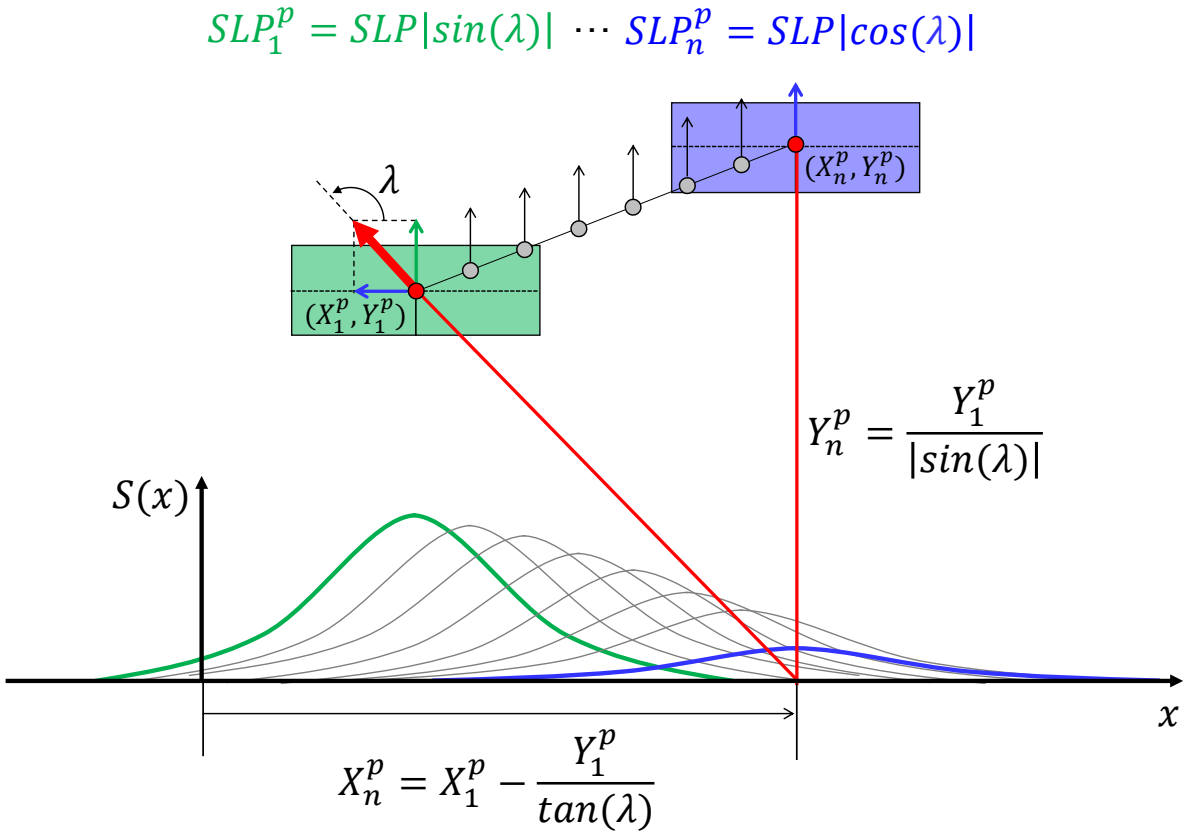

Figure 2.7: Schematic sketch of step 3 of AP method. The green rectangle represents the first hypothetical fault where the epicenter is (X_1^p, Y_1^p) and the slip is SLP_1^p. The blue rectangle represents the last hypothetical fault among a series of hypothetical faults where the epicenter is (X_n^p, Y_n^p) and slip is SLP_n^p. Gray circles and arrows represent the epicenters and the slips of the hypothetical faults, respectively; these are linearly distributed between the first hypothetical fault and the last hypothetical fault. Two red lines are of the same length. One line is parallel to the slip direction spanning from the epicenter of the rotated fault to the point where it meets the coastline. The other line is the vertical distance from the epicenter of the last hypothetical fault to the coastline.

Following this procedure, a fault where strike direction is not parallel to the coastline and/or rake angle is not 90° can be converted into a series of hypothetical faults where the strike direction is parallel to the coastline and rake angle is 90°.

2.3.3 TRRF application for prediction

Fig. 2.8 shows the procedure for how the TRRF predicts a tsunami run-up distribution once the TRRF is built. The first step is to convert the earthquake fault into a series of hypothetical faults using the AP method. The second step is to estimate the OS formula coefficients a_i^p, b_i^p $(i = 1, 2...n)$ of hypothetical faults using the RSM functions (Eqs. 2.7 and 2.8). The third step is to estimate the OS formula coefficient c_i^p $(i = 1, 2...n)$ by inputting the X_i^p into Eq. 2.9. The fourth step is to estimate the final source run-up $S^p(x)$ by inputting the OS formula coefficients (a_i^p, b_i^p, c_i^p) into Eq. 2.2 and taking the maximum values of the estimated source run-ups for all hypothetical faults. Finally, the tsunami run-up distribution $R^p(x)$ can be estimated by inputting the source run-up $S^p(x)$ and the normalized topographic run-up $NT^p(x)$ to Eq. 2.6.

2.4 TRRF development for northern Puerto Rico

2.4.1 Numerical simulation

In this study, we assumed that the coastline of northern Puerto Rico runs parallel to east-west direction ($\delta = 0°$), and thus the x-axis is parallel to east-west direction and y-axis is parallel to north-south direction (Fig. 2.2). In this condition, the epicenter location along the x-axis (X) is only related to the epicenter longitude (LON) and the epicenter location along the y-axis (Y) is only related to the epicenter latitude (LAT).

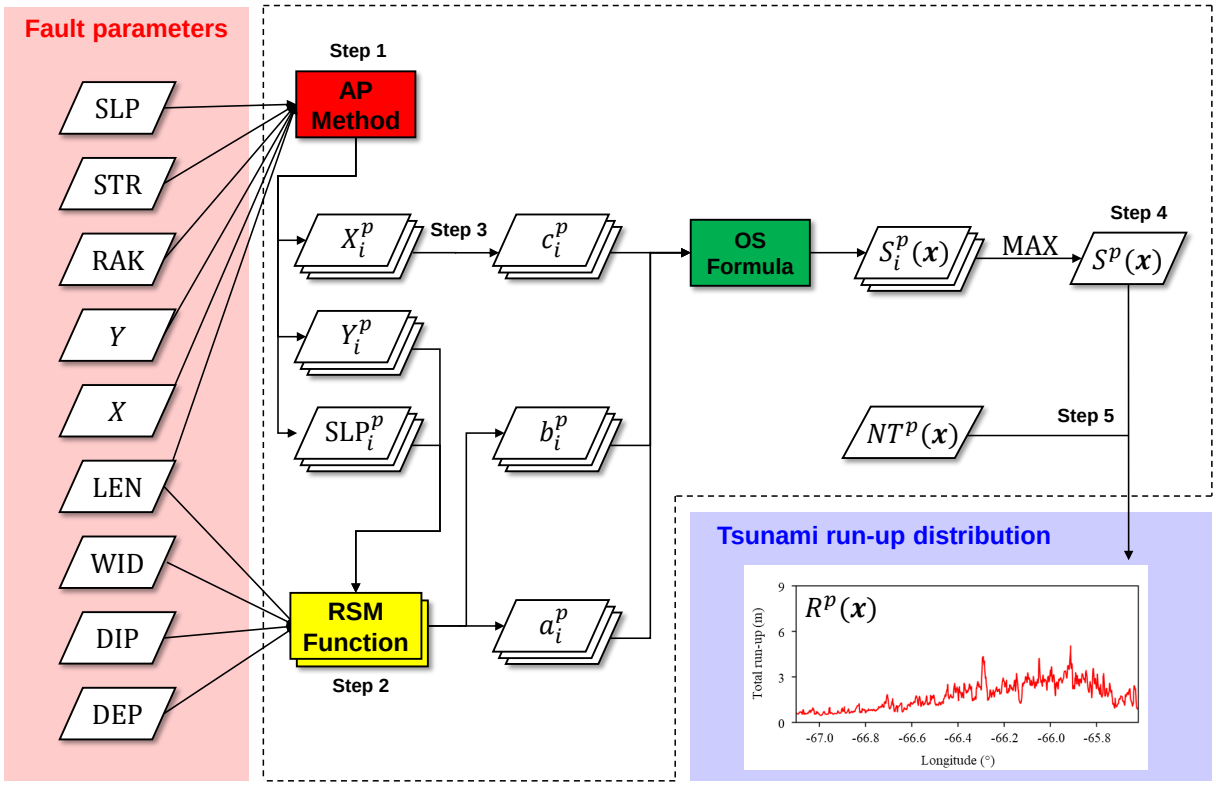

Figure 2.8: Computational flow of TRRF application for prediction. The inputs, the processing steps, and the outputs are represented in light red box, white dashed box, and light blue box, respectively. The subscript i represents the ith hypothetical fault, and the superscript p represents the prediction. MAX represents the process of extracting the maximum value along the x-axis.

The 729 tsunamigenic-earthquake scenarios were simulated based on the numerical model Basilisk, which solves the Green-Naghdi equations and employs both Adaptive Mesh Refinement (AMR) and parallelization to facilitate efficient computation. The Basilisk model has not only been validated with several benchmark problems but also been applied to several tsunami research [74, 112, 153]. The 729 scenarios were designed as shown in Table 2.1. The range of the epicenter latitude LAT was determined based on National Oceanic and Atmospheric Administration (NOAA)'s pre-defined unit sources and historical earthquake records in northern Puerto Rico (Fig. 2). The range of the fault length LEN, fault width WID, and slip SLP was set based on the assumption that the moment magnitude (M_w)

should be larger than 7.0 for a tsunami to occur. We used the empirical regression of Hanks and Kanamori [46] and fundamental equation of Aki [1] to calculate the moment magnitude:

$$M_w = \frac{2}{3}\left[\log\left(M_0\right) - 9.05\right] \tag{2.22}$$

$$M_0 = \mu(LEN \times WID \times SLP) \tag{2.23}$$

where M_0 is a seismic moment (Nm), μ is rigidity modulus of the Earth's crust (Nm^{-2}), and the units of LEN, WID, and SLP are in meters. We assumed that the rigidity modulus μ is 4.2×10^{10} Nm^{-2} in northern Puerto Rico following Grilli et al. [43]. We limited the maximum moment magnitude to 8.0 considering the historical seismic events that led to tsunamis in Puerto Rico [98]. We assumed that the LEN should be longer than the WID, and the range of the LEN and WID should follow the scaling laws introduced by Blaser et al. [11]. The range of the dip angle DIP and the depth of the top edge DEP were determined based on the characteristics of a subduction-interface earthquake that usually causes a tsunami. According to Thingbaijam et al. [137], subduction-interface earthquakes occur between 10° and 30° dip angles and within a slip-centroid depth of 50 km. We assumed that the fault rupture occurred instantaneously, where the initial free surface displacement was calculated using the Okada equations [104]. Nearshore bathymetry and onshore topography in the inundation zone were from the 3 arc-second National Geophysical Data Center data set [100], while the 1 arc-minute ETOPO1 data set [3] was used for the entire region (Fig. 2.2). Considering the grid size, the minimum and maximum AMR levels were set to 5 and 11, respectively. The bottom friction was parameterized using a quadratic drag law in which the bottom drag coefficient C_f was set to 10^{-4}. The numerical model was used to simulate two hours of tsunami propagation to ensure that complete inundation of the onshore areas was captured. The maximum envelope of the water level was interpolated

bilinearly onto a regular grid (0.001° interval). We excluded four simulations, which failed to finish the simulations because of instability issue, to build the TRRF. A sensitivity test showed that the impact of building the TRRF without four simulations on the accuracy of the TRRF was negligible. We obtained tsunami run-up distribution $R(x)$ by extracting the maximum inundation height along the coastline ranging from $67.100°W$ to $65.620°W$. The tsunami simulations were conducted in a spherical coordinate system, but the TRRF was defined based on a Cartesian coordinate system. To align the coordinate systems, Vincenty's formulae [146] were used to convert the unit of the geometric point from degrees to kilometers. We set the origin at ($18.450°N$, $66.400°W$) and used it as a reference point in Vincenty's formulae.

2.4.2 RSM functions and $NT^p(x)$

The RSM functions and the normalized topographic run-up $NT^p(x)$ were derived as follows. We calculated the OS formula coefficients a and b by fitting the tsunami run-up distribution $R(x)$ to the OS formula for each simulation (Eq. 2.2). Here, the OS formula coefficient c was fixed to zero because we set the longitude of the origin and the epicenter longitude of simulations identically (Eq. 2.9). We derived the RSM functions by fitting the RSM parameters to the OS formula coefficients a and b using second order polynomial models. The normalized topographic run-up $NT(x)$ was calculated for each simulation following Eqs. 2.1-2.3. We derived $NT^p(x)$ by selecting the 50th percentile of $NT(x)$ among all simulations (Fig. 2.9).

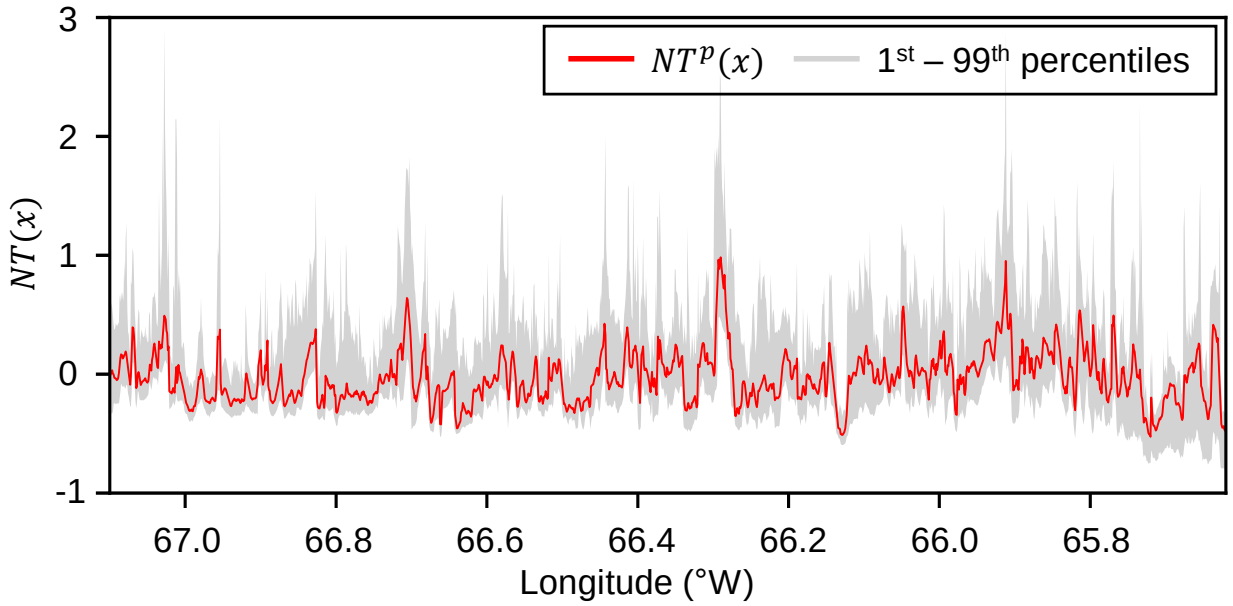

Figure 2.9: Normalized topographic run-up $NT^p(x)$ of northern Puerto Rico. The gray represents the range between 1^{st} and 99^{th} percentiles.

2.4.3 Fault parameter range for TRRF prediction

We set the fault parameter range for TRRF prediction as shown in Table 2.1. The range of six fault parameters (LAT, LEN, WID, DIP, SLP, DEP) was set to the same range as the tsunamigenic-earthquake scenarios used in the TRRF development. In order to avoid an extrapolation beyond the inference space of the RSM functions, we only considered cases where all epicenter of the hypothetical faults fell within the range for LAT. The range of LON was set to the extent that the fault does not fall outside the region used in the numerical simulation. The strike angle is usually set in the direction tangential to the subduction zone [38], and thus we set the range of STR to be from 50° to 130°. Even though some tsunamis are generated by strike-slip earthquakes [52], most tsunamis are caused by thrust earthquakes. Following this characteristic of RAK, we set the range of RAK to be from 50° to 130°.

Table 2.1: Range of fault parameters used for TRRF development and TRRF prediction

Fault	Development			Prediction	
Parameter	Low	Central	High	Min	Max
$LAT(°N)$	19.0	19.3	19.6	19.000	19.600
$DIP(°)$	10	20	30	10	30
$LEN(km)$	60	90	120	60.000	120.000
$WID(km)$	20	40	60	20.000	60.000
$SLP(m)$	2	3	4	2.00	4.00
$DEP(km)$	10	20	30	10.000	30.000
$LON(°W)$		66.4		65.800	67.000
$STR(°)$		90		50	130
$RAK(°)$		90		50	130

2.5 TRRF calibration

To apply the AP method, (1) the site-specific coefficients (α, β, and γ) of Eqs. 2.10 and 2.11 and (2) the number of hypothetical faults (n) must be defined in advance.

To determine the coefficient α, we simulated 80 additional cases (hereafter called STR cases) that were not used in building the TRRF. These additional cases had a fixed longitude of $66.400°W$, where 10 sets varying the RSM parameters were randomly selected. For each set, eight different strike angles between 50° and 130° were selected, at 10° intervals, except 90°. The rake angle was fixed to 90° so that θ could be independent of β and λ could be fixed to 90° (see Eqs. 2.10 and 2.11). The coefficient α was selected by minimizing TRRF error as represented by normalized root mean square error ($NRMSE$):

$$NRMSE = \frac{\sqrt{\frac{1}{N}\sum_{x=1}^{N}\left[R^p(x) - \hat{R}^p(x)\right]^2}}{max\left[\hat{R}^p(x)\right] - min\left[\hat{R}^p(x)\right]} \times 100\,(\%) \tag{2.24}$$

where $R^p(x)$ is the tsunami run-up distribution predicted by the TRRF, $\hat{R}^p(x)$ is the numerically simulated tsunami run-up distribution, and N is the total number of alongshore

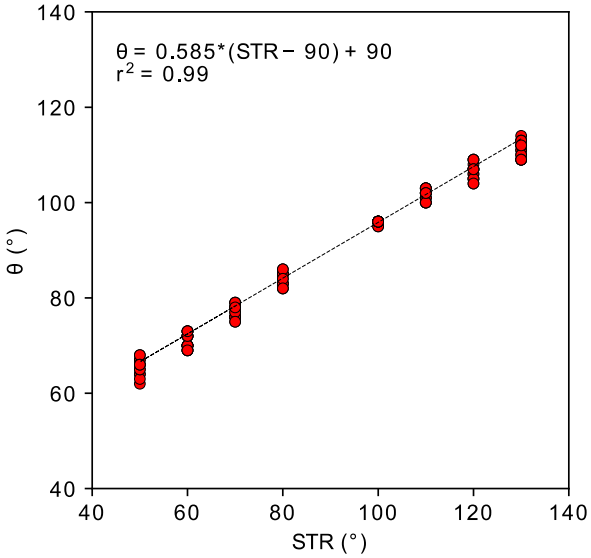

Figure 2.10: Best θ values (that show the minimum NRMSE) associated with varying strike angles. Dashed line represents the best-fitting line.

locations. For each case, we found the θ value that shows the minimum NRMSE in the range of 45° and 135°. We fixed the number of hypothetical faults (n) to 100, which was large enough to provide a convergent prediction. We set the coefficient α to 0.585 by fitting the STR and the θ in Eq. 2.10 (Fig. 2.10).

To determine the coefficients (β, and γ), we simulated 80 additional cases (hereafter called RAK cases) where all fault parameters but the rake angle were set in the same way as the STR cases. Unlike the STR cases, the rake angle was set to the same value as the strike angle. For each case, we found the θ value that shows the minimum NRMSE in the range of 45° and 135°. At the same time, we found the λ value that shows the minimum NRMSE in the range of 90° and 179° (if $RAK < 90°$) or the λ value that shows the minimum NRMSE in the range of 1° and 90° (if $RAK \geq 90°$). We set the coefficient β to -0.284 by fitting the RAK and the θ to Eq. 2.10 (Fig. 2.11(a)). We set the coefficient γ to -0.754 by fitting the RAK and the λ in Eq. 2.11 (Fig. 2.11(b)).

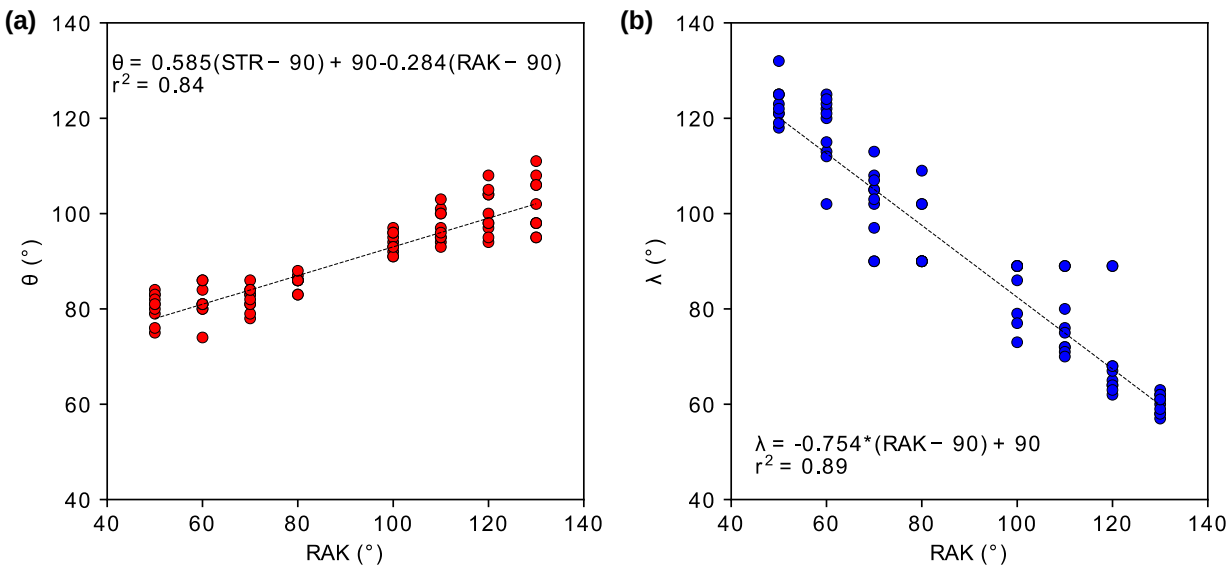

Figure 2.11: Best (a) θ and (b) λ values (that show the minimum NRMSE) associated with varying rake angles. Dashed line represents the best-fitting line.

To determine the number of hypothetical faults (n), we revisited the RAK cases. For each case, we decreased the number of hypothetical faults (n) from 100 to 2 (Fig. 2.12). Then, we found the minimum value needed for convergence since the computational time increases as n increases. In this study, we set the n to 30, which shows less than 0.1% difference in NRMSE.

2.6 TRRF performance

2.6.1 Accuracy

The accuracy of the TRRF was investigated by comparing TRRF predictions against the direct numerical simulations. We systematically tested the accuracy of the TRRF as follows:

- Test 1: To test whether the RSM functions and the $NT^p(x)$ are valid, we simulated

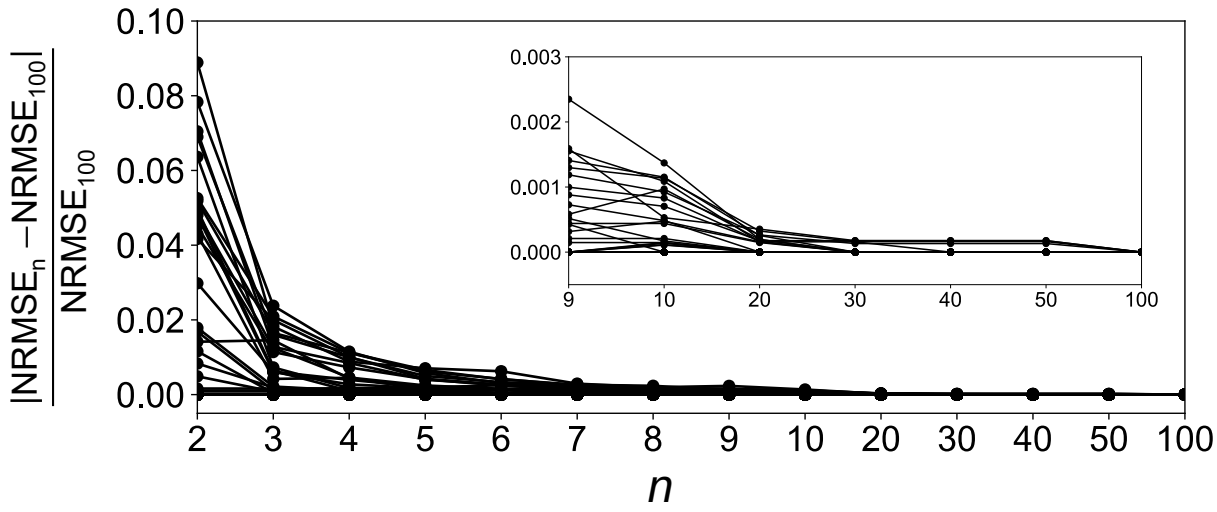

Figure 2.12: Relative $NRMSE$ differences as the total number of hypothetical faults (n) increases. $NRMSE_n$ is the $NRMSE$ of the case where n hypothetical faults are considered. $NRMSE_{100}$ is the $NRMSE$ of the case where 100 hypothetical faults are considered.

100 additional cases in which the RSM parameters were randomly selected, while the epicenter longitude was fixed to 66.400°W and both the strike and rake angles were fixed to 90°.

- Test 2: To test whether Eq. 2.9 is valid, we simulated 100 additional cases in which the fault parameters were selected based on the following conditions. While both the strike and rake angles were fixed to 90°, 10 sets of the RSM parameters were randomly selected. For each set, 10 longitudes were selected at a uniform interval in the range of 65.800°W and 67.000°W.

- Test 3: To test the performance of the AP method, we investigated the RAK cases defined in Section 2.5.

- Test 4: To test the overall accuracy of the TRRF, we simulated 100 additional cases in which all fault parameters were randomly selected.

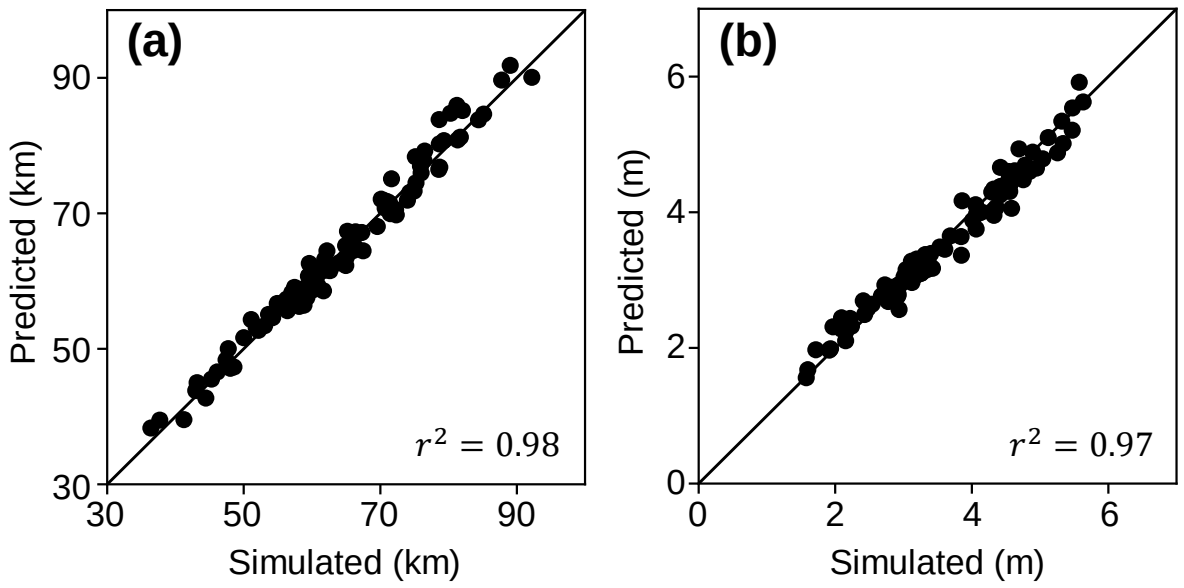

Figure 2.13: Comparison of OS formula coefficients between Basilisk (simulated) and TRRF (predicted): (a) OS formula coefficient a, (b) OS formula coefficient b.

Fig. 2.13 shows the comparison of the OS formula coefficients based on the 100 cases of Test 1. Note that these 100 cases were never used to derive the RSM functions. The x-axis is the OS formula coefficient obtained by fitting the numerical simulation result to the OS formula. The y-axis is the OS formula coefficient obtained by putting the fault parameters to the RSM functions. The high-correlated results confirm that the RSM functions can predict the OS formula coefficients well.

Fig. 2.14 shows the selected alongshore tsunami run-up predictions for each test. Fig. 2.14(a) and (b) show the best case (minimum $NRMSE$) and the worst case (maximum $NRMSE$) of Test 1, respectively. In both cases, the TRRF prediction followed the overall trend of the numerical simulation result well. However, there are a few localities where the TRRF did not predict the run-up well such as the run-ups near $66.2°W$ in the worst case. Fig. 2.14(c) and (d) display the Test 2 results where all the fault parameter conditions were the same except the epicenter longitude. The results show that the TRRF can effectively capture the

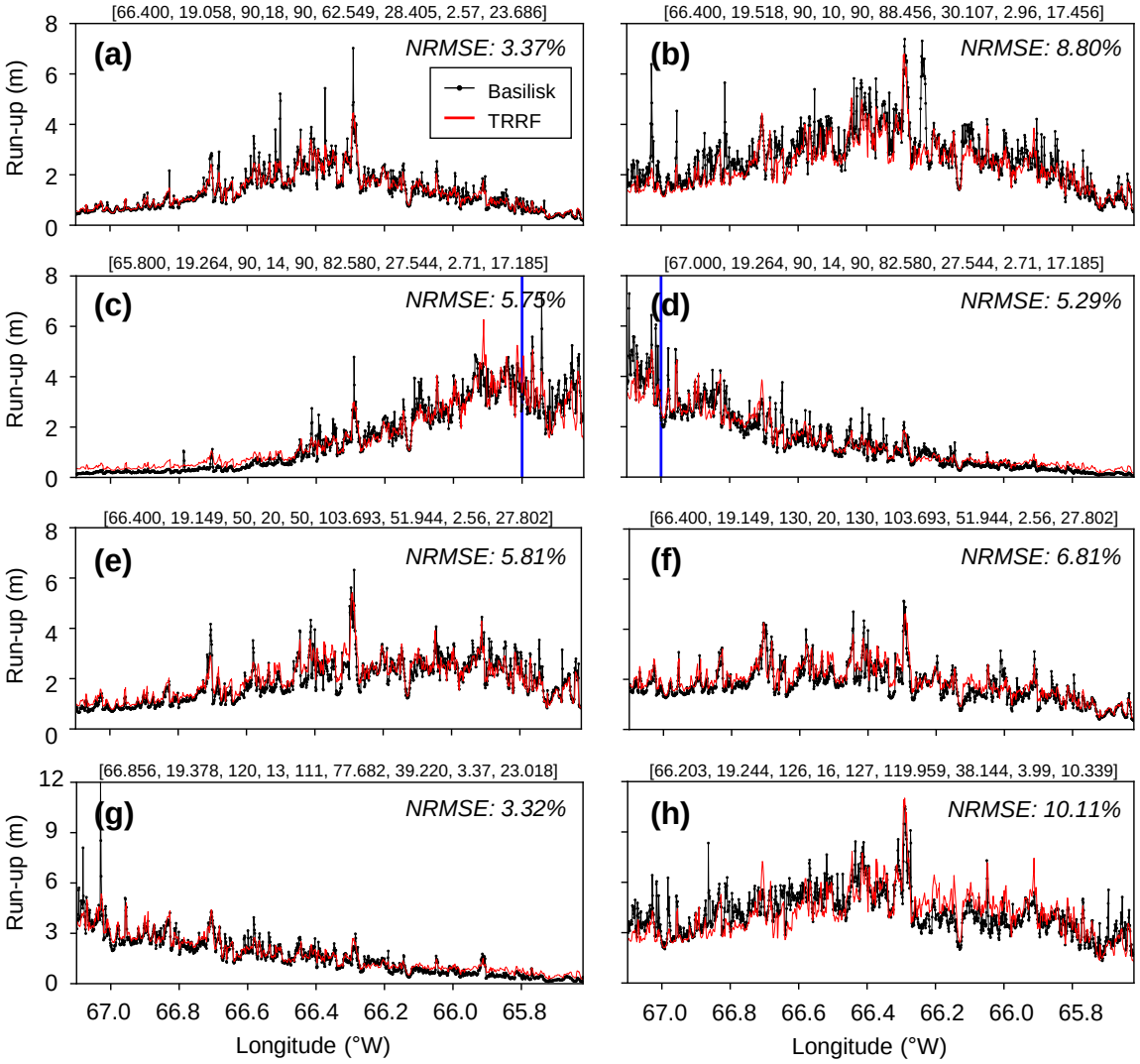

Figure 2.14: Selected examples of tests: (a and b) Test 1. (c and d) Test 2. (e and f) Test 3. (g and h) Test 4. Black line and red line are the tsunami run-up distributions predicted by Basilisk and TRRF, respectively. The number inside the bracket above each pane represents the fault parameters in this sequence: $LON(^{\circ}W)$, $LAT(^{\circ}N)$, $STR(^{\circ})$, $DIP(^{\circ})$, $RAK(^{\circ})$, $LEN(km)$, $WID(km)$, $SLP(m)$, $DEP(km)$. The blue line in (c) and (d) represents the location of epicenter longitude.

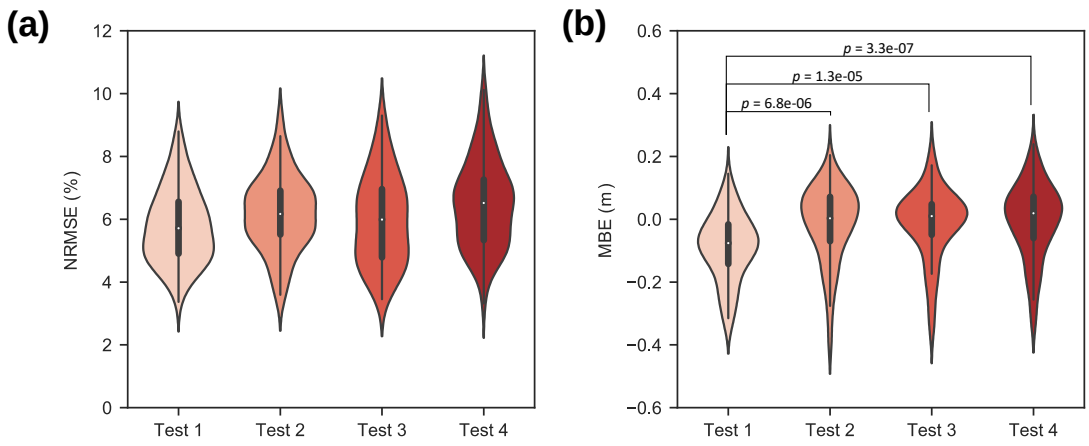

Figure 2.15: Overall error of TRRF: (a) Normalized root mean square error (%), (b) Normalized bias error (m). The violin plot shows the distribution of test results with the box and whisker plot inside where the black box represents the interquartile range, the black lines stretched from the box represent the range of 1.5 times of the interquartile range, and the white dot represents the median. p is a p-value of Welch's t-test.

influence of the epicenter longitude. Fig. 2.14(e) and (f) present the Test 3 results in which all fault parameter conditions are the same except for the strike and rake angles. Note that the TRRF predictions strongly align with the numerical simulation results while capturing the asymmetrical shape of the tsunami run-up distribution. Fig. 2.14(g) and (h) show the best case (minimum $NRMSE$) and worst case (maximum $NRMSE$) of Test 4, respectively. Both examples have a few localities where the TRRF did not predict the run-ups well, but the overall trend of the TRRF predictions agrees well with the numerical simulation results.

Fig. 2.15 shows the overall error of the TRRF in each corresponding test where the mean bias error (MBE) is defined as follows:

$$MBE = \frac{1}{N}\sum_{x=1}^{N}\left[R^p(x) - \hat{R}^p(x)\right] \tag{2.25}$$

where $R^p(x)$ is a TRRF prediction, $\hat{R}^p(x)$ is a numerically simulated tsunami run-up distri-

bution, and N is the total number of alongshore locations. As shown in Fig. 2.15(a), the overall $NRMSE$ of Test 2 ($3.40\% - 9.21\%$) has only increased slightly compared to Test 1 ($3.37\% - 8.80\%$), and this result confirms that Eq. 2.9 is valid. Also, the overall $NRMSE$ of Test 3 ($3.46\% - 10.02\%$) increased only slightly from Test 1, and this result confirms the performance of the AP method. The overall $NRMSE$ of Test 4 ($3.32\% - 10.11\%$) shows that the TRRF can produce reliable run-up distribution. Fig. 2.15(b) shows that the TRRF underestimated the run-up in Test 1 while slightly overestimating the run-up in Test 2 and Test 3. The overall MBE of Test 4 shows that the TRRF can predict run-up distribution without an apparent bias ($MBE = -0.33\ m - 0.24\ m$).

2.6.2 Computational time

The efficiency of the TRRF was investigated by comparing the computational time between the physics-based numerical model and the TRRF. When the physics-based numerical model (Basilisk) was used to predict the tsunami run-up distribution, the computational time was about one hour (24 CPU hours) on average for each scenario (24 cores, OpenMP, Intel Xeon E5-2680v3). On the other hand, when the TRRF was used to predict the tsunami run-up distribution, the computational time was only 0.01 CPU second per scenario (desktop computer with one core, Intel I7-7700). The TRRF's CPU time is nearly 9 million times shorter than that of numerical simulation. The difference in computational time between the TRRF and the numerical model would be even greater given higher resolution grids and larger geographic areas than those used in this study.

2.7 Discussion

The performance of TRRF was investigated based on total 380 additional simulations in Section 2.6. When the TRRF predictions are compared against the direct numerical simulations, it is clear that the TRRF can produce reliable run-up predictions over real topography, given the computational time. However, as shown in Fig. 2.14, even though the TRRF predicts the leading order of tsunami run-up distribution well, there are a few localities where the difference of the run-up is more than two-fold. We found that these localities are correlated to the uncertainty (or the range of percentiles) of $NT^p(x)$ (Fig. 2.9). For example, a large uncertainty was commonly found in places with complex topography, such as areas surrounded by mountains (e.g., $65.735°W$), areas containing a river (e.g., $66.955°W$), steep cliffs (e.g., $66.444°W$), and coastal dunes (e.g., $66.239°W$). Even though it is difficult to fully interpret the physics behind the normalized topographic run-up $NT^p(x)$, we think that this high uncertainty may be attributed to the nonlinear behavior of the tsunami wave as it propagates and inundates complex topography. In its present form, the TRRF does not directly consider potential nonlinearities between the source and topographic run-up components in the hypothesis that the tsunami run-up distribution can be expressed as a sum of the source and topographic run-ups (Eq. 2.1). Future studies should investigate ways to account for the uncertainty to improve the accuracy of the TRRF approach.

As shown in Fig. 2.15(b), Test 1 shows statistically different MBE compared to other tests ($p < 0.05$). The TRRF generally underestimated the run-up in Test 1 where the fault parameters were set based on the following conditions: (1) X is fixed to zero, (2) strike direction is parallel to the coastline, and (3) the rake angle is 90°. In this condition, the error is only related to the RSM functions and the normalized topographic run-up, $NT^p(x)$. We think that this underestimated run-up may be attributed to the characteristic of $NT^p(x)$ of northern Puerto Rico, for two reasons. First, the RSM functions predicted

the OS formula coefficients well (Fig. 2.13), and second, most of the $NT^p(x)$ ($67.1°W$ – $65.8°W$) was biased towards the lower values within the range of $NT(x)$ (Fig. 2.9). On the other hand, the TRRF slightly overestimated the run-up in Test 2 and Test 3 which were designed to test the error of Eq. 2.9 and that of the AP method, respectively. It should be noted that when all fault parameters are randomly selected (Test 4), there was no apparent bias (Median $MBE = 1.8\ cm$). We think this is because the negative bias caused by $NT^p(x)$ is compensated by the positive bias caused by Eq. 2.9 and the AP method. Future studies should investigate how to reduce distinct bias in a certain condition like Test 1.

Moreover, future studies should expand the applicability of the TRRF by considering the following limitations. One is that the TRRF is only applicable to uniform slip distribution. Several studies have shown that tsunami prediction can vary depending on heterogeneous slip models even when the earthquake magnitude is the same [25, 36, 79, 119]. The other limitation of the TRRF is that it is only applicable to tsunamis generated by seafloor displacements associated with earthquakes. After earthquakes, landslides are the second most common cause of tsunamis [47]. Moderate earthquakes do not always cause tsunamis themselves, but they can, in some instances, trigger large landslides that result in tsunamis [144]. Though landslide-generated tsunamis are rare, a single occurrence can cause substantial damage and loss of life. For example, in 2017, a landslide-generated tsunami off the western coast of Greenland flooded several villages and resulted in casualties [106]. A recent study also revealed that the 2018 Indonesian tsunami, which claimed more than 2,000 lives and severely damaged coastal communities, was caused by the combination of an earthquake and a landslide [121]. Several other key elements would merit attention in future studies. For example, the arrival time and inundation distance are as important to consider as the run-up. A high tide could enhance tsunami inundation, while a receding tide could dissipate tsunami energy [142, 155]. Likewise, a modest amount of sea-level rise could dramatically

impact the tsunami run-up distribution [80]. Lastly, the TRRF was able to reduce the input dimensionality by using the OS formula, but the OS formula limits its applicability to straight coastal areas and near-field tsunamis. To generalize the applicability of TRRF, future studies should investigate the effect of a coastline shape and that of a distance between an earthquake source and a coast.

2.8 Conclusions

In the present study, we presented a new methodology, called TRRF, that can predict the alongshore run-up distribution from a near-field tsunami. We adopted the OS formula and developed what we call the AP method to reduce the number of simulations to build the TRRF. The tsunami run-up distribution was decomposed into source run-up and topographic run-up, that source run-up can be modeled by earthquake fault parameters, and that normalized topographic run-up is associated with local topographic characteristics. Using the northern region of Puerto Rico as a case study, the performance of the TRRF was investigated based on total 380 additional simulations. The results showed that the TRRF can produce rapid near-field tsunami run-up predictions over real topography ($3\% - 10\%$ of $NRMSE$, $-0.33\ m - 0.24\ m$ of MBE). We expect that future applications of the TRRF will have the potential to save lives and promote resiliency of coastal communities.

2.9 Acknowledgments

This material is based upon work supported by the National Science Foundation under Grant Nos. 1630099 and 1735139. The authors acknowledge Advanced Research Computing at Virginia Tech for providing computational resources and technical support that have

contributed to the results reported within this paper. URL: http://www.arc.vt.edu

Chapter 3

Probabilistic near-field tsunami source and tsunami run-up distribution inferred from tsunami run-up records in northern Chile

Jun-Whan Lee [1], Jennifer L. Irish [1,3], Robert Weiss [2,3]

[1] Department of Civil and Environmental Engineering, Virginia Tech, 750 Drillfield Dr, Blacksburg, VA, 24061, USA

[2] Department of Geosciences, Virginia Tech, 926 W Campus Dr, Blacksburg, VA, 24061, USA

[3] Center for Coastal Studies, Virginia Tech, 926 W Campus Dr, Blacksburg, VA 24061, USA

This manuscript is under review.

3.1 Abstract

Understanding a tsunami source and its impact is vital to assess a tsunami hazard. Thanks to the efforts of the tsunami survey teams, high-quality tsunami run-up data exists for contemporary events. Still, it has not been widely used to infer a tsunami source and its impact mainly due to the computational burden of the tsunami forward model. In this study, we propose a TRRF-INV (Tsunami Run-up Response Function-based INVersion) model that can provide probabilistic estimates of a near-field tsunami source and tsunami run-up distribution from a small number of run-up records. We tested the TRRF-INV model with synthetic tsunami scenarios in northern Chile and applied it to the 2014 Iquique, Chile, tsunami event as a case study. The results demonstrated that the TRRF-INV model can provide a reasonable tsunami source estimate to first order and estimate tsunami run-up distribution well. Moreover, the case study results agree well with the United States Geological Survey report and the global Centroid Moment Tensor solution. We also analyzed the performance of the TRRF-INV model depending on the number and the uncertainty of run-up records. We believe that the TRRF-INV model has the potential for supporting accurate hazard assessment by (1) providing new insights from tsunami run-up records into the tsunami source and its impact, (2) using the TRRF-INV model as a tool to support existing tsunami inversion models, and (3) estimating a tsunami source and its impact for ancient events where no data other than estimated run-up from sediment deposit data exists.

3.2 Plain language summary

Thanks to tsunami survey teams, there are observations of the highest elevation flooded by tsunamis in discrete locations. However, this data has not been widely used to deter-

mine where the earthquake that triggered the tsunami occurred, how large the earthquake was, and how large and extensive the floods caused by the tsunami were. In this study, we develop a new computer model that can identify the earthquake information and the flooding extent along the coastline from the discrete flood observations. The new computer model is tested for thousands of artificial earthquake scenarios and a historical earthquake event that occurred in 2014 in Chile. The results show that the new computer model can estimate the earthquake information and the flooding extent well. We believe that this new computer model can advance understanding of historical tsunami events and lead to better preparedness plans for possible future tsunamis.

3.3 Introduction

Tsunamis, mainly caused by shallow subduction-zone earthquakes, can cause severe damage to coastal communities once they occur, especially to near-field areas. To mitigate the tsunami damage and increase the resiliency of coastal communities, it is crucial to better understand a tsunami source and assess its impact. To better understand the tsunami source, tsunami inversion models, which can infer a tsunami source from observed data, have been widely developed [123]. Depending on the input data, tsunami inversion models can be divided into three types. The first type is a tsunami inversion model that relies on seismic waveform data alone or combined with other data such as local strong motion, GPS (Global Positioning System), InSAR (Interferometric Synthetic Aperture Radar), and DART (Deep-ocean Assessment and Reporting of Tsunamis) data [e.g. 75, 151, 152]. Instead of relying on seismic waveform data, the second type is a tsunami inversion model that uses tsunami waveforms (such as DART, tide gauge data) alone or combined with GPS and/or InSAR data [e.g. 53, 117, 149, 156]. This methodology was first proposed by Satake [122] and is receiving

increased attention, especially after the Mw 9.0 2011 Tohoku-Oki earthquake, because one of the main reasons for enormous casualties and tsunami damage is known to be due to underestimating the earthquake's magnitude and resulting tsunami run-up by relying on the early arrival of seismic waveform data alone [54]. The third type is a tsunami inversion model that uses tsunami sediment deposit data to infer the historical tsunami source, especially for the paleotsunami events [e.g. 57, 87, 89, 96]. Once a tsunami source is estimated, a tsunami forward model —usually a high-fidelity physics-based numerical model that can simulate tsunami propagation and inundation processes from a given tsunami source—is then used to assess the impact of tsunamis.

A tsunami run-up, the maximum ground elevation wetted by the tsunami, is one of the important characteristics to quantify the impact of a tsunami. Thanks to the tsunami survey teams such as the International Tsunami Survey Team (ITST), there are many high-quality tsunami run-up data sets for contemporary events [e.g. 7, 133]. For this reason, the tsunami run-up distribution along the coastline is usually employed to validate the tsunami source and to evaluate the impact of tsunamis. However, there are only a few studies that directly used tsunami run-up data to infer a tsunami source [e.g. 33, 87, 111]. One of the main reasons is the tsunami forward model's computational burden because a tsunami inversion model requires a large number of tsunami forward simulations to find a tsunami source that best matches the tsunami run-up records. Even though several tsunami forward models employed computational techniques to improve the computational efficiency, such as adaptive mesh refinement and parallelization techniques [e.g. 88, 112], estimating a tsunami run-up distribution using high-fidelity physics-based numerical models remains computationally intensive. For this reason, Fuentes et al. [33] and Piatanesi et al. [111] have relied on a less accurate but faster tsunami forward model than the high-fidelity model, which estimates run-up by multiplying an amplification factor and the maximum wave height of the

offshore point, to consider a large number of scenarios. On the other hand, MacInnes et al. [87] used a high-fidelity tsunami forward model but considered only a handful of scenarios determined by expert judgment.

To overcome the computational burden of the high-fidelity physics-based numerical model, Lee et al. [77] recently developed a tsunami forward model based on a response surface methodology, hereafter Tsunami Run-up Response Function (TRRF) model, that can rapidly estimate a near-field tsunami run-up distribution over real topography without substantial loss of accuracy, with respect to high-fidelity models. The main concept of the TRRF model is that the tsunami run-up distribution can be decomposed into (1) a leading-order contribution being modeled by fault parameters using the Okal and Synolakis [105]'s empirical formula and (2) a regional component that is dictated by the local topography.

This study proposes a new tsunami inversion model based on the TRRF model to infer a near-field tsunami source and tsunami run-up distribution from tsunami run-up records: hereafter referred to as Tsunami Run-up Response Function-based INVersion or TRRF-INV model. This study provides the first tsunami inversion model capable of giving probabilistic estimates of tsunami source information (moment magnitude, epicenter location, fault length, fault width, average slip) from tsunami run-up records. Moreover, to our best knowledge, our work is the first attempt to provide probabilistic estimates of tsunami run-up distribution derived only from a small number of tsunami run-up records. We chose the northern Chile coastal region as a study area and investigated the performance of the TRRF-INV model based on synthetic tsunami run-up records, and then we applied the TRRF-INV model to real tsunami run-up records of the M_W 8.2 2014 Iquique, Chile, earthquake.

3.4 Study area

The northern Chile coastal area is an active subduction zone where the Nazca plate is being subducted under the continental South-American plate at high rates [about $63 mm/year$, 18] (Fig. 3.1). The city of Iquique, one of the important commercial and industrial urban centers in the northern Chile coastal region, is exposed to significant tsunami risk considering its inhabitants (about $184,000$) and critical coastal infrastructures [42]. Historically, large earthquakes ($M_W > 8.5$) occurred in 1868 and 1877 near the convergent tectonic plate interface, and the tsunamis damaged the cities in northern Chile coastal region [42, 71]. On April 1st, 2014, at 23:46:50 UTC, a M_W 8.2 earthquake occurred off the coast of Pisagua in northern Chile in an area known as a seismic gap (a portion of an active fault known to cause a major earthquake but not occurring for a long time.) [50]. This earthquake was detected in the form of a seismic waveform, strong motion, and GPS data, and the resulting tsunami was visually detected in several DART buoys and tide gauges [e.g. 4, 44, 76, 124]. Moreover, high-quality tsunami run-up records also exist [14]. Even though the 2014 Iquique earthquake relieved some amount of the accumulated deviatoric stress, several studies pointed out that the northern Chile coastal region still can generate a large earthquake with an associated tsunami [16, 119].

3.5 Method

The TRRF-INV model infers a tsunami source and tsunami run-up distribution from run-up records in four steps as follows (Fig. 3.2):

- Step 1: Set three angles (strike, dip, rake) and earthquake depth from a pre-defined list.

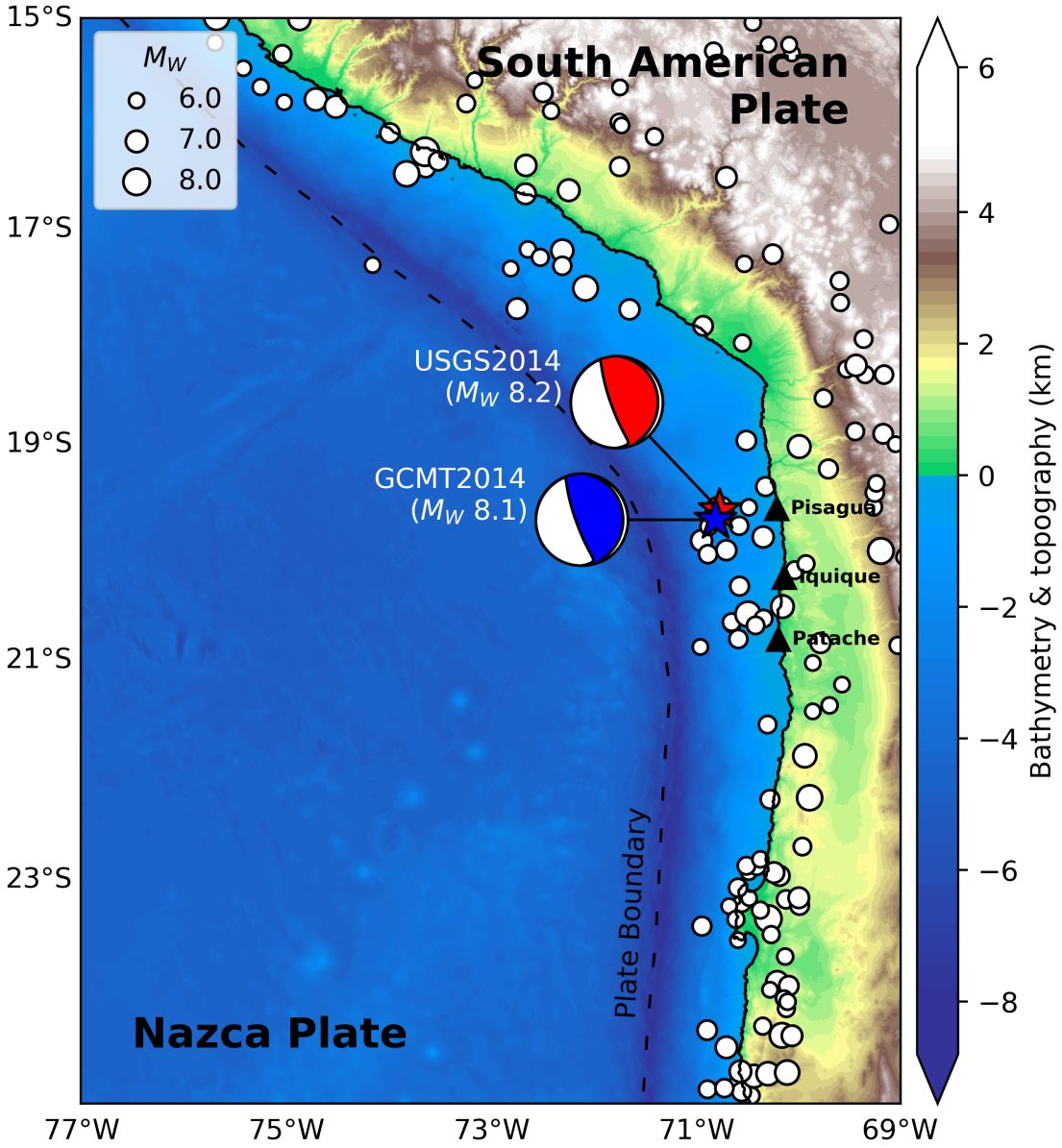

Figure 3.1: Map of the northern Chile coastal region. The white circles represent the historical earthquake records with magnitude larger than 6 (U.S. Geological Survey National Earthquake Information Center). The black dashed line represents the plate boundary between the Nazca and South American plates. Focal mechanisms (beachballs) and epicenters (stars) of the 2014 Iquique earthquake given by the USGS and the gCMT [28] are plotted in red and blue color, respectively. The locations of Patache, Iquique, Pisagua are shown in black triangles.

- Step 2: Determine the order in which to estimate the fault parameters (epicenter latitude, epicenter longitude, fault length, fault width, average slip).

- Step 3: Repeat estimating fault parameters until one of two thresholds (see section 3.5.3) is satisfied.

- Step 4: Generate earthquake scenarios based on the estimated fault parameters and save possible scenarios.

The TRRF-INV model repeats these four steps and accumulates possible earthquake scenarios until all combinations defined in step 1 are considered. And lastly, the probabilistic tsunami source and tsunami run-up distribution are estimated based on the accumulated scenarios.

To run the TRRF-INV model, a pre-trained TRRF model for the study area is required. In this study, we trained the TRRF model based on physics-based numerical simulations of 729 tsunamigenic-earthquake scenarios in the northern Chile coastal region (Table 3.1) following Lee et al. [77]. We used the numerical model Basilisk, an efficient hydrodynamic numerical model that employs an Adaptive Mesh Refinement (AMR) technique and a parallel computing technique [112]. We set the x-axis parallel to North and y-axis parallel to West. We systemically simulated additional 175 scenarios to calibrate the TRRF model. Then, to validate the TRRF model, we simulated 20 random scenarios (hereafter called base scenarios), which were never used to train or calibrate the TRRF model (Table B.1). The error of the TRRF model was represented by a normalized Root Mean Square Error ($NRMSE$), the $RMSE$ normalized by the maximum run-up:

$$NRMSE = \frac{\sqrt{\frac{1}{N_p}\sum_{x=1}^{N_p}\left[R_T(x) - R_p(x)\right]^2}}{max\left[R_p(x)\right]} \times 100\,(\%) \tag{3.1}$$

Table 3.1: Fault parameters used for TRRF training, calibration, and validation

Fault Parameter	Training			Calibration & Validation	
	Low	Central	High	Min	Max
$LON(°W)$	70.5	71.0	71.5	70.5	71.5
$DIP(°)$	10	20	30	10	30
$LEN(km)$	90	135	180	90	180
$WID(km)$	40	75	90	40	90
$SLP(m)$	2	4	6	2	6
$DEP(km)$	10	25	40	10	40
$LAT(°S)$		20		19.2	20.8
$STR(°)$		360		340	360
$RAK(°)$		90		70	110

where $R_T(x)$ is the tsunami run-up predicted by the TRRF model, $R_p(x)$ is the true tsunami run-up (Basilisk predictions or observational data), and N_p is the number of alongshore locations considered. More details on the TRRF model training, calibration, and validation can be found in B.1.

The TRRF-INV model also requires a pre-defined range of fault parameters (Table 3.2). Note that the fault-parameter range must be within the range used for TRRF model validation. The rest of the section will describe the details of the TRRF-INV model.

3.5.1 Step 1: Set three angles and earthquake depth

The TRRF-INV model sets three angles (strike STR, dip DIP, rake RAK) and top-edge fault depth (DEP) from a pre-defined list. In this study, we considered 27 combinations ($N_i = 27$) where three-level of STR, DIP, DEP and one RAK are considered (Table 3.2). The range of STR, DIP, DEP was determined based on the Slab model values in northern Chile [51]. Since the $NRMSE$ changes only up to 1% with rake angle over the range from $70° - 110°$, we assumed a pure reverse-slip mechanism ($RAK = 90°$).

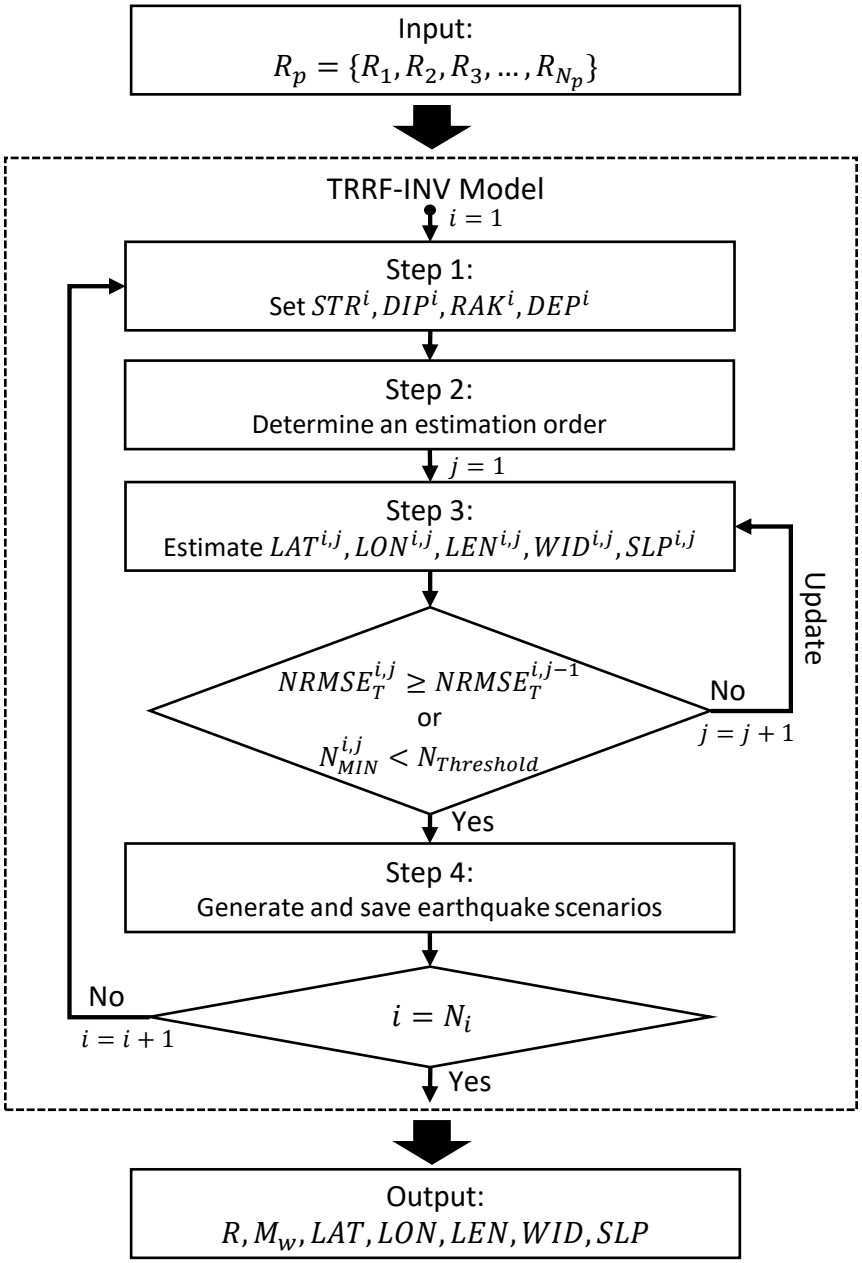

Figure 3.2: Computational flow of TRRF-INV model. The inputs are tsunami run-up records (R_p) where N_p represents the number of run-up records. The outputs are the probabilistic estimates of moment magnitude (M_W), epicenter latitude (LAT), epicenter longitude (LON), fault length (LEN), fault width (WID), average slip (SLP), and tsunami run-up distribution (R). N_i is the number of combinations of three angles and earthquake depth. j is the iteration number. $NRMSE_T$ is a total error. N_{MIN} is the minimum number of earthquake scenarios.

Table 3.2: The range of fault parameters with interval used in the TRRF-INV model

Fault Parameter	Min	Max	Interval
$LON(°W)$	70.5	71.5	0.1
$LAT(°S)$	19.2	20.8	0.1
$LEN(km)$	90	180	5
$WID(km)$	40	90	5
$SLP(m)$	2	6	0.5
$DEP(km)$	20	30	5
$STR(°)$	340	360	10
$DIP(°)$	10	30	10
$RAK(°)$	90	90	0

3.5.2 Step 2: Determine an estimation order

Even though the TRRF model is rapid (computational time: < 1 s/scenario), it is still computationally intensive to simulate all possible scenarios listed in Table 3.2 (> 9 million scenarios). To minimize the number of TRRF simulations, the TRRF-INV model determines the order in which to estimate the fault parameters (epicenter latitude LAT, epicenter longitude LON, fault length LEN, fault width WID, and average slip SLP) as follows.

First, the TRRF-INV model generates scenarios for each of the five fault parameters (hereafter a reference fault parameter) as follows. The reference fault parameter varies for all values in Table 3.2. The other four fault parameters vary for three-level values (minimum, maximum, and average of values listed in Table 3.2). The three angles and the earthquake depth are fixed to the values set in step 1. Note that the interval of five fault parameters in Table 3.2 was set to the value where the $NRMSE$ change within the interval is negligible ($< 0.5\%$ point). Secondly, tsunami run-ups are estimated based on the TRRF model for each scenario, and then the $NRMSE$ between the TRRF estimates and the run-up records is calculated. Thirdly, the scenarios where the reference fault parameter value is the same are grouped, and the mean error ($\overline{NRMSE}$) is calculated for each group. Fourthly, the maximum difference of $\overline{NRMSE}$ among groups ($\Delta\overline{NRMSE}$) is calculated. And lastly, once

the $\Delta\overline{NRMSE}$ is calculated for all fault parameters (LAT, LON, LEN, WID, SLP), the estimation order is defined as an order from the most sensitive fault parameter (which shows the largest $\Delta\overline{NRMSE}$) to the least sensitive fault parameter (which shows the smallest $\Delta\overline{NRMSE}$) (See example result in Appendix B.2).

3.5.3 Step 3: Estimate fault parameters

Following the estimation order, the fault parameters are estimated until one of two stop conditions is satisfied: (1) When the error does not decrease compared to the previous iteration, (2) When the number of generated scenarios is less than the threshold. From now on, the fault parameter of the ith combination (three angles and depth) of the jth iteration of kth estimation order will be represented as $FP_k^{i,j}$.

To estimate the first-order fault parameter ($FP_1^{i,j}$), the TRRF-INV model generates scenarios for each value of the FP_1 in Table 3.2 as follows. If it is the first iteration ($j = 1$), the TRRF-INV model generates scenarios considering all combinations of three-level values of FP_2, FP_3, FP_4, FP_5 used in step 2. Otherwise, the TRRF-INV model generates scenarios considering all combinations of the $(j-1)$th estimates of the other four fault parameters ($FP_2^{i,j-1}, FP_3^{i,j-1}, FP_4^{i,j-1}, FP_5^{i,j-1}$). The three angles and the earthquake depth are fixed to the values set in step 1. Secondly, tsunami run-ups are estimated based on the TRRF model for each scenario, and then the $NRMSE$ between the TRRF estimates and the run-up records is calculated. Thirdly, the scenarios where the FP_1 value is the same are grouped, and the base group is defined as a group that shows the smallest mean error ($min(\overline{NRMSE}_{FP_1}^{i,j})$). Fourthly, the model conducts the Welch's t-test between the base group and the other groups. Based on the t-test result, the estimates of the $FP_1^{i,j}$ are defined as the FP_1 values corresponding to the base group and the other groups that

show no statistically significant $\overline{NRMSE}$ difference compared to that of the base group ($p - value > 0.05$).

The other four fault parameters are estimated in the same way, following the estimation order. The only difference is that, when generating the scenarios to estimate the present-order fault parameter, the jth estimates of the preceding-order fault parameters are used instead of the $(j-1)$th estimates. For example, when estimating the fault parameter of the ith combination (three angles and depth) of the jth iteration of the third-order ($FP_3^{i,j}$), the jth estimates of the first and second-order fault parameters ($FP_1^{i,j}, FP_2^{i,j}$) are used to generate the scenarios, instead of the $(j-1)$th estimates ($FP_1^{i,j-1}, FP_2^{i,j-1}$).

Once all fault parameters ($FP_k^{i,j}$) are estimated, the total error ($NRMSE_T^{i,j}$) and the minimum number of generated earthquake scenarios ($N_{MIN}^{i,j}$) are calculated:

$$NRMSE_T^{i,j} = \sqrt{\sum_{k=1}^{5} (min(\overline{NRMSE}_{FP_k}^{i,j}))^2} \tag{3.2}$$

$$N_{MIN}^{i,j} = min(N_{FP_k}^{i,j}) \quad where\ k = 1, 2, ..., 5 \tag{3.3}$$

where $N_{FP_k}^{i,j}$ is the number of earthquake scenarios in the base group to estimate the $FP_k^{i,j}$. Then the TRRF-INV model decides whether to stop the iteration based on the two stop conditions:

$$NRMSE_T^{i,j} \geq NRMSE_T^{i,j-1} \tag{3.4}$$

$$N_{MIN}^{i,j} < N_{Threshold} \tag{3.5}$$

The first stop condition (Eq. 3.4) is when the total error is not reduced compared to the previous iteration. Note that the first stop condition is only checked after the second iteration ($j \geq 2$). The second stop condition (Eq. 3.5) is when the minimum number of generated earthquake scenarios is less than the threshold ($N_{Threshold}$). The larger the threshold, the less precise the model is, and the smaller the threshold, the more likely the error distribution is not to satisfy normality. In this study, we set the threshold ($N_{Threshold}$) to 10, balancing the model precision and normality of the error distribution. If one of the stop conditions is satisfied at the jth iteration, the model stops estimating the fault parameters, and the fault parameter estimates of the $(j-1)$th iteration are saved. Otherwise, the TRRF-INV model will repeat the procedure mentioned above (See example result in Appendix B.3).

3.5.4 Step 4: Generate and save earthquake scenarios

The last step is to generate the earthquake scenarios based on the estimated fault parameters and save the possible scenarios where the $NRMSE$ is smaller than the threshold. To be specific, the TRRF-INV model calculates the moment magnitude using the following equations [1, 46]:

$$M_W^i = \frac{2}{3}\left[\log\left(M_o^i\right) - 9.05\right] \tag{3.6}$$

$$M_o^i = \mu(LEN^i \times WID^i \times SLP^i) \tag{3.7}$$

where M_o is a seismic moment (Nm), μ is the rigidity modulus of the Earth's crust (Nm^{-2}), and the units of fault length (LEN), fault width (WID), and average slip (SLP) are in meters. In this study, we assumed that the rigidity modulus μ is 3.5×10^{10} Nm^{-2} in northern

Chile coastal region following Shrivastava et al. [130]. Secondly, the TRRF-INV model generates scenarios considering all combinations of the estimated epicenter (LAT^i, LON^i) and the three fault parameters (LEN, WID, SLP) within the range of moment magnitude (M_W^i). The three angles and the earthquake depth are fixed to the values set in step 1. Thirdly, tsunami run-ups are estimated based on the TRRF model for each scenario, and then the $NRMSE$ between the TRRF estimates and the run-up records is calculated. Finally, the TRRF-INV model saves the earthquake scenarios where the corresponding $NRMSE$ values are smaller than the threshold ($NRMSE^i_{Threshold}$) defined as follows:

$$NRMSE^i_{Threshold} = min(\mathbf{NRMSE}^i) + \alpha[max(\mathbf{NRMSE}^i) - min(\mathbf{NRMSE}^i)] \quad (3.8)$$

where $\mathbf{NRMSE}^i$ is a list of the $NRMSE$ values of the generated scenarios, and α is a constant that determines the threshold. In this study, after testing various α values, we set the α to 0.2 to balance the efficiency and the accuracy of the TRRF-INV model (Appendix B.4).

The TRRF-INV model repeats the process from step 1 to step 4 until all combinations of three angles and earthquake depth are considered ($i = N_i$). Once all combinations are considered, the TRRF-INV model estimates the probabilistic tsunami source and tsunami run-up distribution based on the accumulated earthquake scenarios.

3.6 Results

3.6.1 Performance on Synthetic Scenarios

To validate the TRRF-INV model, we generated 200 synthetic scenarios as follows. For each of the 20 base scenarios (Table B.1), we made ten scenarios by randomly selecting a few run-ups from the tsunami run-up distribution of Basilisk simulation. In this test, we fixed the number of run-up records ($N_p = 20$) to make the number of run-ups similar to the 2014 Chile tsunami run-up record. Note that only these 20 run-up data were provided to the TRRF-INV model as an input while the true values (the earthquake fault parameters and the tsunami run-up distribution) were intentionally concealed during the TRRF-INV model run. Here, we will first present the detailed result based on one of the synthetic scenarios (Figure 3.3) and then highlight the overall performance of the TRRF-INV model (Figure 3.4).

Figure 3.3 shows the results of the scenario with the smallest error for moment magnitude but the largest error for the tsunami run-up distribution among the ten random scenarios for Case 1 in Table B.1. Overall, the probabilistic estimates of tsunami source agree well with the true values for this synthetic scenario (Figure 3.3a). We defined the error (e) as the estimated value (that showed the highest probability) minus the true value. The TRRF-INV model slightly overestimated the M_W ($e = 0.04$), LON ($e = 0.014°$), LAT ($e = 0.124°$), and WID ($e = 19km$) while the model slightly underestimated the SLP ($e = -0.25m$). Even though the LEN shows a relatively large error ($e = -39km$), the true value falls within the high probability region ($> 0.6\%$). In Figure 3.3b, we plot the probabilistic estimate of the tsunami run-up distribution. The result shows that the probabilistic estimate of the TRRF-INV model agrees well with the true tsunami run-up distribution, except near the underestimated Patache area. The $NRMSE$ between the true value and median of

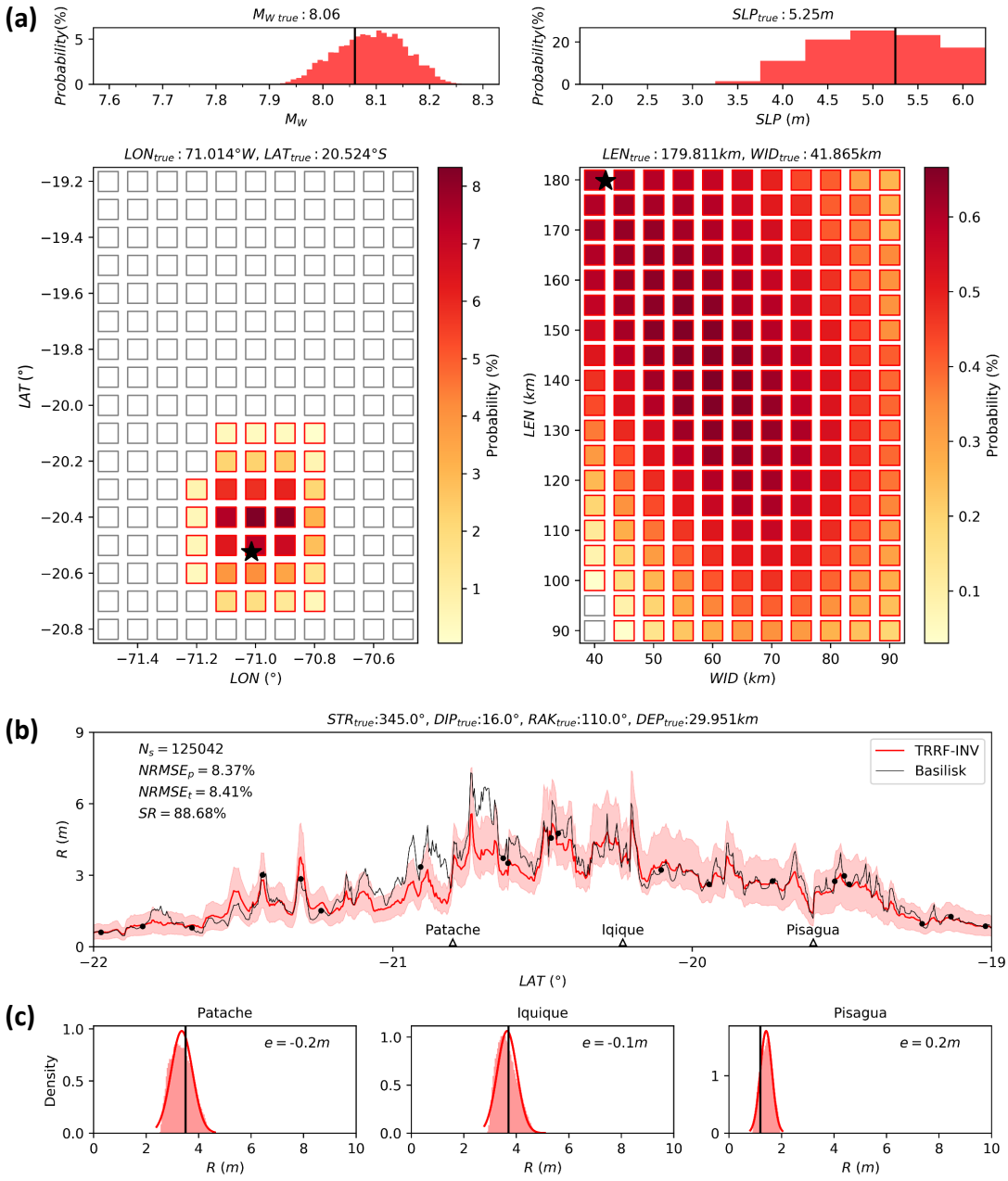

Figure 3.3: The TRRF-INV model outputs for the synthetic scenario. (a) Probabilistic estimates of tsunami source where the black lines and stars represent the true values. (b) Probabilistic tsunami run-up distribution. The light red area represents the full range of run-up, and the red line represents the median. The black line is true tsunami run-up distribution. The black circles are the input of the TRRF-INV model. (c) The probability density function (red curve) compared to the true run-up (black line) at three locations.

estimates was 8.37% when we only compared the 20 input locations ($NRMSE_p$) and 8.41% when we compared the entire locations ($NRMSE_t$). We defined a success ratio (SR) as a ratio of the number of locations where the true run-up value falls within the range of run-up estimates (light red area in the upper panel of Fig. 3.3b). Moreover, the error (e) of run-up at three key locations (Patache, Iquique, Pisagua, see Fig. 3.1) was calculated by subtracting the true value from the median of the fitted distribution. In the case shown in Fig. 3.3, the TRRF-INV model yields the SR of 88.68% and small errors at three key locations ($|e| \leq 0.2\ m$).

Figure 3.4 summarizes the result of all 200 synthetic scenarios. Overall, the TRRF-INV model provides a reasonable first-order estimates of tsunami source, especially for the moment magnitude M_W ($MAE = 0.04$) and the epicenter latitude LAT ($MAE = 0.09°$) where MAE represents the mean absolute error. Moreover, the TRRF-INV model estimates the tsunami run-up distribution quite well only with the 20 run-up data (mean $SR = 95.16\%$), especially in Iquique ($MAE = 0.12\ m$) and in Pisagua ($MAE = 0.18\ m$). The mean $NRMSE_t$ is about 6.82%, which is similar to the error of the TRRF model itself.

3.6.2 Performance using the 2014 Chile tsunami run-up record

To evaluate the performance of the TRRF-INV model on a real tsunami event, we applied the TRRF-INV model to infer the tsunami source and tsunami run-up distribution from the 2014 Chile tsunami run-up records [14] and then compared our results with the United States Geological Survey (USGS) report, the global Centroid Moment Tensor (gCMT) solution, and the other tsunami inversion model result [4]. To match the resolution of run-up records with the grid interval of the TRRF-INV model (0.004 degrees), we used the mean value if there were more than one run-up record within a grid.

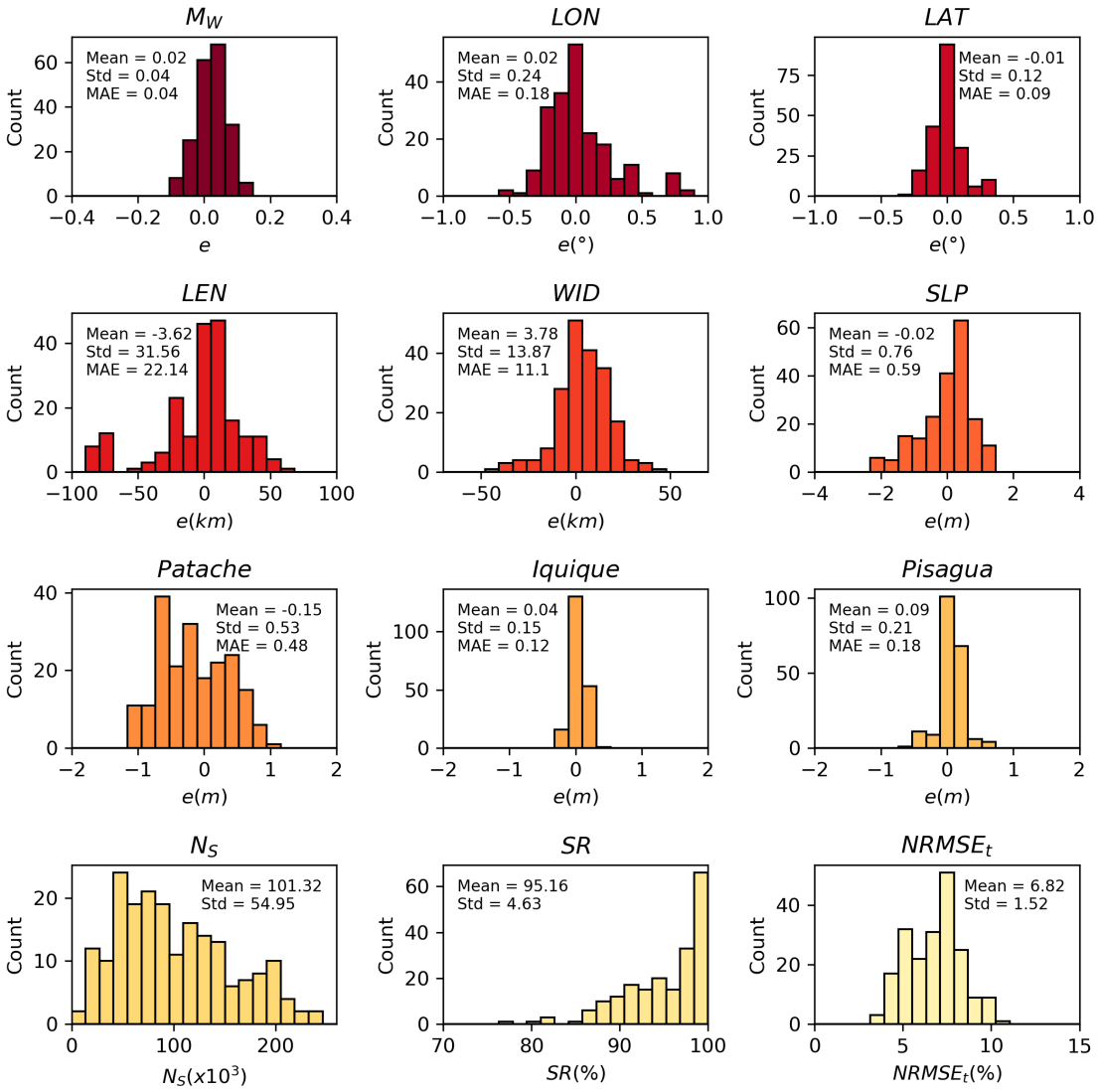

Figure 3.4: Performance of the TRRF-INV model based on 200 synthetic scenarios. The top three rows show the error (e) distribution of moment magnitude (M_W), epicenter longitude (LON), epicenter latitude (LAT), fault length (LEN), fault width (WID), average slip (SLP) and the run-ups at three key locations (Patache, Iquique, Pisagua) where the e is defined as the estimated value minus the true value, and the MAE represents the mean absolute error. The bottom row shows the histograms of the number of filtered scenarios (N_S), success rate (SR), and the normalized root mean squared error ($NRMSE_t$). The mean and the standard deviation (Std) are denoted within each panel.

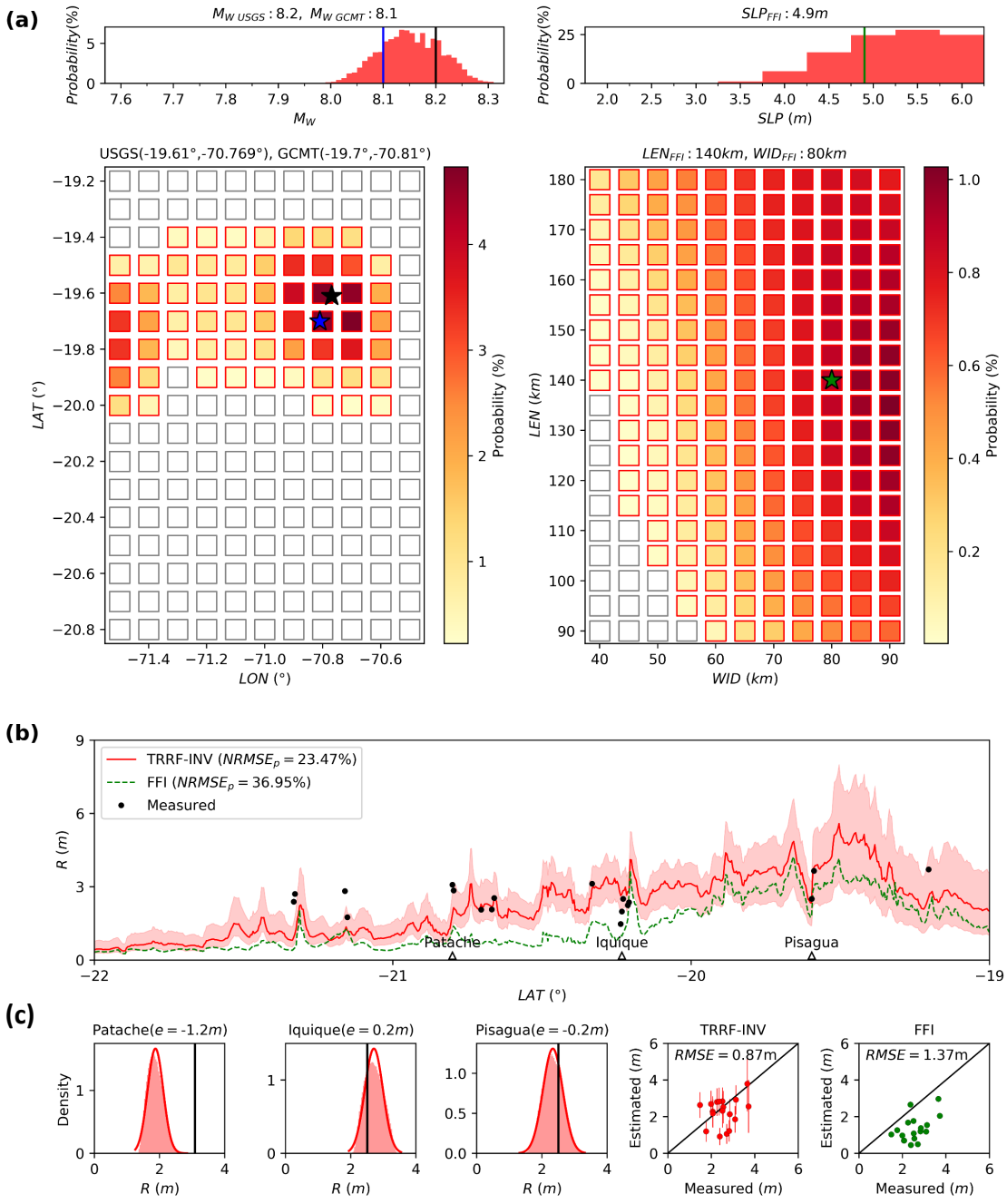

Figure 3.5: The TRRF-INV model outputs for the 2014 Iquique tsunami run-up records. (Continued on the following page.)

Figure 3.5: (a) Probabilistic estimates of tsunami source. The black line and star represent the United States Geological Survey (USGS) report result. The blue line and star represent the global Centroid Moment Tensor (GCMT) solution. The green line and star represent the An et al. [4]'s finite fault inversion (FFI) model result. (b) A probabilistic tsunami run-up distribution. The light red area represents the full range of run-up, and the red line represents the median. The green dashed line is a tsunami run-up distribution based on the FFI source, and the black circles are the 2014 Iquique tsunami run-up records. (c) The probability density function (red curve) compared to the measured run-up (black line) at three key locations (left three). The comparison of run-up between observation and the estimates of TRRF-INV model (red) and FFI (green), respectively (right two).

Figure 3.5 shows the outputs of the TRRF-INV model when using the 2014 Chile tsunami run-up records [14] as inputs. As shown in Figure 3.5a, the estimated M_W ($= 8.13$) falls within the range between the M_W of gCMT and that of USGS. The estimated epicenter $(-19.7°, -70.7°)$ strongly agrees with the epicenter of USGS and that of gCMT. The relatively large probability, though not the largest, was shown near the plate boundary $(-19.8°, -71.5°)$. Since there is no true value for the fault geometry (LEN, WID, SLP), we compared the TRRF-INV model result with the An et al. [4]'s finite fault slip distribution. The estimated slip ($SLP = 5.5\ m$) is slightly larger than the average slip of An et al. [4]. The estimated fault length ($LEN = 135\ km$) and fault width ($WID = 90\ km$) resembles the fault size of An et al. [4]. Note that we defined the average slip and the fault size of the An et al. [4]'s slip distribution based on the finite faults where the slip is larger than 3 m. As shown in Figure 3.5b, the tsunami run-up distribution based on the TRRF-INV model is reasonably matched with the run-up records. The TRRF-INV model underestimates the observed run-up of 1.2 m at Patache, while the estimated run-ups at Iquique and Pisagua agree with the observations very well ($|e| = 0.2\ m$). Note that we used the nearest run-up records to compare the run-ups at three key locations.

To compare the performance of the TRRF-INV model and other tsunami inversion models in estimating the tsunami run-up distribution, we simulated the 2014 Iquique tsunami based

on the An et al. [4]'s tsunami source using the same Basilisk simulation condition used to develop the TRRF model in this study. The tsunami run-up distribution estimated by the An et al. [4]'s tsunami source shows a larger error ($RMSE_p = 1.37\ m$) than the TRRF-INV model result ($RMSE_p = 0.87\ m$), underestimating the tsunami run-ups, especially in the area between the Patache and Iquique, which could be critical in hazard assessment.

3.7 Discussion

Even though there was a couple of synthetic scenarios that showed a poor agreement in a tsunami source and/or run-ups, it is worth noting that the TRRF-INV model provides reasonable first-order estimates in most of the cases, given that the TRRF-INV model only used the 20 run-up data.

In the 200 synthetic-scenario test (Fig. 3.4), the mean absolute error (MAE) of the epicenter latitude (LAT) was twice smaller than that of the epicenter longitude (LON). This may be attributed to the orientation of the coastline and the earthquake fault used in this study. We assumed that the coastline was parallel to the north-south direction, and the strike direction was parallel or inclined up to 20° to the coastline. In this condition, the change of the tsunami run-up distribution is more sensitive to the epicenter latitude (LAT), and thus the TRRF-INV model can distinguish a relatively small change of the epicenter latitude (LAT). Similarly, the fact that the change of the tsunami run-up distribution was more sensitive to the fault width (WID) than the fault length (LEN) can explain the mean absolute error (MAE) of the fault width (WID) that was twice smaller than that of the fault length (LEN).

In Fig. 3.4, the TRRF-INV model shows a relatively large run-up error in Patache even though the average run-up of 20 random synthetic scenarios in Patache was similar to that

in Iquique and Pisagua. The relatively large error in Patache compared to other locations was also found in the case study of the 2014 Iquique tsunami (Fig. 3.5b). We interpret this large error at Patache as a result of the tsunami-source direction that was mostly oriented toward the Iquique-Pisagua area (Table B.1). In this condition, tsunami waves arrived at Patache would have been relatively more affected by the secondary factors such as resonance, edge waves, and other local bathymetry effects [14, 42], which is not directly considered in the TRRF model, than the tsunami waves at Iquique and Pisagua.

We conducted two additional tests to analyze the sensitivity of the TRRF-INV model depending on the number and the uncertainty of run-up records (Fig. 3.6). First, we investigated the performance of the TRRF-INV model depending on the number of run-up records ($N_p = 2, 3, 5, 10, 20, 40$)(Fig. 3.6a). For each number (N_p), a total of 200 scenarios were considered by generating ten random scenarios for each of the 20 base scenarios (Table B.1). The results showed that the error (e) decreased as the number of run-up records (N_p) increased in general. Note that the performance is similar after $N_p = 20$ because of the error the TRRF model itself has. Secondly, we investigated the performance of the TRRF-INV model as the uncertainty of run-up records increased (Fig. 3.6b). The number of run-up records ($N_p = 20$) was fixed, and the uncertainty of run-up values was generated randomly from a normal distribution with a standard deviation ($Std_U = 0m, 0.5m, 1.0m$) and zero mean. For the input run-ups that showed negative values after considering the uncertainty, we replaced them with zeros to prevent unrealistic negative run-up values. The results showed that the error (e) increased as the uncertainty of run-up increased in general. The TRRF-INV model tends to overestimate the moment magnitude (M_W), fault length (LEN), fault width (WID), average slip (SLP), and run-ups at three key locations as the uncertainty increases. This is because the number of input run-ups replaced by zero is likely to increase as the uncertainty increases. These two tests suggest that the optimum conditions for achieving

the convergent performance of the TRRF-INV model in northern Chile are approximately 20 observed run-up records with less than $0.5m$ of uncertainty.

It is important to note that the performance of the TRRF-INV model depends on not only the run-up records but also several other factors such as local bathymetry/topography and earthquake slip complexity. In this study, we only tested the TRRF-INV model for up to about M_W 8.3 earthquake, assuming a uniform slip distribution in northern Chile. Also, the 2014 Iquique earthquake rupture can be considered as a compact and centered slip distribution compared to other large earthquakes [17]. Thus, it is necessary to investigate further the performance of the TRRF-INV model for different regions and larger magnitude earthquakes with more complex slip distributions.

3.8 Conclusions

The capability to understand a tsunami source and its impact is crucial in robust tsunami hazard assessment. To date, several tsunami inversion models have been developed, relying on several types of measured data such as seismic waveform, strong motion, GPS, InSAR, DART, and tide gauge data. Compared to these data, a tsunami run-up record has not been used widely to infer a tsunami source and tsunami run-up distribution because of the computational burden of tsunami forward simulations. In this paper, we propose a new tsunami inversion model, called TRRF-INV model, which can infer a probabilistic near-field tsunami source and a probabilistic tsunami run-up distribution from tsunami run-up records. The TRRF-INV model has overcome the computational burden of tsunami forward simulations by adopting the TRRF model [77] that can rapidly estimate the alongshore tsunami run-up distribution from the earthquake fault parameters. The synthetic tests based on 1,600 scenarios have confirmed that the TRRF-INV model can provide not only reasonable

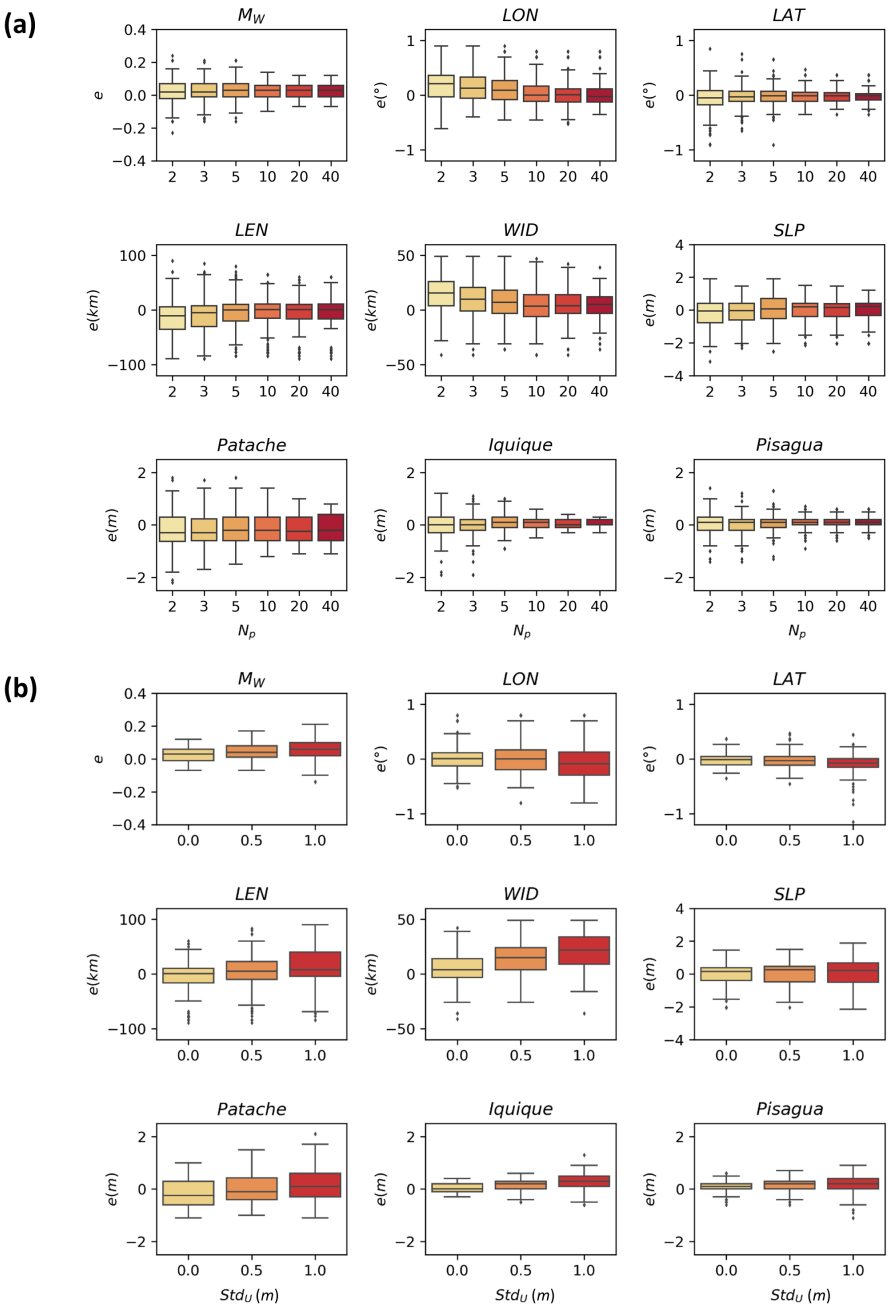

Figure 3.6: Performance of the TRRF-INV model depending on (a) the number of run-up records (N_p) and (b) the uncertainty of run-up records. The error (e) is defined as the estimated value minus the true value. The Std_U represents the standard deviation of uncertainty in meters. Each box-whisker plot consists of 200 random scenarios. The box symbol shows the interquartile range (box boundary), median (horizontal line). The lower(upper) whisker is defined as 1.5 times the interquartile range below(above) the first(third) quartile. The data beyond the whiskers is plotted as an outlier (diamond).

estimates of tsunami source to first order but also accurate tsunami run-up distribution only with 20 run-up values with less than half a meter of uncertainty. The overall agreement on the earthquake magnitude and the epicenter of the 2014 Iquique tsunami event was satisfactory compared to the USGS report and gCMT solution, which supports the effectiveness of the TRRF-INV model. We believe that the TRRF-INV model has the potential for supporting accurate hazard assessment by providing new insights from tsunami run-up records into the tsunami source and its impact. The TRRF-INV model will be beneficial to validate the tsunami source estimated from existing tsunami inversion models, or the TRRF-INV model can serve as a starting point for constraining the tsunami source. Moreover, the TRRF-INV model can be potentially applied to estimate a tsunami source and its impact for ancient events where no data other than run-up estimates derived from sediment deposit data exists.

3.9 Data availability statement

The Basilisk model used to simulate tsunamis is available at http://basilisk.fr/. The bathymetry data of the General Bathymetric Chart of the Ocean (GEBCO) is available at https://www.gebco.net/data_and_products/gridded_bathymetry_data/. The data and codes used in this paper can be accessed via repository: 10.17603/ds2-ej26-wa59.

3.10 Acknowledgments

This publication was prepared by Jun-Whan Lee using Federal funds under award NA18OAR4170083, Virginia Sea Grant College Program Project R/72155L from the National Oceanic and Atmospheric Administration's (NOAA) National Sea Grant College Program, U.S. Department. of Commerce. The statements, findings, conclusions, and recommendations are those of the

3.10. Acknowledgments

author(s) and do not necessarily reflect the views of Virginia Sea Grant, NOAA, or the U.S. Department of Commerce. This material is based upon work partially supported by the National Science Foundation under Grant Nos. 1630099 and 1735139. Any opinions, findings, and conclusions or recommendations expressed in this material are those of the authors and do not necessarily reflect the views of the National Science Foundation. The authors acknowledge Advanced Research Computing at Virginia Tech for providing computational resources and technical support that have contributed to the results reported within this paper. URL: https://198.82.212.30

Chapter 4

Rapid prediction of peak storm surge from tropical cyclone track using machine learning

Jun-Whan Lee [1], Jennifer L. Irish [1,2], Michelle T. Bensi [3], Douglas C. Marcy [4]

[1] Department of Civil and Environmental Engineering, Virginia Tech, 750 Drillfield Dr, Blacksburg, VA, 24061, USA

[2] Center for Coastal Studies, Virginia Tech, 926 W Campus Dr, Blacksburg, VA 24061, USA

[3] Department of Civil and Environmental Engineering, University of Maryland, College Park, MD 20742, USA

[4] NOAA Office for Coastal Management, 2234 S. Hobson Avenue, Charleston, SC 29405, USA

4.1 Abstract

Rapid and accurate prediction of peak storm surges across an extensive coastal region is necessary to protect coastal communities' life and property. Significant advances in high-fidelity, physics-based numerical models have been made over the last two decades, but use of these models for probabilistic forecasting and probabilistic hazard assessment is computationally intensive . Several surrogate modeling approaches based on existing databases of high-fidelity synthetic storm surge simulations have been recently suggested to reduce computational burden without substantial loss of accuracy. In these previous studies, however, the surrogate modeling approaches relied on a tropical cyclone condition at one moment (usually at or near landfall), which is not always most correlated with the peak storm surge. In this study, a new one-dimensional convolutional neural network model combined with principal component analysis and a k-means clustering (C1PKNet) model is presented that can rapidly predict peak storm surge across an extensive coastal region from time-series of tropical cyclone conditions, namely the storm track. The C1PKNet model was trained and cross-validated for the Chesapeake Bay area of the United States using the North Atlantic Coast Comprehensive Study database of the US Army Corps of Engineers, containing 1031 synthetic tropical cyclones, including both landfalling and bypassing storms. Moreover, the performance of the C1PKNet model was evaluated based on observations from three historical hurricanes (Hurricane Isabel in 2003, Hurricane Irene in 2011, and Hurricane Sandy in 2012). The results indicate that the C1PKNet model is computationally efficient and can predict peak storm surges for any tropical cyclone condition. We believe that this new surrogate model can enhance coastal resilience by providing rapid storm surge predictions.

4.2 Introduction

Storm surge by tropical cyclone (TC) is one of the most devastating threats to coastal communities in the United States (US), which has cost hundreds of billions of dollars in economic damage and is responsible for about half of the fatalities from Atlantic TCs (1963-2012) [113]. Historically, the US's costliest natural disaster is Hurricane Katrina (2005), where the storm surge exceeded 7.5 m above sea level, causing at least $108 billion of property damage [10, 116]. Furthermore, the single deadliest natural disaster in the US is Hurricane Galveston (1900) that caused at least 8,000 deaths, and most of the deaths are known to occur when the storm surge inundated [10]. To mitigate the damages, several studies have emphasized the needs for a rapid and accurate storm surge model that can support not only a probabilistic storm surge forecast where a large number of simulations is required to deal with the storm track's uncertainty [39], but also a probabilistic storm surge hazard assessment where a large number of simulations is required to account for the uncertainty in hazard estimation [115].

Physics-based numerical models, such as SLOSH [Sea, Lake, and Overland Surges from Hurricanes, 60] and ADCIRC [ADvanced CIRCulation, 86], are being widely used to predict storm surges. Over the last several decades, significant advances in physics-based models allow accurate simulation of storm surge at high resolution and thus with high accuracy. The problem, however, is that a high-fidelity physics-based numerical model is computationally intensive for probabilistic forecasting and probabilistic hazard assessment, even with the parallelization techniques. For this reason, the National Hurricane Center's operational probabilistic forecast system (P-Surge) relies on a large number of coarse-grid simulations based on SLOSH that neglects key physical components such as waves and nonlinear advection [66]. Moreover, due to the computational burden of the high-fidelity physics-based numerical model, most of the probabilistic storm surge hazard assessments have been rely-

ing on a large number of storms based on low-fidelity models [e.g., 82] or only on a limited number of storms based on high-fidelity models [e.g., 70].

Over the last decade, data-driven surrogate modeling based on the high-fidelity synthetic storm simulation database [e.g., 20, 58, 65] is getting more and more attention as several studies have shown that the surrogate model can provide storm surge predictions without substantial loss of accuracy while drastically reducing the computational time compared to the high-fidelity physics-based numerical simulation. One example is a surrogate model based on surge response functions (SRFs) that are physics-based algebraic expressions of storm surge at a specific location of interest [59, 131, 136]. Moreover, a multilayer perceptron (MLP, a class of feedforward artificial neural network) or support vector regression (SVR) were used to develop surrogate models [2, 48, 67]. However, these surrogate modeling approaches are inefficient to apply for an extensive coastal region, including a large number of points, and cannot consider overland locations. For these reasons, several studies developed surrogate models based on moving least squares response surface [134, 135], kriging (also referred to as Gaussian process regression) with principal component analysis (PCA) [9, 61, 62, 72, 154], and a MLP with PCA [9], which are applicable to high-dimensional output including overland locations.

The aforementioned multi-output surrogate models have only considered a tropical cyclone (TC) condition at one moment (usually at landfall) as model input. This type of point-based input, which does not take advantage of the temporal variation in TC conditions, limits the surrogate model unable to distinguish the storms with the same conditions at landfall but with different conditions before and/or after landfall. Besides, historical records indicate that the peak storm surge is not always most correlated with TC parameters at landfall [99]. Secondly, in the studies of the North Atlantic coast, bypassing-track storms, approximately 40% of the database [20]), were excluded in surrogate modeling [72, 154]. The lack of capacity

to respond to bypassing-track storms is a major problem for surrogate models in that TCs, such as Hurricane Irene (2011), cannot be addressed. Lastly, the aforementioned multi-output surrogate models' performance was only evaluated using cross-validation based on the synthetic TCs. The cross-validation approach is often used to evaluate the surrogate model's performance over the entire database because there is an advantage that does not require new observations [62]. However, especially when using the database where the synthetic storms are systemically designed [e.g., 20, 58, 65], the cross-validation can exaggerate the performance of the surrogate model because the performance is evaluated only with storms similar to those already used for surrogate modeling (e.g. a storm that has the same storm track and a small difference in other parameter values).

This study introduces a new surrogate model that can rapidly predict peak storm surges across an extensive coastal region from a time-series of TC parameters: hereafter referred to as the C1PKNet model that stands for one-dimensional convolutional neural network model combined with principal component analysis and k-means clustering. The variation of TC conditions over time is incorporated into the C1PKNet model by applying a convolutional neural network (CNN), a class of deep neural networks widely used in several classification and regression applications. The main advantage of CNN is that it can capture spatial and/or temporal dependencies by preserving data structures in a process called feature learning, which is a distinct point from MLP. Since the TC conditions are time-series data, one-dimensional CNN where the kernel (or filter) slides along time dimension is used to capture the features of TC conditions over time. To increase CNN's efficiency and accuracy, high-dimensional output (peak storm surges) is grouped among geospatial points with similar peak storm surge responses using k-means clustering, and the data dimensionality of the grouped points is reduced using PCA before CNN training. This study's main contributions are listed as follows: (1) Our work is the first attempt to incorporate the variation of TC

conditions over time in surrogate modeling. (2) We included landfalling-track storms as well as bypassing-track storms in surrogate modeling. (3) We not only evaluated the performance of the C1PKNet model based on a cross-validation approach but also validated the C1PKNet model with historical peak storm surge observations.

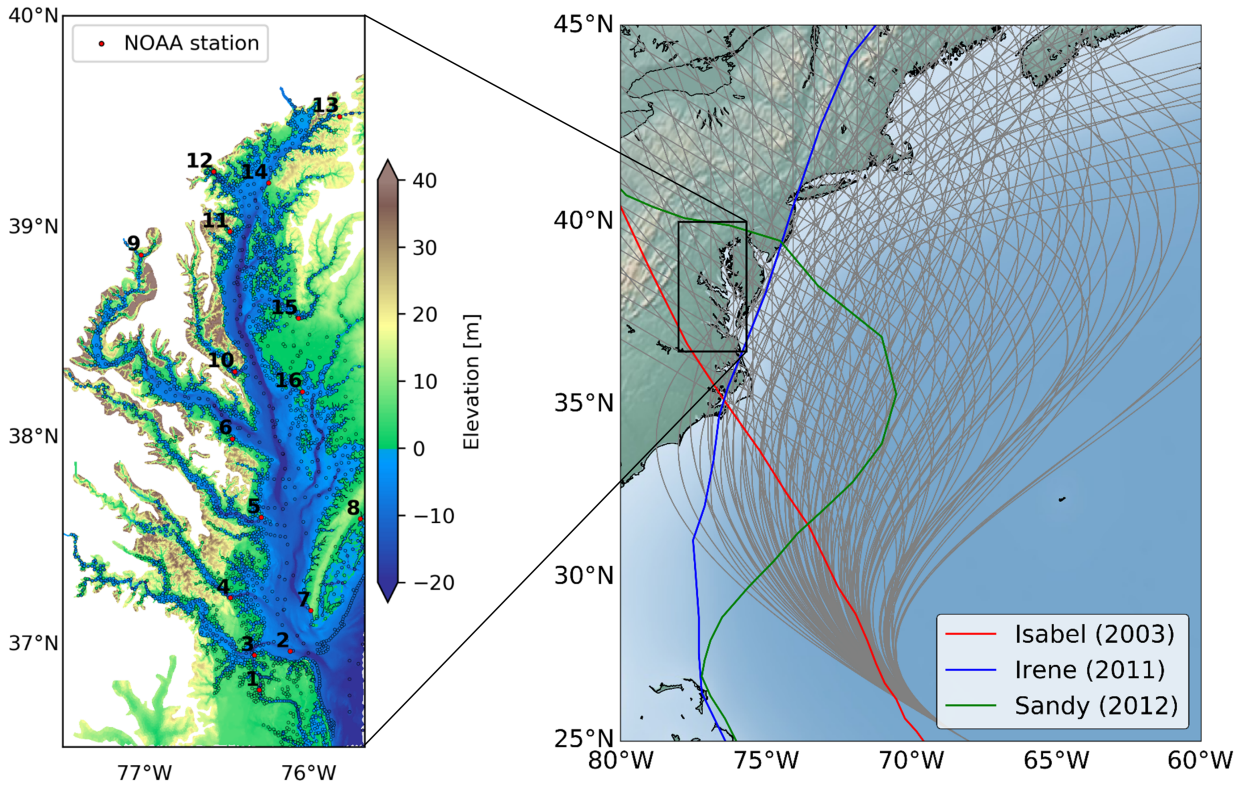

Figure 4.1: Location map of the Chesapeake Bay. In the left map, the empty circles are the save points of NACCS, and the red circles represent the NOAA stations. The map is colored with the topography and bathymetry data that were used in NACCS. The elevation values refer to the mean sea level (MSL). In the right map, the gray lines are the synthetic tropical cyclone (TC) tracks of NACCS. The red, blue, and green lines represent the storm tracks of Hurricane Isabel in 2003, Hurricane Irene in 2011, and Hurricane Sandy in 2012, respectively.

Table 4.1: NOAA Station ID and its location

No.	NAME	Station ID	LAT(°)	LON(°)
1	Money Point, VA	8639348	36.7783	-76.3017
2	Chesapeake Bay Bridge Tunnel, VA	8638863	36.9667	-76.1133
3	Sewells Point, VA	8638610	36.9467	-76.3300
4	Yorktown USCG Training Center, VA	8637689	37.2267	-76.4783
5	Windmill Point, VA	8636580	37.6167	-76.2900
6	Lewisetta, VA	8635750	37.9950	-76.4650
7	Kiptopeke, VA	8632200	37.1650	-75.9883
8	Wachapreague, VA	8631044	37.6083	-75.6850
9	Washington, DC	8594900	38.8733	-77.0217
10	Solomons Island, MD	8577330	38.3167	-76.4500
11	Annapolis, MD	8575512	38.9833	-76.4817
12	Baltimore, MD	8574680	39.2667	-76.5800
13	Chesapeake City, MD	8573927	39.5267	-75.8100
14	Tolchester Beach, MD	8573364	39.2133	-76.2450
15	Cambridge, MD	8571892	38.5717	-76.0617
16	Bishops Head, MD	8571421	38.2200	-76.0383

4.3 Methods

4.3.1 Study area

The Chesapeake Bay, the largest estuary in the United States, is one of the most complex coastal plain estuaries in the world that consists of numerous tributaries, embayments, marshes, islands, and channels [127] (Figure 4.1). This area is vulnerable to flooding due to storm surges, as there are many geographically low-lying areas on the coastal plains surrounding Chesapeake Bay [81]. Hurricane Isabel (2003) is a prime example that affected the Chesapeake Bay, where the storm surge reached 2.5 m in the upper Chesapeake Bay, causing about $3.37 billion in losses [101, 128]. Even though storm surges from Hurricane Irene (2011) and Hurricane Sandy (2012) were not as large as the storm surges from Hurricane Isabel (2003) in the Chesapeake Bay, the expected storm surges by two hurricanes were also large enough to issue voluntary and mandatory evacuations for low-lying and oceanfront

areas around the Chesapeake Bay.

4.3.2 Data

The C1PKNet model was developed based on the North Atlantic Comprehensive Coastal Study (NACCS) database of the US Army Corps of Engineers [20]. The NACCS database contains storm surge simulations for 1050 synthetic tropical cyclones (TCs) in the North Atlantic region (Virginia to Maine), computed using coupled high-fidelity physics-based numerical model composed of ADCIRC [86, ADvanced CIRCulation] and STWAVE [90, STeady-state spectral WAVE model]. A planetary boundary layer (PBL) numerical model is used to generate wind and pressure fields [139]. The model grids consist of 3.1 million nodes and 6.2 million elements, where the smallest element's nodal spacing is approximately 10 m. A time-series of model results are saved for a subset of points (18,977 save-point locations). The 1050 synthetic TCs of NACCS are selected using a joint probability method with optimized sampling (JPM-OS) [115, 143]. More details on modeling and storm selection can be found in Cialone et al. [20, 21], Nadal-Caraballo et al. [94].

In this study, we used 1031 synthetic TCs that were successfully simulated on storm surge-only conditions (excluding astronomical tide). These synthetic TCs include both landfalling-track storms and bypassing-track storms (see gray lines in Figure 4.1). We used a peak storm surge above mean sea level (MSL) of 3,111 save-point locations within the study area (see empty circles in Figure 4.1). Out of these points, 21% of points are overland points (where the land elevation is higher than the mean sea level), and 79% of points are subaqueous points (where the land elevation is lower than the mean sea level). We filtered out the unrealistic peak storm surge values that are larger than 10 m. Following Taflanidis et al. [134]'s approach, the missing peak storm surge values of the overland points and the peak

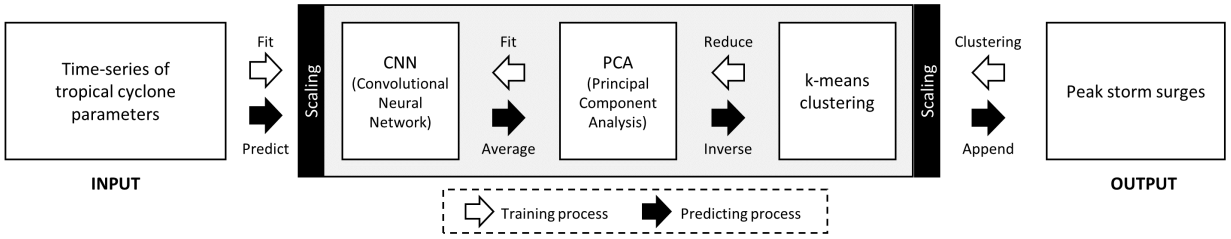

Figure 4.2: Computational flow of C1PKNet model.

storm surge for the dry points (the overland points that are not inundated) were filled with the peak storm surge of the nearest inundated overland point. The missing peak storm surges at subaqueous points were filled with the nearest subaqueous point's peak storm surge.

4.3.3 Model

Figure 4.2 shows the computational flow of the C1PKNet model. The inputs are the time-series of TC parameters (latitude LAT, longitude LON, heading direction θ, central pressure C_p, radius of maximum winds R_{max}, and translation speed V_f). Note that two other TC parameters provided by NACCS (Holland B and a scale pressure radius) correlated to other TC parameters were not used in surrogate modeling to make the training process faster. Holland B is a function of the radius of maximum winds and latitude of storm location, and the scale pressure radius is a function of the radius of maximum winds. NACCS defined reference points to the location 250 km away from the landfall location for the landfalling-track storms, and to the location when the storm exits the pre-defined impact region for the bypassing-track storm [20]. Following the definition of the reference point, we used the time range between 30 hours before passing the reference point to 9 hours after passing the reference point with a 1-hour interval, which is the most extended time range that we can extract from the entire 1031 synthetic TCs. The outputs are the peak storm surges of 3,111 save-point locations mentioned in section 4.3.2.

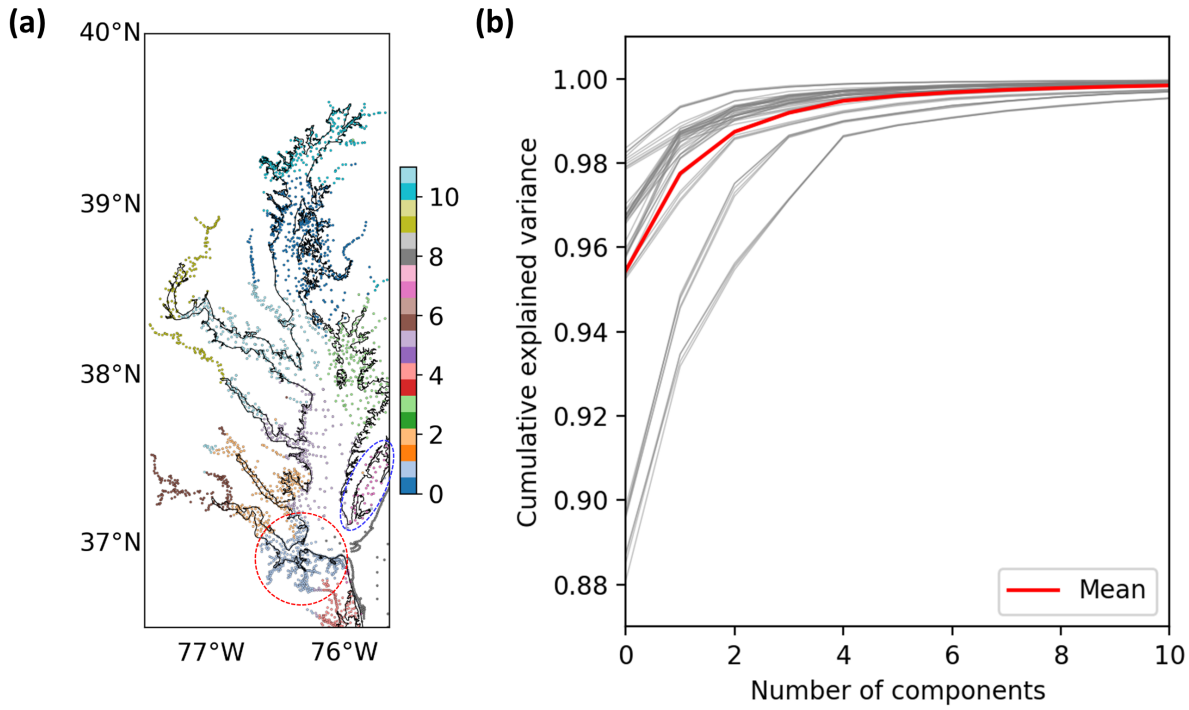

Figure 4.3: (a) Spatial distribution of clusters for the first outer-fold. Each color represents a different cluster. The Red dashed circle is the Hampton-Norfolk area, and the blue dashed ellipse is the Hog Island bay-Mockhorn bay area. (b) Variation of cumulative explained variance against the number of principal components. The gray lines represent the results according to each outer-fold and cluster. The red line is the mean value.

The C1PKNet model consists of three components: (1) k-means clustering that groups the save-point locations showing similar patterns of peak storm surges for TC scenarios, (2) principal component analysis (PCA) that reduces the spatial dimension for each cluster, and (3) one-dimensional convolutional neural network (CNN) that captures the relationships between the time-series of TC parameters and the principal components. Note that the input and output data were standardized by subtracting the mean and then scaling to unit variance. Once the C1PKNet model is trained, the model can predict the peak storm surges at 3,111 save-point locations from any TC parameter conditions within a few seconds. The C1PKNet model considers the point where the predicted peak storm surge value is smaller than the location elevation as a dry point (not inundated). The C1PKNet model is written

in Python where the k-means clustering and PCA were implemented using scikit-learn [110], and the CNNs were implemented using Keras [19] with a TensorFlow backend.

To prevent biased model evaluation, we trained and validated the C1PKNet model using nested k-fold cross-validation with shuffling (Figure C.1). We set outer 10-fold cross-validation by separating 10% of TCs as a test set. At every iteration of the outer fold, inner 5-fold cross-validation was conducted where 20% of TCs were separated as a validation set. For each outer fold, the average of five inner-fold estimates is considered as the final output of the C1PKNet model.

In this study, the number of clusters of the C1PKNet model was set to 12 considering Chesapeake Bay's geographic features. One of the criteria was to separate the Hampton-Norfolk area and Hog Island bay-Mockhorn bay area, and we found that at least 12 clusters are required to separate these two areas (Figure 4.3a). The entire clusters for 10 outer-folds can be found in Figure C.2. For each cluster of each outer fold, the PCA was conducted to analyze the cumulative explained variance (Figure 4.3b). The number of principal components of the C1PKNet model was set to 5, explaining more than 99% of the variance of the peak storm surges of the clustered points on average.

Figure 4.4 shows the detailed CNN architecture of the C1PKNet model where the inputs are the scaled time-series (40 hours) of six TC parameters (LAT, LON, θ, C_p, R_{max}, V_f), and the outputs are five principal components. We put a batch normalization layer [56] after one-dimensional convolutional layer to improve the training efficiency and stability. We also put a dropout layer [132] after a dense layer to prevent over-fitting during training. In this study, We propose the hyperparameters (number of layers, filter size, kernel size, pool size, number of neurons) as shown in Figure 4.4, which were determined considering both accuracy and efficiency. We used Adam optimizer [68] with a learning rate of 0.01, and mean squared error (MSE) as a loss function. The maximum epoch was set to 10,000, and the

CNN model training was set to stop early when the MSE of the validation set is not reduced for 100 epochs. The best CNN model that showed the minimum MSE for the validation set was saved as a final trained CNN model.

4.4 Results

4.4.1 Synthetic tropical cyclones

To quantify the performance of the C1PKNet model based on 1031 synthetic tropical cyclones (TCs), we used the 10-fold cross-validation method as mentioned in Section 4.3.3. For each outer fold, the 60 CNNs (5 inner folds $\times$ 12 clusters) were trained, and the C1PKNet model predicted peak storm surges for the test set that was never used in training. This process was repeated 10 times to test the entire 1031 synthetic TCs. Here, we will first present the detailed result based on one of the synthetic TCs (Figure 4.5) and then highlight the overall performance of the C1PKNet model based on the points where the C1PKNet model correctly predicted the wet/dry condition (Figure 4.6) and the points where the C1PKNet model incorrectly predicted the wet/dry condition (Figure 4.7). The error of the C1PKNet model ($\Delta\eta_n^i$) is represented as follows:

$$\Delta\eta_n^i = \eta_{C1PKNet,n}^i - \eta_{NACCS,n}^i \tag{4.1}$$

where i is the scenario number, n is the point number, $\eta_{C1PKNet,n}^i$ is the peak storm surge predicted by the C1PKNet model, and $\eta_{NACCS,n}^i$ is the peak storm surge of NACCS. The performance of the C1PKNet for each synthetic TC is represented by a root mean square error ($RMSE$) and mean bias error (MBE):

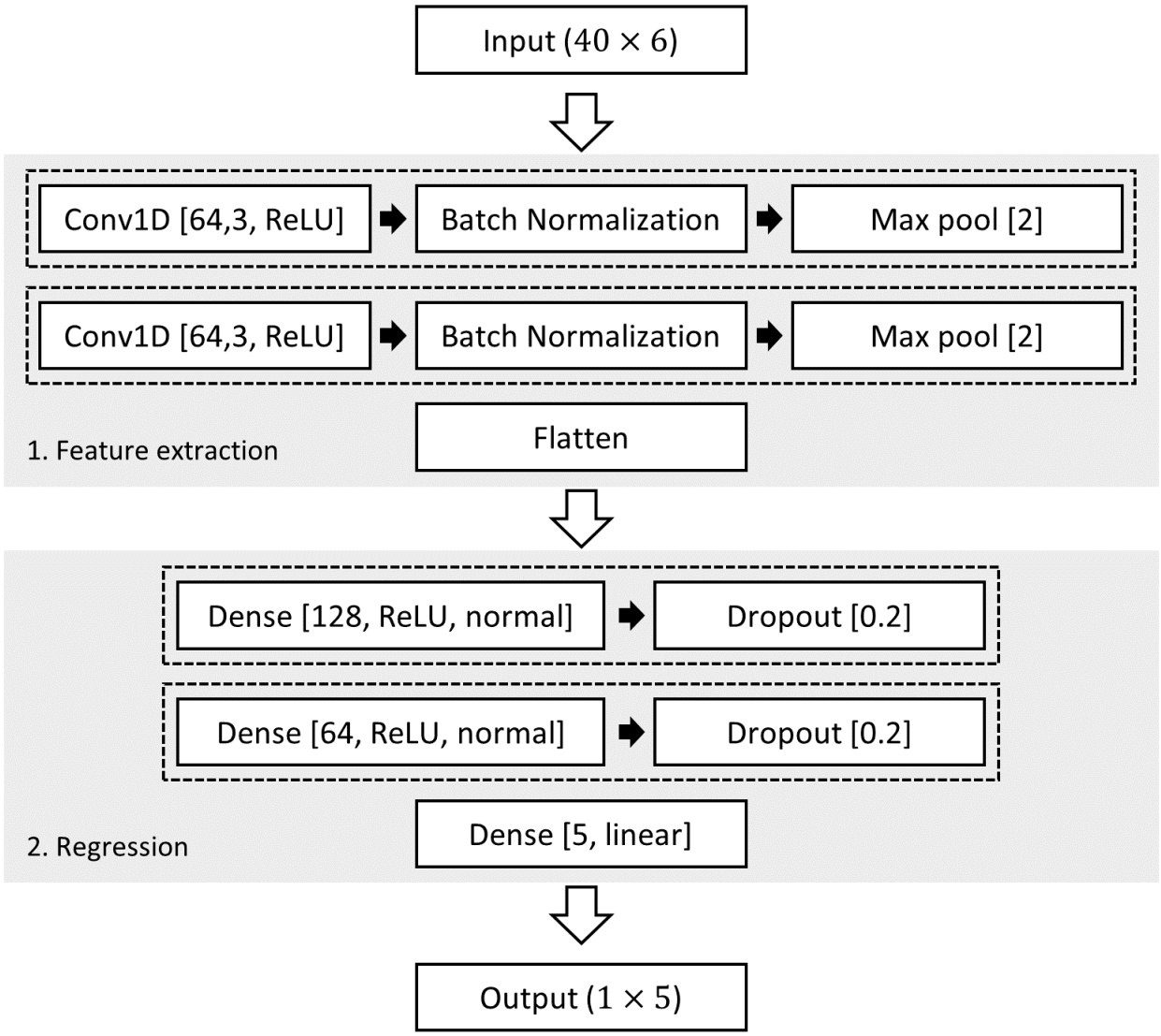

Figure 4.4: Convolutional neural network (CNN) architecture. Conv1D [64,3, ReLU] represents the 1-dimensional convolutional layer where the dimensionality of the output space (filter) is 64, the kernel size is 3, and the activation function is rectified linear activation function (ReLU). Max pool [2] represents the max pooling operation for 1-dimensional data where the max pooling window size is 2. Dense [128, ReLU, normal] represents the densely-connected neural network layer where the dimensionality of the output space is 128, the activation function is rectified linear activation function (ReLU), and the normal distribution is used as an initializer for the kernel weights matrix. Dropout [0.2] represents the dropout layer where the drop rate is 0.2. Dense [5, linear] represents the densely-connected neural network layer where the dimensionality of the output space is 5, and the activation function is a linear activation function.

$$RMSE^i = \sqrt{\frac{1}{N_p}\sum_{n=1}^{N_p}[\Delta\eta_n^i]^2} \tag{4.2}$$

$$MBE^i = \frac{1}{N_p}\sum_{n=1}^{N_p}\Delta\eta_n^i \tag{4.3}$$

where N_p is a total number of save points.

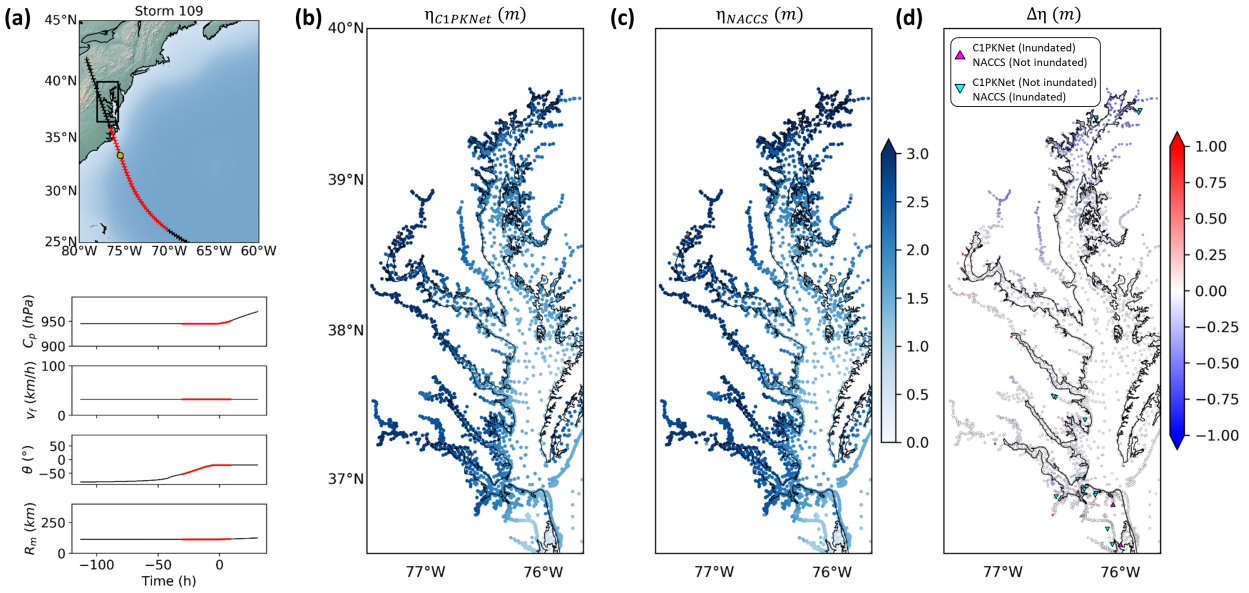

Figure 4.5: Synthetic scenario result. (a) Time series of tropical cyclone (TC) parameters where C_p is the central pressure, V_f is the translation speed, θ is the heading direction, and R_{max} is the radius of maximum winds. The yellow circle in the map represents the reference point that is 250 km away from the landfall point. The red lines are the 40 hours of TC parameters used as inputs of the C1PKNet model. The time of zero is set to the time when the TC passes the reference point. (b) Peak storm surges predicted by the C1PKNet model. (c) Peak storm surges of NACCS. (d) The difference between the C1PKNet predictions and the NACCS predictions. The magenta and green triangles represent the points where the C1PKNet model incorrectly predicted the wet/dry condition compared to NACCS.

Figure 4.5 shows the one example result (Scenario 109) where the TC parameters are similar to Hurricane Isabel in 2003. The TC made landfall near Cape Lookout (North Carolina,

USA), with a central pressure (C_p) of 945 hPa, translation speed (V_f) of 32 km/h, heading direction (θ) of $-20°$, and radius of maximum winds (R_{max}) of 113 km (Figure 4.5a). Overall, the peak storm surges predicted by the C1PKNet model agree well with the peak storm surges of NACCS that were not used during the C1PKNet model training ($RMSE^{109} = 0.17$ m, Figure 4.5b). The C1PKNet model slightly underestimated the peak storm surges, especially at the northern save points ($MBE^{109} = -0.09$ m). The C1PKNet model incorrectly predicted the wet/dry condition for 14 overland points (2% of the overland points).

Figure 4.6a shows the error in peak storm surge estimated using the C1PKNet model versus the peak storm surge of NACCS for the entire data (1031 synthetic storm scenarios $\times$ 3111 save points). Note that the points in wet conditions (where the peak storm surge elevation is higher than the land elevation) by both the C1PKNet model and NACCS are considered in Figure 4.6. Overall, the peak storm surge errors ($\Delta\eta$) are aligned well with the zero error line. For the subaqueous locations, most of the large errors ($|\Delta\eta| > 1$ m) occurred in the range of 2 m and 4 m of peak storm surge (η_{NACCS}). The largest error (-6.3 m) occurred at point 13256 by synthetic scenario 50 where the peak storm surge of NACCS (η_{NACCS}) was 7.02 m. We believe that this largest error is not due to the C1PKNet model but due to the unstable numerical simulation of NACCS because the peak storm surge at point 13256 by synthetic scenario 50 was distinctively larger compared to that of the other similar TCs (Figure C.3). For the overland locations, most of the large overestimation errors ($\Delta\eta > 1$ m) occurred in the range of 1 m and 2 m of peak storm surge (η_{NACCS}), while most of the large underestimation errors ($\Delta\eta < -1$ m) occurred in the range of 2 m and 4 m of peak storm surge (η_{NACCS}).

Since most of the peak storm surge values are concentrated in the range of 0 m and 2 m as shown in Figure 4.6a, the $RMSE$ based on the entire data can mislead the actual performance of the C1PKNet model as mentioned in Al Kajbaf and Bensi [2]. Therefore, we

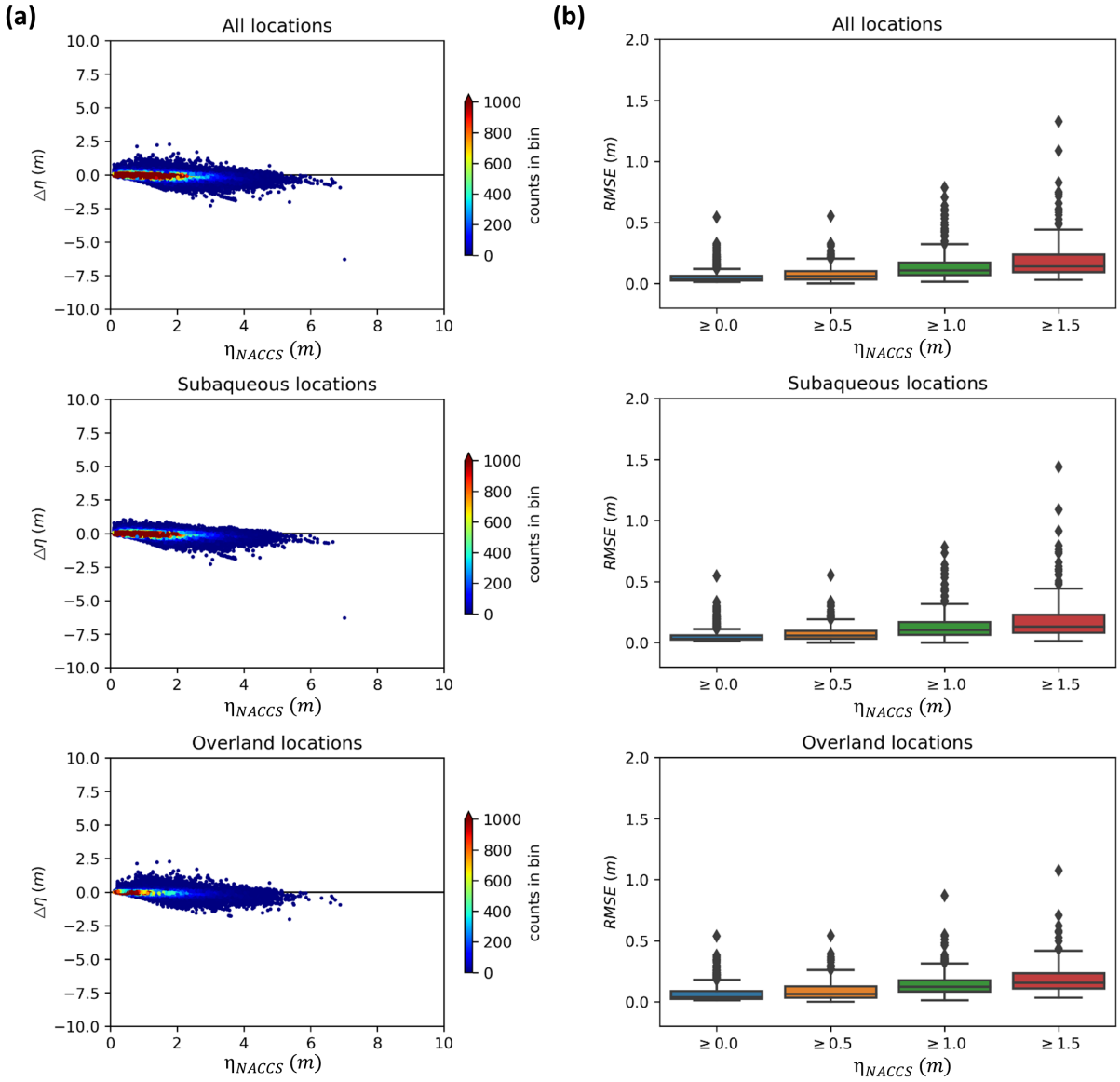

Figure 4.6: Performance of the C1PKNet model based on 1,031 synthetic storm scenarios. (a) The density scatter plot that shows the error distribution depending on the peak storm surge of NACCS. The black horizontal line represents the zero error line. (b) The root mean square error (RMSE) of peak storm surges for individual storms as the lower bound truncation threshold increases from 0 m to 1.5 m. The box symbol shows the interquartile range (box boundary), median (horizontal line). The lower(upper) whisker is defined as 1.5 times the interquartile range below(above) the first(third) quartile. The data beyond the whiskers are plotted as an outlier (diamond).

Table 4.2: The number of tropical cyclone (TC) scenarios and root mean square error (RMSE) depending on the lower bound truncation threshold.

		TC scenario	RMSE (m)				
	Threshold	count	min	25%	50%	75%	max
All locations	0 m	1031	0.01	0.02	0.03	0.06	0.54
	0.5 m	726	0.00	0.03	0.06	0.10	0.55
	1 m	424	0.02	0.07	0.11	0.17	0.78
	1.5 m	308	0.03	0.09	0.14	0.24	1.32
Subaqueous locations	0 m	1031	0.01	0.02	0.03	0.06	0.55
	0.5 m	726	0.00	0.03	0.06	0.10	0.55
	1 m	421	0.00	0.06	0.10	0.17	0.78
	1.5 m	303	0.01	0.08	0.13	0.23	1.44
Overland locations	0 m	1031	0.01	0.03	0.04	0.09	0.54
	0.5 m	695	0.00	0.03	0.06	0.13	0.54
	1 m	403	0.01	0.08	0.12	0.18	0.87
	1.5 m	299	0.03	0.11	0.15	0.23	1.07

calculated the $RMSE$ of peak storm surges for individual storms as the lower bound truncation threshold increases from 0 m to 1.5 m with 0.5 m intervals (Figure 4.6b). As the lower bound truncation threshold increases, the median of $RMSE$ increases from 0.03 m to 0.14 m, and the range of $RMSE$ also increases. Table 4.2 summarizes the $RMSE$ and shows how many scenarios are within the thresholds. For example, the peak storm surge above 1.5 m was shown at least at one point in 308 synthetic scenarios out of 1031 synthetic scenarios (about 30% of scenarios). The $RMSE$ based only on the overland points was similar to the $RMSE$ based only on the subaqueous points.

Figure 4.7 shows the performance of how well the C1PKNet model predicts the wet/dry condition. First, we calculated the percentage of scenarios where the C1PKNet model incorrectly predicts each point location's wet/dry condition. Figure 4.7a is the case where the point is inundated by the C1PKNet model but not in NACCS (hereafter case 1). Figure 4.7b is the case where the point is inundated in NACCS but not by the C1PKNet model (hereafter case 2). Overall, the C1PKNet model incorrectly predicts the wet/dry condition only for a few scenarios. In case 1, the median of the percentage of the scenarios is 0.3%,

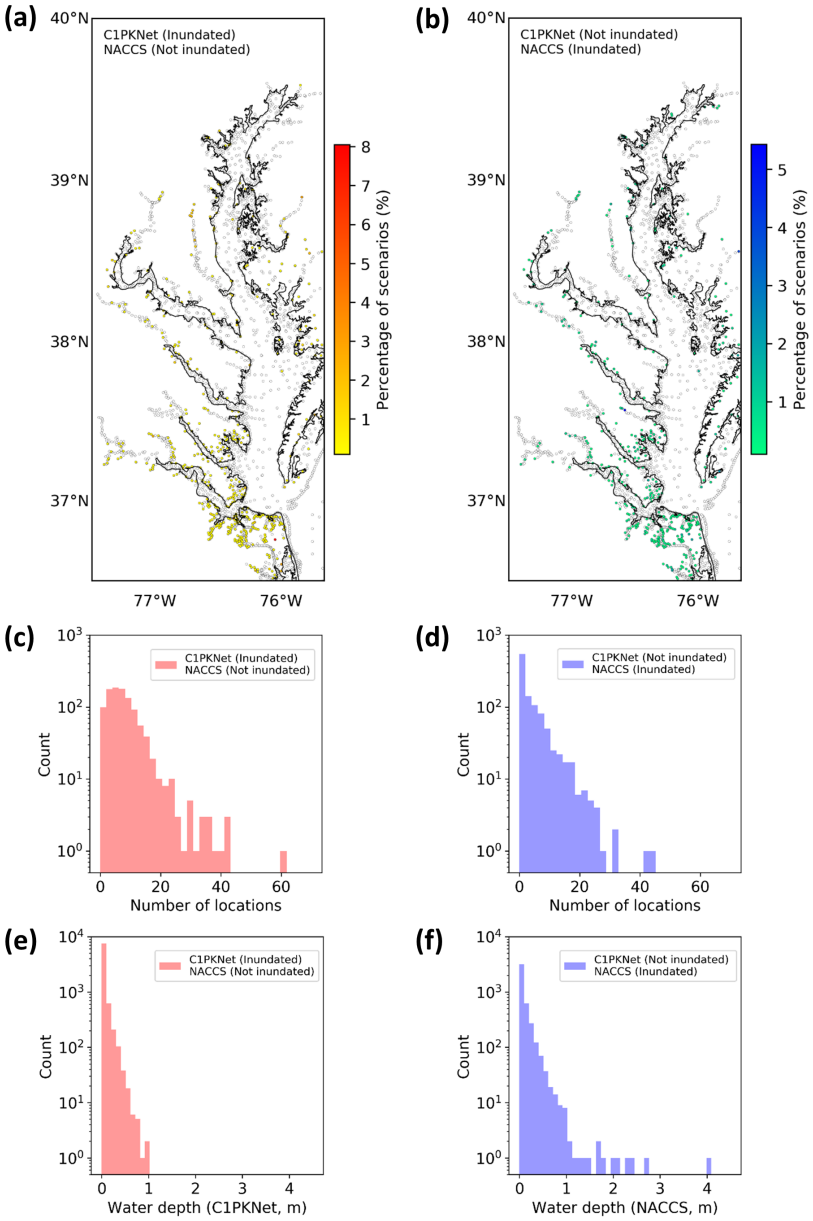

Figure 4.7: Performance on how well the C1PKNet model predicts the wet/dry condition. (a) The percentage of TC scenarios where the point is flooded by C1PKNet model simulation and not in the NACCS database. (b) The percentage of TC scenarios where the point is not flooded in the NACCS database and not by C1PKNet model simulation. (c,d) Histogram of the number of locations where the C1PKNet model incorrectly predicts the wet/dry condition for each scenario. (e,f) Histogram of the water depth based only on the data where the C1PKNet model incorrectly predicts the wet/dry condition.

and the maximum percentage of the scenarios is 8%. In case 2, the median of the percentage of scenarios is 0.4%, and the maximum percentage of the scenarios is 5.4%. In both cases, most of the points where the wet/dry condition was incorrectly predicted were located in the low-lying area of coastal Virginia (below 37.5°N). Secondly, we counted the number of save points where the wet/dry condition was incorrectly predicted for each synthetic TC scenario (Figures 4.7c and d). There were less than 20 save points in both cases where the C1PKNet model incorrectly predicts the wet/dry condition for more than 96% of TC scenarios. The median of case 1 is 7 save points, while that of case 2 is 2 save points. Lastly, we plotted the water depth frequency when the C1PKNet model incorrectly predicted the wet/dry condition (Figures 4.7e and f). The results show that more than 98% of water depth when the C1PKNet model incorrectly predicts the wet/dry condition was less than 0.5 m. For case 1, the water depth was less than 1 m for every data. For case 2, there were 16 data where the water depth was larger than 1 m. In summary, the C1PKNet model predicted the wet/dry condition well, considering the number of storms and the number of points. Moreover, even when the C1PKNet model incorrectly predicted the wet/dry condition, the water depth was smaller than 0.5 m in most cases.

4.4.2 Historical hurricanes

To test the C1PKNet model based on real storm cases, we simulated three historical hurricanes (2003 Isabel, 2011 Irene, 2012 Sandy). We chose these three hurricanes because each of them shows different hurricane track features. Hurricane Isabel (2003) made landfall on South of the study area (Outer Banks, North Carolina), Hurricane Irene (2011) bypasses the southeastern part of the study area, and Hurricane Sandy (2012) made landfall on North of the study area (Brigantine, New Jersey). The hurricane tracks and the time-series of hurricane parameters are shown in Figure 4.8. The hurricane-parameter data was taken from the

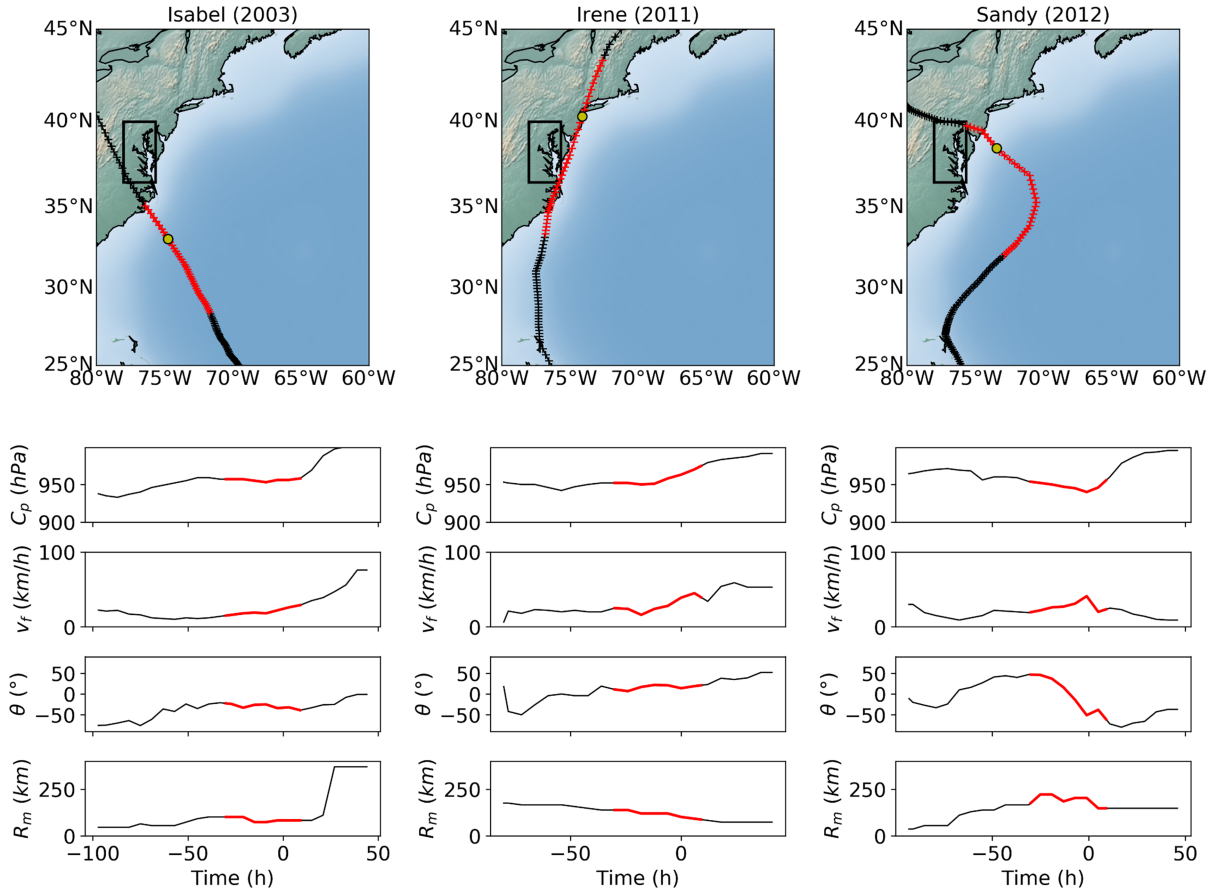

Figure 4.8: Time series of hurricane parameters of Hurricane Isabel in 2003, Hurricane Irene in 2011, and Hurricane Sandy in 2012. In the upper map, the yellow circle represents the reference point. The red lines are the 40 hours of hurricane parameters used as inputs of the C1PKNet model.

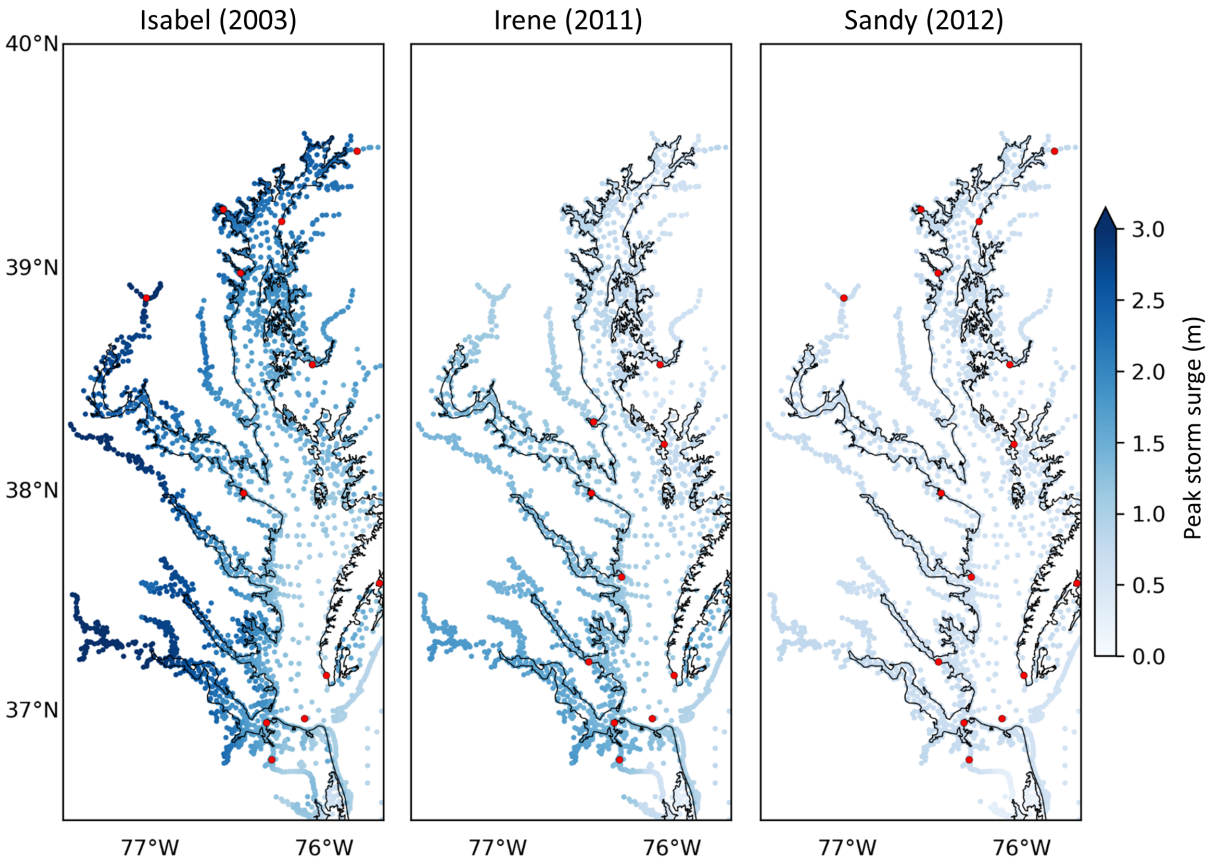

Figure 4.9: Peak storm surges predicted by the C1PKNet model. The red circles represent the NOAA stations where the measured water-level data exists.

extended best track dataset [27], which supplements the second-generate hurricane database (HURDAT2) of the National Hurricane Center (NHC) [73]. Since the dataset is saved in a 6-hour interval, we linearly interpolated the data into a 1-hour interval. Each historical hurricane's reference point was set to the closest point of the interpolated hurricane track to the reference point of the most similar synthetic TC track of NACCS. Based on the reference point, the hurricane parameter values over 40 hours were used as the inputs of the C1PKNet model (Red lines in Figure 4.8).

The C1PKNet simulation results of three historical hurricanes are shown in Figure 4.9. In

this study, we used a cross-validation ensemble (the average of ten trained C1PKNet model predictions) as a final prediction, which is more stable than using the best performing model during 10-fold cross-validation. The maximum value of the peak storm surges was 3.41 m (Hurricane Isabel), 1.88 m (Hurricane Irene), and 0.85 m (Hurricane Sandy), respectively.

Figure 4.10 shows the comparison between the C1PKNet model results and the NOAA stations' observations. The peak storm tides ($\bar{\eta}$) were estimated as follows:

$$\bar{\eta} = \eta_{C1PKNet} + \eta_{Tide} - \eta_{NLR} \tag{4.4}$$

where $\eta_{C1PKNet}$ is a peak storm surge predicted by the C1PKNet model, η_{Tide} is a predicted tide elevation, and η_{NLR} is an astronomical tide bias of NACCS. Note that we set $\eta_{C1PKNet}$ to the peak storm surge at the save point located closest to the NOAA station. The predicted tide data (η_{Tide}) and observed storm tide data were extracted from the NOAA reports [31, 32, 55]. The tidal datum of data was converted from mean lower low water (MLLW) to mean sea level (MSL) using the NOAA Tide and Currents database [102]. The astronomical tide bias data (η_{NLR}) was compiled from the Coastal Hazards System (CHS) of the USACE [95]. Overall, the C1PKNet model predictions matched well with the observations for Hurricane Isabel (2003). The largest underestimation (0.65 m) occurred at the Chesapeake City station. For Hurricane Irene (2011), the C1PKNet model underestimated the large storm tides ($>$ 1.8 m) while overestimated the small storm tides ($<$ 1.8 m). For Hurricane Sandy (2012), the C1PKNet model underestimated the storm tides at all stations between 0.08 m and 0.68 m. We believe that the relatively large underestimation of storm tide shown in the Hurricane Sandy (2012) case is due to sudden changes in hurricane parameters nearby the moment of landfall that were not seen in the synthetic scenarios used for the C1PKNet model training.

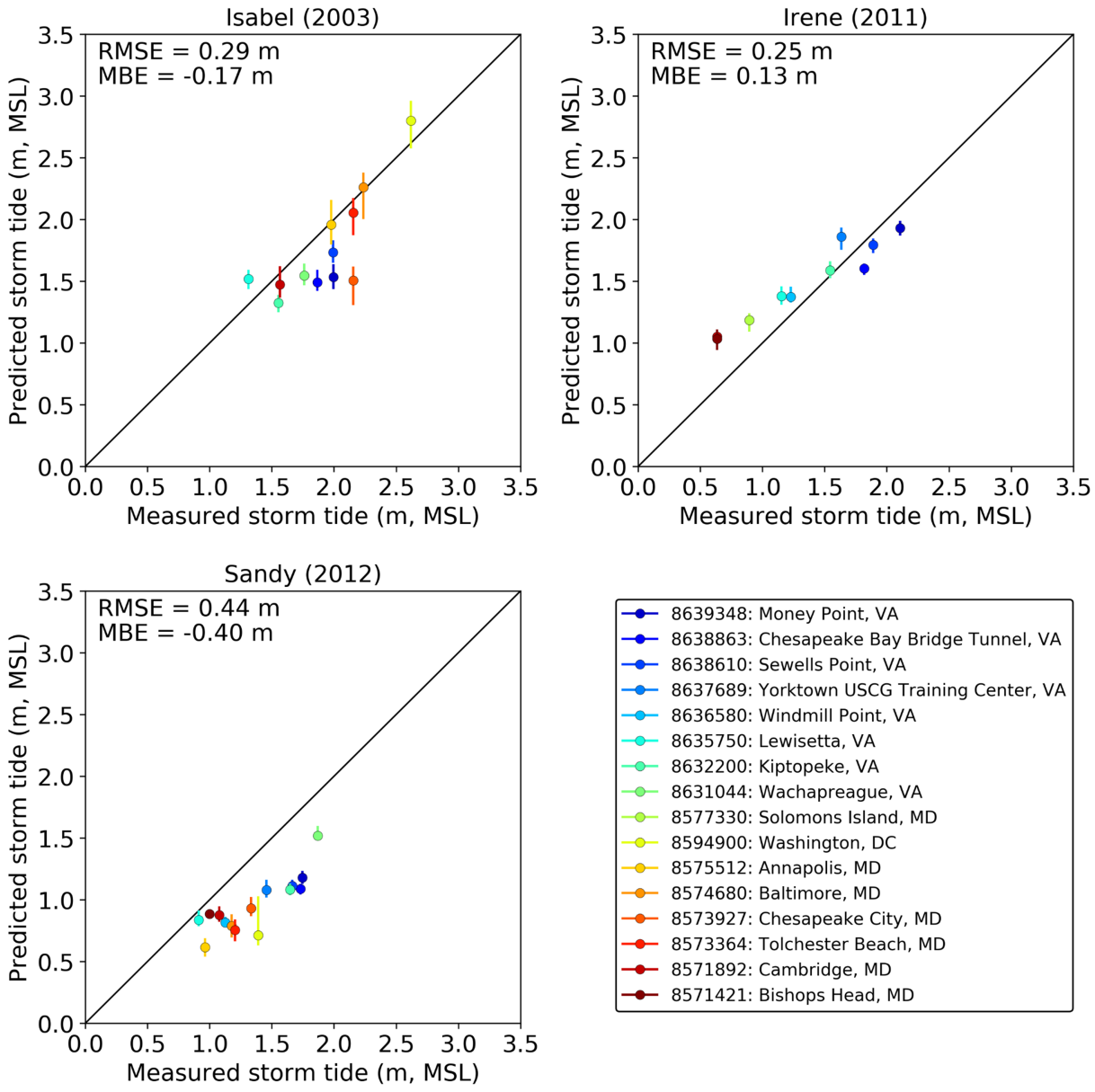

Figure 4.10: Comparison between measured storm tide (x-axis) and C1PKNet storm tide predictions (y-axis). In the y-axis, the circle and vertical line represent the mean and the range of 10 C1PKNet predictions, respectively.

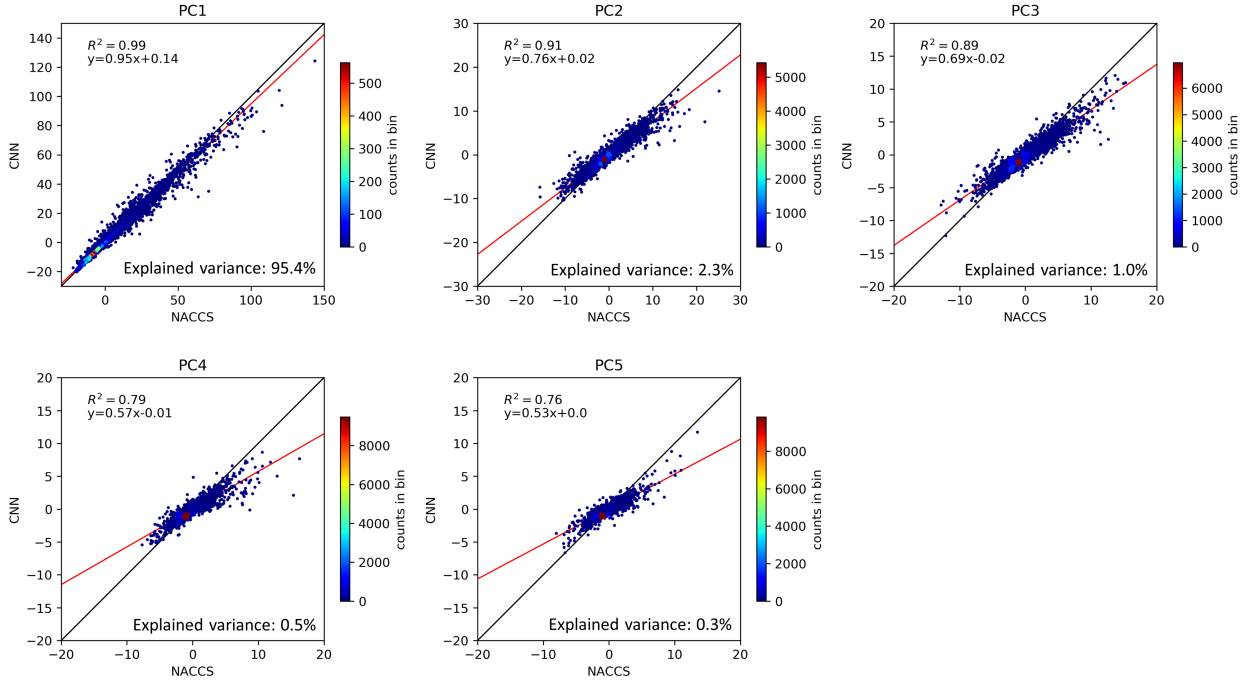

Figure 4.11: Performance of convolutional neural network. Principal components derived from the scaled peak storm surges of NACCS (x-axis) versus principal components predicted by the convolutional neural networks (y-axis). Each plot contains 12,372 data (1,031 storms $\times$ 12 clusters). The black line represents the equal line, and the red line is the linear regression solution.

4.5 Discussion

4.5.1 Error contribution analysis

In section 4.4.1, the performance of the C1PKNet model was investigated based on the final outputs of the C1PKNet model (peak storm surge predictions) containing errors from three components: the convolutional neural network (CNN), principal component analysis (PCA), and k-means clustering. To explore the impact of each component separately, we performed additional three analyses as follows.

First, to investigate the errors coming from CNN, we compared the principal components

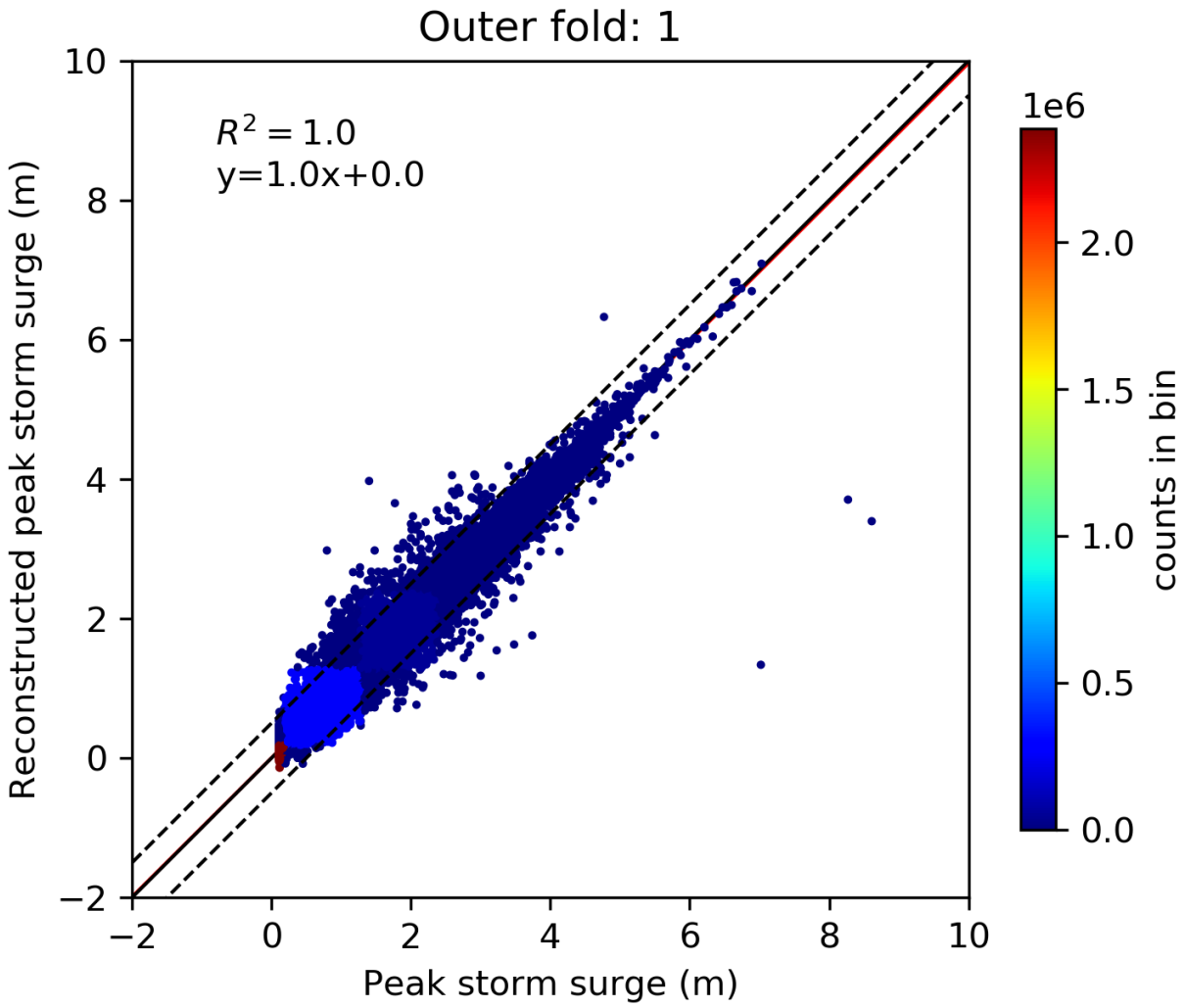

Figure 4.12: Performance of principal component analysis. Comparison between the peak storm surges of NACCS (x-axis) and the peak storm surges reconstructed using five principal components (y-axis) for the first outer fold. The plot contains $2,883,897$ data (927 storms $\times$ $3,111$ points). The black line represents the equal line, the black dashed lines indicate ± 0.5 m about an exact match, and the red line is linear regression solution.

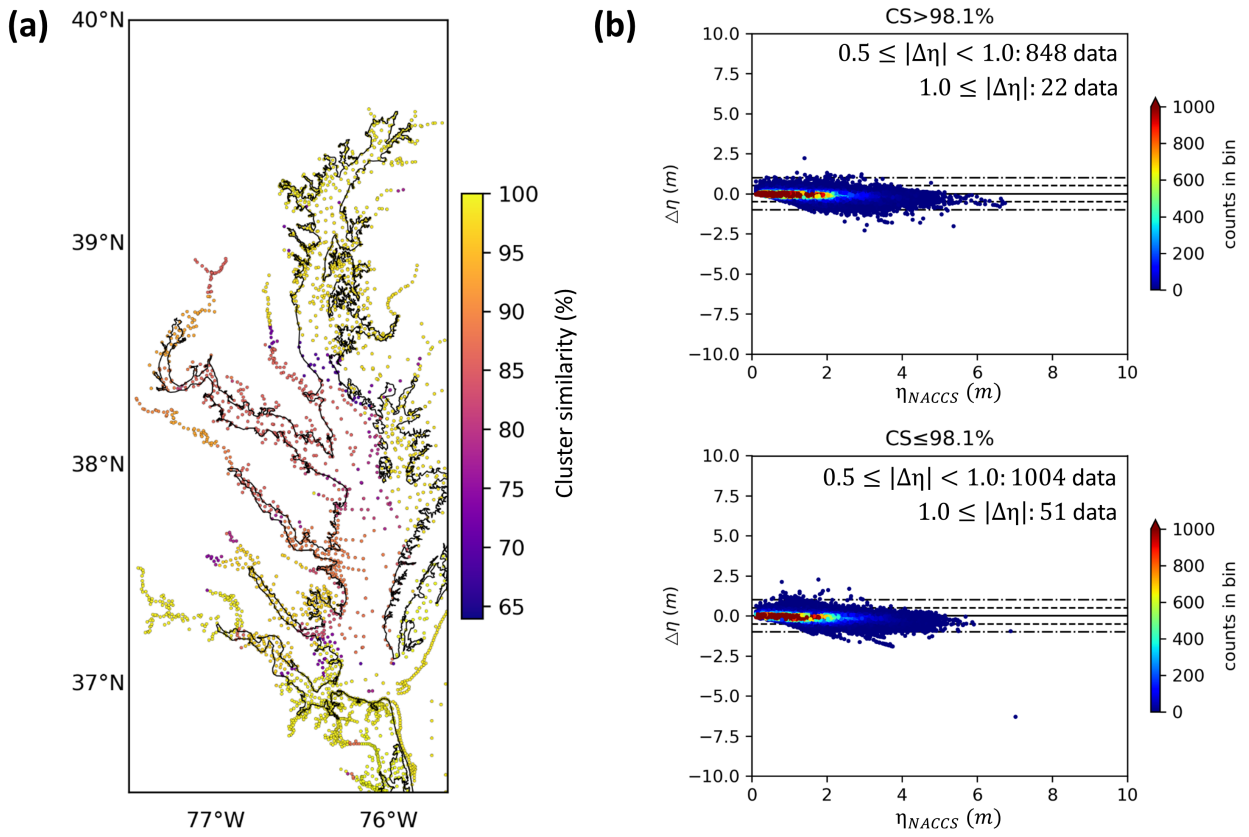

Figure 4.13: Performance of k-means clustering. (a) Map of cluster similarity that represents how often the point is classified into the same cluster. The larger the cluster similarity value, the more often the point is classified into the same cluster. (b) Peak storm surge error distribution depending on a cluster similarity value. The black line, black dashed lines, and black dashed-dot lines represent the point where the absolute error is 0.0 m, 0.5 m, and 1.0 m, respectively.

derived from the scaled peak storm surges of NACCS and the principal components predicted by the CNNs across 10 folds (Figure 4.11). Overall, the CNNs well predicted the first principal component (PC1) that explains 95.4% of the variance of peak storm surges ($R^2 = 0.99$). However, the accuracy of the CNNs gradually decreased from the second principal component ($R^2 = 0.91$) to the fifth principal component ($R^2 = 0.76$).

Secondly, to investigate the errors coming from PCA, we compared the original peak storm surges of NACCS and the peak storm surges reconstructed using five principal components for each outer-fold (Figure 4.12). Overall, the reconstructed peak storm surges match well with the original peak storm surges ($R^2 = 1.0$). The difference between the original peak storm surges and the reconstructed peak storm surges was greater than 0.5 m on 0.03% of data. Note that the three largest differences in data with a greater than 6 m of peak storm surge occurred at point 13256 (Figure C.3) and point 15125 (Figure C.4). We believe these outliers are caused by unstable numerical simulations, as mentioned in section 4.4.1, because these peak storm surges were distinctively larger compared to that of the other similar TCs at the same point. The figures of the entire comparisons for 10 outer-folds can be found in Figure C.5.

And lastly, to investigate the errors coming from k-means clustering, we first examined how similar the k-means clustering results were during 10-fold cross-validation. To quantify the cluster similarity at a point-level, we calculated how often a pair of points were classified into the same cluster for all folds. And then, we counted the number of points where the frequency was zero (never grouped into the same cluster) and ten (always grouped into the same cluster) for each point. Based on the counted number (N), we defined the cluster similarity (CS), which indirectly represents how often the point was classified into the same cluster, as follows:

$$CS = \frac{N}{N_T - 1} \times 100(\%) \tag{4.5}$$

where N_T is the total number of points considered in the study (3111 points). As shown in Figure 4.13a, most of the points were classified into the same cluster during 10-fold cross-validation (median $CS = 98.1\%$). The relatively small CS values ($CS < 80\%$) were shown in 141 points (about 4.5%) that are mainly distributed at the middle of the bay ($37°N - 38.5°N$). To compare the accuracy of the C1PKNet model depending on the CS values, we plotted the error distribution after dividing the save-points into two groups based on $CS = 98.1\%$ (Figure 4.13b). The results show that the small CS group ($CS \leq 98.1\%$) contains more data with large errors. In particular, the data where the error is larger than 1 m was shown more than twice in the small CS group ($CS \leq 98.1\%$) compared to the large CS group ($CS > 98.1\%$).

4.5.2 Limitations and future work

There are still several limitations that need to be addressed in the future. First, the US Northeast is affected by extratropical (e.g., nor'easters) and tropical cyclones [8], but the C1PKNet model is only applicable to tropical cyclones. Even though tropical cyclones have traditionally been more intense than extratropical cyclones, since nor'easters are known to affect the Chesapeake Bay more frequently, last longer, and impact larger areas than tropical cyclones [34, 41], future studies should expand its applicability to extratropical cyclones in surrogate modeling.

Secondly, historical hurricanes such as Ike (2008) have shown that dangerous forerunner surge preceding a peak storm surge can occur [64, 84], but the C1PKNet model is only able to predict peak storm surges. Although a large forerunner surge is rare, since it could cause

much damage once occurred, the C1PKnet model should be expanded to predict storm surge time-series to capture the forerunner surge.

Thirdly, several factors that can exacerbate flooding when combined with storm surge (the astronomical tide, sea-level change combined with land subsidence, and heavy rainfall) were not considered in this study. Several studies have shown that the water level can be higher or lower than the individual contribution due to nonlinear tidal surge interactions [e.g., 138]. Rising sea levels due to climate change, which can trigger increases in flood frequency by storm surge, are a great concern to coastal communities [150]. Especially, the Hampton Roads area in the lower Chesapeake Bay has been identified as experiencing a high rate of relative sea-level rise [13, 30, 120]. If storm surges and heavy rains occur simultaneously (or in close succession), the possibility of flooding is much greater than from storm surge alone [9, 147]. Thus, future studies are necessary to take into account the astronomical tide, sea-level change, and heavy rainfall in surrogate modeling.

And lastly, there are several parameters of the C1PKNet model needed to be optimized. For example, we used the longest time-series of TC parameters (40 hours) that can be extracted from the NACCS database as inputs of the C1PKNet model. Since the CNN training time is related to the input size, the time-series length should be optimized considering both model accuracy and efficiency. Also, various CNN architectures (Figure 4.4), the number of principal components, and the number of clusters should be tested to optimize the performance of the C1PKNet model. However, since these hyperparameter/parameter tuning will be computationally expensive with a grid search approach (considering all possible combinations), an efficient optimization algorithm will be needed. Moreover, Taflanidis et al. [134]'s approach, which is used to fill the missing peak storm surge values in this study, is sensitive to the peak storm surge of the nearest point. Thus, future studies should investigate several interpolation approaches (e.g., k-nearest neighbor interpolation with an inverse

distance weighting [72]) that can improve the performance of the C1PKNet model.

4.6 Conclusions

This study presents a new surrogate model called the C1PKNet model that can rapidly predict peak storm surges across the extensive coastal region from time-series of tropical cyclone (TC) conditions. A convolutional neural network (CNN) was implemented in surrogate modeling to incorporate the variation of tropical cyclone conditions over time. The principal component analysis and k-means clustering were integrated to facilitate high efficiency and accuracy of CNN. The C1PKNet model was trained for the Chesapeake Bay using 1031 synthetic tropical cyclones of the NACCS database, including landfalling-track storms and bypassing-track storms. The performance of the C1PKNet model was evaluated based on not only 1031 synthetic tropical cyclones of the NACCS database but also three historical hurricane observations (Hurricane Isabel in 2003, Hurricane Irene in 2011, and Hurricane Sandy in 2012). To provide complete performance information, we analyzed the error of individual point-data (Figure 4.6a), the aggregate error metric after grouping the data by peak storm surge values (Figure 4.6b), the wet/dry misclassification (Figure 4.7), and the errors coming from each component of the C1PKNet model (Figures 4.11-4.13). The results indicate that the C1PKNet model is computationally efficient and can predict peak storm surges for any tropical cyclone condition that changes over time. We believe that the C1PKNet model has the potential for enhancing coastal resilience by providing rapid storm surge predictions. From this study, the following recommendations can be drawn for surrogate modeling to predict peak storm surges:

1. The variation of tropical cyclone conditions over time should be incorporated into surrogate modeling because peak storm surge is not always most correlated with TC parameters

at landfall.

2. The bypassing-track storms should not be neglected in surrogate modeling, which could cause coastal flooding.

3. The performance assessment should include the case studies based on historical hurricanes because the performance quantification only relying on cross-validation can mislead the actual performance of surrogate model.

Acknowledgments

This publication was prepared by Jun-Whan Lee using Federal funds under award NA18OAR4170083, Virginia Sea Grant College Program Project R/72155L from the National Oceanic and Atmospheric Administration's (NOAA) National Sea Grant College Program, U.S. Department. of Commerce. The statements, findings, conclusions, and recommendations are those of the author(s) and do not necessarily reflect the views of Virginia Sea Grant, NOAA, or the U.S. Department of Commerce. This material is based upon work partially supported by the National Science Foundation under Grant Nos. 1630099 and 1735139. Any opinions, findings, and conclusions or recommendations expressed in this material are those of the authors and do not necessarily reflect the views of the National Science Foundation. The authors acknowledge Advanced Research Computing at Virginia Tech for providing computational resources and technical support that have contributed to the results reported within this paper. URL: https://198.82.212.30. The North Atlantic Comprehensive Coastal Study (NACCS) database of the US Army Corps of Engineers was obtained from the Coastal Hazards System (CHS) (https://chs.erdc.dren.mil).

Chapter 5

Conclusions

5.1 Summary

This dissertation has presented new surrogate models using statistical and machine learning techniques to rapidly predict coastal hazards such as a tsunami and storm surge. The research focused on (1) reducing the input dimensionality in tsunami surrogate modeling, (2) inferring a tsunami source and its impact from tsunami run-up records, and (3) incorporating the variation of tropical cyclone conditions in storm surge surrogate modeling.

In Chapter 2, a tsunami run-up response function (TRRF) model was developed that can rapidly predict the spatial distribution of the run-up from near-field tsunamis over real topography without substantial loss of accuracy, with respect to high-fidelity physics-based models. The TRRF model is based on a response surface methodology (RSM), which is one of the surrogate modeling approaches. The TRRF model was demonstrated in northern Puerto Rico, where a significant tsunami generated by an earthquake along the Puerto Rico Trench could devastate the coastal communities on the northern shore. The input dimensionality was reduced based on the idea that the tsunami run-up distribution can be decomposed into a leading-order contribution being modeled by fault parameters using the Okal and Synolakis [105]'s empirical formula and a regional component that is dictated by the local topography.

In Chapter 3, a tsunami run-up response function-based inversion (TRRF-INV) model was

developed to provide probabilistic estimates of a near-field tsunami source and a tsunami run-up distribution from a small number of run-up records. The TRRF-INV model can infer a tsunami source from tsunami run-up records by adopting the TRRF model [77] for tsunami forward modeling. The TRRF-INV model was tested based on 1,600 synthetic scenarios in northern Chile and was applied to the 2014 Iquique, Chile, tsunami event (Mw 8.1) as a case study. The results show that the TRRF-INV model can provide reasonable estimates of tsunami source to first order and accurate tsunami run-up distribution only with 20 run-up values with less than half a meter of uncertainty in the study area.

In Chapter 4, a new one-dimensional convolutional neural network combined with principal component analysis and k-means clustering (C1PKNet) model was developed that can rapidly predict peak storm surges across an extensive coastal region from tropical cyclone track time-series. The variation of tropical cyclone conditions over time was incorporated in surrogate modeling using a convolutional neural network. The C1PKNet model was trained and cross-validated for the Chesapeake Bay area of the United States using the 1031 synthetic tropical cyclones, including both landfalling and bypassing storms. The C1PKNet model was applied to three historical hurricanes (Hurricane Isabel in 2003, Hurricane Irene in 2011, and Hurricane Sandy in 2012) as case studies. The results show that the C1PKNet model can rapidly provide peak storm surges for any tropical cyclone condition without substantial loss of accuracy.

Moreover, to produce valuable transferable knowledge from research results to coastal stakeholders and coastal communities, under the guidance of Mr. Doug Marcy, a Coastal Hazards specialist at NOAA's Office for Coastal Management, an interactive web-mapping tool was developed by integrating the research results of chapter 4. We believe this tool has the potential to raise the communities' awareness of storm surge hazards and to support decision and policy makers.

5.2 Contributions

The major contributions of this dissertation are summarized as follows.

- In tsunami modeling, a surrogate model has not been widely developed due to the high-dimensional input, which requires a large number of simulations to build a surrogate model. Chapter 2 is the first study that has successfully reduced the input dimensionality in tsunami surrogate modeling by decomposing the leading order tsunami run-up contribution and the residual part of the run-up distribution using the Okal and Synolakis [105]'s empirical formula.

- In tsunami inversion modeling, a tsunami run-up record has not been widely used to infer a tsunami source and its impact because of the computational burden of high-fidelity tsunami forward simulations to find a tsunami source that best matches the tsunami run-up record. Chapter 3 is the first study that has successfully overcome the computational burden of tsunami forward simulations in tsunami inversion modeling by adopting the surrogate model developed in Chapter 2.

- In storm surge modeling, most of the existing surrogate modeling approaches relied on a tropical cyclone condition at one moment (usually at or near landfall), which is not always most correlated with the peak storm surge. Chapter 4 is the first study that successfully incorporates the variation of tropical cyclone conditions over time in surrogate modeling by using a convolutional neural network. Thanks to this incorporation, the developed surrogate model is also able to consider bypassing storms, which were neglected in several surrogate modeling studies.

5.3 Significance for disaster resilience

The broader impacts of this dissertation in the context of interdisciplinary disaster resilience are summarized as follows.

- This work has the potential to save lives and mitigate coastal hazard damage by improving the capacity of the real-time probabilistic forecast and the robust probabilistic hazard assessment-based evacuation planning. This will benefit not only the governors and state leaders to successfully manage a coastal hazard and a corresponding evacuation but also the urban planners to design effective evacuation plans considering the risks to infrastructure, businesses, and vulnerable populations. This work can also be linked to the study of adequate shelter space selection, traffic & supply chain dynamics during evacuation, risk-based decision making, and the economic impact of evacuations on coastal infrastructures.

- This work has the potential to promote resilient coastal communities by better understanding coastal hazards. This will benefit engineers to effectively design coastal infrastructures and help policy makers choose more successful strategies for coastal hazards. This work can also be linked to the study of the impacts of coastal infrastructure on natural systems, integrated coastal zone management planning, land use standards, and building codes for hazard mitigation.

5.4 Future work

The detailed limitations and future works have been noted and can be found throughout the dissertation. Here, four major recommendations for future research are highlighted as follows.

- Currently, the tsunami run-up response function (TRRF) model and the tsunami run-up response function-based inversion (TRRF-INV) model are only applicable to uniform slip distribution. This prevents the TRRF model and the TRRF-INV model from being applied to large earthquakes with complex slip distribution. Moreover, several studies have shown that a tsunami run-up distribution can vary depending on the heterogeneity of slip distribution even when the earthquake magnitude is the same [e.g., 79]. Therefore, future studies should expand the TRRF model and the TRRF-INV model applicable to non-uniform slip distribution.

- Further surrogate model improvement is needed to consider the following factors, which can exacerbate coastal flooding when combined with coastal hazards (tsunami and storm surge). First, a sea-level rise due to climate change should be considered that can not only trigger increases in flood frequency by storm surge [150] but also dramatically impact the coastal flooding by tsunami [80]. Secondly, an astronomical tide should be considered that can cause the water level to be higher or lower than the individual contribution due to nonlinear interactions between the tide and the coastal hazard [138, 142, 155]. And lastly, heavy rainfall, which occurs simultaneously or in close succession with storm surge, should be considered because it can cause a much greater increase in the possibility of flooding than from storm surge alone [9, 147].

- The performance of the TRRF model and the C1PKNet model for probabilistic forecasting and probabilistic hazard assessment should be evaluated. Future studies should

analyze the uncertainty of forecasting according to the number of surrogate model simulations. Future research should also analyze how an annual experience probability or a return period of tsunami and storm surge hazards change with the number of surrogate model simulations.

- And last but not least, there is a widespread perception that the impact of coastal risk is unevenly distributed in coastal communities depending on resources to prepare for, respond to, and recover from coastal hazards [24]. Future studies should leverage the surrogate models to assess the risk (a combination of hazard, exposure, and vulnerability) to understand not only the dynamic interaction between risk drivers and mitigation measures but also the socioeconomic impacts of coastal hazards. Since the risk is inherently multi-dimensional, the risk assessment framework will require transdisciplinary collaboration among researchers in the social, policy, and economic sectors to incorporate the human element into the framework.

Bibliography

[1] Keiiti Aki. Generation and Propagation of G Waves from the Niigata Earthquake of June 16, 1964.: Part 2. Estimation of earthquake moment, released energy, and stress-strain drop from the G wave spectrum. *Bulletin of the Earthquake Research Institute, University of Tokyo*, 44(1):73–88, 1966.

[2] Azin Al Kajbaf and Michelle Bensi. Application of surrogate models in estimation of storm surge:a comparative assessment. *Applied Soft Computing*, 91:106184, 2020. ISSN 1568-4946. doi: 10.1016/j.asoc.2020.106184.

[3] Christopher Amante and Barry W. Eakins. Data from "ETOPO1 1 arc-minute global relief model" National Geophysical Data Center, NOAA. Available at https://dx.doi.org/10.7289/V5C8276M. Deposited 1 January 2009., 2009.

[4] Chao An, Ignacio Sepúlveda, and Philip L.-F. Liu. Tsunami source and its validation of the 2014 Iquique, Chile, earthquake. *Geophysical Research Letters*, 41(11):3988–3994, 2014. doi: 10.1002/2014GL060567.

[5] Tadashi Annaka, Kenji Satake, Tsutomu Sakakiyama, Ken Yanagisawa, and Nobuo Shuto. Logic-tree Approach for Probabilistic Tsunami Hazard Analysis and its Applications to the Japanese Coasts. *Pure & Applied Geophysics*, 164:577–592, 2007. doi: 10.1007/s00024-006-0174-3.

[6] Shin Aoi, Wataru Suzuki, Naotaka Yamamoto Chikasada, Takayuki Miyoshi, Taro Arikawa, , and Katsumi Seki. Development and utilization of real-time tsunami inundation forecast system using s-net data. *Journal of Disaster Research*, 14(2):212–224, 2019. doi: 10.20965/jdr.2019.p0212.

[7] Nicolas P Arcos, Paula K Dunbar, Kelly J Stroker, and Laura SL Kong. The impact of post-tsunami surveys on the NCEI/WDS global historical tsunami database. *Pure and Applied Geophysics*, 176(7):2809–2829, 2019.

[8] R. Bakhtyar, P.M. Orton, R. Marsooli, and J.K. Miller. Rapid wave modeling of severe historical extratropical cyclones off the northeastern united states. *Ocean Engineering*, 159:315–332, 2018. ISSN 0029-8018. doi: 10.1016/j.oceaneng.2018.04.037.

[9] Benjamin Bass and Philip Bedient. Surrogate modeling of joint flood risk across coastal watersheds. *Journal of Hydrology*, 558:159–173, 2018. ISSN 0022-1694. doi: 10.1016/j.jhydrol.2018.01.014.

[10] Eric S Blake, Chris Landsea, and Ethan J Gibney. The deadliest, costliest, and most intense united states tropical cyclones from 1851 to 2010 (and other frequently requested hurricane facts). Technical Report NOAA Technical Memorandum NWS NHC-6, National Weather Service, National Hurricane Center, Miami, Florida, 2011. URL https://www.nhc.noaa.gov/pdf/nws-nhc-6.pdf.

[11] Lilian Blaser, Frank Krüger, Matthias Ohrnberger, and Frank Scherbaum. Scaling relations of earthquake source parameter estimates with special focus on subduction environment. *Bulletin of the Seismological Society of America*, 100(6):2914–2926, 2010. ISSN 00371106. doi: 10.1785/0120100111.

[12] G. E. P. Box and K. B. Wilson. On the Experimental Attainment of Optimum Conditions. *Journal of the Royal Statistical Society: Series B (Methodological)*, 13(1):1–45, 1951.

[13] Brett Buzzanga, David P. S. Bekaert, Ben D. Hamlington, and Simran S. Sangha. Toward sustained monitoring of subsidence at the coast using insar and gps: An applica-

tion in hampton roads, virginia. *Geophysical Research Letters*, 47(18):e2020GL090013, 2020. doi: 10.1029/2020GL090013.

[14] Patricio A Catalán, Rafael Aránguiz, Gabriel González, Takashi Tomita, Rodrigo Cienfuegos, Juan González, Mahesh N Shrivastava, Kentaro Kumagai, Cyril Mokrani, Pablo Cortés, et al. The 1 April 2014 Pisagua tsunami: observations and modeling. *Geophysical Research Letters*, 42(8):2918–2925, 2015.

[15] Patricio A. Catalan, Alejandra Gubler, Javier Cañas, Carlos Zuñiga, Cecilia Zelaya, Leonardo Pizarro, Carlos Valdes, Rene Mena, Eduardo Toledo, and Rodrigo Cienfuegos. Design and operational implementation of the integrated tsunami forecast and warning system in chile (sipat). *Coastal Engineering Journal*, 62(3):373–388, 2020. doi: 10.1080/21664250.2020.1727402.

[16] Simone Cesca, F Grigoli, Sebastian Heimann, T Dahm, Marius Kriegerowski, M Sobiesiak, C Tassara, and M Olcay. The Mw 8.1 2014 Iquique, Chile, seismic sequence: a tale of foreshocks and aftershocks. *Geophysical Journal International*, 204(3):1766–1780, 2016.

[17] Kejie Chen, Andrey Babeyko, Andreas Hoechner, and Maorong Ge. Comparing source inversion techniques for GPS-based local tsunami forecasting: A case study for the April 2014 M8.1 Iquique, Chile, earthquake. *Geophysical Research Letters*, 43(7): 3186–3192, 2016. doi: https://doi.org/10.1002/2016GL068042.

[18] Mohamed Chlieh, Hugo Perfettini, Hernando Tavera, Jean-Philippe Avouac, Dominique Remy, Jean-Mathieu Nocquet, Frédérique Rolandone, Francis Bondoux, Germinal Gabalda, and Sylvain Bonvalot. Interseismic coupling and seismic potential along the Central Andes subduction zone. *Journal of Geophysical Research: Solid Earth*, 116(B12), 2011. doi: 10.1029/2010JB008166.

[19] François Chollet et al. Keras. https://keras.io, 2015.

[20] Mary A Cialone, T Chris Massey, Mary E Anderson, Alison S Grzegorzewski, Robert E Jensen, Alan Cialone, David J Mark, Kimberly C Pevey, Brittany L Gunkel, and Tate O McAlpin. North atlantic coast comprehensive study (naccs) coastal storm model simulations: Waves and water levels. Technical Report ERCD/CHL TR-15-14, U.S. Army Engineer Research and Development Center, Coastal and Hydraulics Laboratory, Vicksburg, MS, 2015. URL https://hdl.handle.net/11681/7339.

[21] Mary A. Cialone, Alison S. Grzegorzewski, David J. Mark, Mary A. Bryant, and Thomas C. Massey. Coastal-storm model development and water-level validation for the north atlantic coast comprehensive study. *Journal of Waterway, Port, Coastal, and Ocean Engineering*, 143(5):04017031, 2017. doi: 10.1061/(ASCE)WW.1943-5460.0000408.

[22] Rodrigo Cienfuegos, Patricio A. Catalán, Alejandro Urrutia, Roberto Benavente, Rafael Aránguiz, and Gabriel González. What can we do to forecast tsunami hazards in the near field given large epistemic uncertainty in rapid seismic source inversions? *Geophysical Research Letters*, 45(10):4944–4955, 2018. doi: 10.1029/2018GL076998.

[23] Diana Comte and Gerardo Suárez. Stress distribution and geometry of the subducting Nazca plate in northern Chile using teleseismically recorded earthquakes. *Geophysical Journal International*, 122(2):419–440, 1995.

[24] Susan L. Cutter, Bryan J. Boruff, and W. Lynn Shirley. Social vulnerability to environmental hazards. *Social Science Quarterly*, 84(2):242–261, 2003. doi: 10.1111/1540-6237.8402002.

[25] Gareth Davies. Tsunami variability from uncalibrated stochastic earthquake models:

tests against deep ocean observations 2006–2016. *Geophysical Journal International*, 218(3):1939–1960, 2019. doi: 10.1093/gji/ggz260.

[26] Gareth Davies, Jonathan Griffin, Finn Løvholt, Sylfest Glimsdal, Carl Harbitz, Hong Kie Thio, Stefano Lorito, Roberto Basili, Jacopo Selva, Eric Geist, et al. A global probabilistic tsunami hazard assessment from earthquake sources. *Geological Society, London, Special Publications*, 456(1):219–244, 2018. doi: 10.1144/SP456.5.

[27] Julie L Demuth, Mark DeMaria, and John A Knaff. Improvement of advanced microwave sounding unit tropical cyclone intensity and size estimation algorithms. *Journal of applied meteorology and climatology*, 45(11):1573–1581, 2006.

[28] Göran Ekström, Meredith Nettles, and AM Dziewoński. The global CMT project 2004–2010: Centroid-moment tensors for 13,017 earthquakes. *Physics of the Earth and Planetary Interiors*, 200:1–9, 2012.

[29] Mireille Escudero Castillo, Edgar Mendoza Baldwin, Rodolfo Silva Casarin, Gregorio Posada Vanegas, and Maritza Arganis Juaréz. Characterization of risks in coastal zones: A review. *CLEAN – Soil, Air, Water*, 40(9):894–905, 2012. doi: 10.1002/clen.201100679.

[30] Tal Ezer and Larry P. Atkinson. Accelerated flooding along the u.s. east coast: On the impact of sea-level rise, tides, storms, the gulf stream, and the north atlantic oscillations. *Earth's Future*, 2(8):362–382, 2014. doi: 10.1002/2014EF000252.

[31] Colleen Fanelli and Paul Fanelli. Hurricane irene, 2011. URL https://repository.library.noaa.gov/view/noaa/17128. Technical Report.

[32] Colleen Fanelli, Paul Fanelli, and David Wolcott. Hurricane sandy, 2013. URL https://repository.library.noaa.gov/view/noaa/17125. Technical Report.

[33] Mauricio Fuentes, Sebastián Riquelme, Gavin Hayes, Miguel Medina, Diego Melgar, Gabriel Vargas, José González, and Angelo Villalobos. A Study of the 2015 Mw 8.3 Illapel earthquake and tsunami: Numerical and analytical approaches. *Pure and Applied Geophysics*, 173(6):1847–1858, 2016.

[34] Juan L. Garzon, Celso M. Ferreira, and Roberto Padilla-Hernandez. Evaluation of weather forecast systems for storm surge modeling in the chesapeake bay. *Ocean Dynamics*, 68(1):91–107, Jan 2018. ISSN 1616-7228. doi: 10.1007/s10236-017-1120-x.

[35] GEBCO Compilation Group. Gebco 2019 grid, 2019.

[36] Eric L. Geist. Complex earthquake rupture and local tsunamis. *Journal of Geophysical Research: Solid Earth*, 107(B5):ESE 2–1–ESE 2–15, 2002. doi: 10.1029/2000JB000139.

[37] Eric L. Geist and Tom Parsons. Probabilistic analysis of tsunami hazards*. *Natural Hazards*, 37(3):277–314, Mar 2006. ISSN 1573-0840. doi: 10.1007/s11069-005-4646-z.

[38] Edison Gica, Mick C. Spillane, Vasily V. Titov, Christopher D. Chamberlin, and Jean C. Newman. Development of the forecast propagation database for NOAA's Short-term Inundation Forecast for Tsunamis (SIFT). *NOAA Technical Memorandum OAR PMEL*, 139, 2008.

[39] Bob Glahn, Arthur Taylor, Nicole Kurkowski, and Wilson A Shaffer. The role of the slosh model in national weather service storm surge forecasting. *National Weather Digest*, 33(1):3–14, 2009.

[40] Sylfest Glimsdal, Finn Løvholt, Carl Bonnevie Harbitz, Fabrizio Romano, Stefano Lorito, Simone Orefice, Beatriz Brizuela, Jacopo Selva, A Hoechner, Manuela Volpe, et al. A new approximate method for quantifying tsunami maximum inundation height

probability. *Pure and Applied Geophysics*, 176(7):3227–3246, 2019. doi: 10.1007/s00024-019-02091-w.

[41] Wenping Gong, Jian Shen, Kyoung-Ho Cho, and Harry V. Wang. A numerical model study of barotropic subtidal water exchange between estuary and subestuaries (tributaries) in the chesapeake bay during northeaster events. *Ocean Modelling*, 26(3): 170–189, 2009. ISSN 1463-5003. doi: 10.1016/j.ocemod.2008.09.005.

[42] Juan González, Gabriel González, Rafael Aránguiz, Diego Melgar, Natalia Zamora, Mahesh N Shrivastava, Ranjit Das, Patricio A Catalán, and Rodrigo Cienfuegos. A hybrid deterministic and stochastic approach for tsunami hazard assessment in Iquique, Chile. *Natural Hazards*, 100(1):231–254, 2020.

[43] S. T. Grilli, S. Dubosq, N. Pophet, Y. Pérignon, J. T. Kirby, and F. Shi. Numerical simulation and first-order hazard analysis of large co-seismic tsunamis generated in the Puerto Rico trench: Near-field impact on the North shore of Puerto Rico and far-field impact on the US East Coast. *Natural Hazards and Earth System Science*, 10(10): 2109–2125, 2010. ISSN 15618633. doi: 10.5194/nhess-10-2109-2010.

[44] Aditya Riadi Gusman, Satoko Murotani, Kenji Satake, Mohammad Heidarzadeh, Endra Gunawan, Shingo Watada, and Bernd Schurr. Fault slip distribution of the 2014 Iquique, Chile, earthquake estimated from ocean-wide tsunami waveforms and GPS data. *Geophysical Research Letters*, 42(4):1053–1060, 2015. doi: 10.1002/2014GL062604.

[45] Zhong-Hua Han, Ke-Shi Zhang, et al. Surrogate-based optimization. *Real-world applications of genetic algorithms*, 343, 2012.

[46] Thomas C Hanks and Hiroo Kanamori. A moment magnitude scale. *Journal*

of Geophysical Research: Solid Earth, 84(B5):2348–2350, 1979. doi: 10.1029/JB084iB05p02348.

[47] Carl B Harbitz, Finn Løvholt, and Hilmar Bungum. Submarine landslide tsunamis: how extreme and how likely? *Natural Hazards*, 72(3):1341–1374, 2014. doi: 10.1007/s11069-013-0681-3.

[48] M. Reza Hashemi, Malcolm L. Spaulding, Alex Shaw, Hamed Farhadi, and Matt Lewis. An efficient artificial intelligence model for prediction of tropical storm surge. *Natural Hazards*, 82(1):471–491, 2016. doi: 10.1007/s11069-016-2193-4.

[49] Gavin P. Hayes, David J. Wald, and Rebecca L. Johnson. Slab1.0: A three-dimensional model of global subduction zone geometries. *Journal of Geophysical Research: Solid Earth*, 117(B1), 2012. doi: 10.1029/2011JB008524.

[50] Gavin P Hayes, Matthew W Herman, William D Barnhart, Kevin P Furlong, Sebástian Riquelme, Harley M Benz, Eric Bergman, Sergio Barrientos, Paul S Earle, and Sergey Samsonov. Continuing megathrust earthquake potential in Chile after the 2014 Iquique earthquake. *Nature*, 512(7514):295–298, 2014.

[51] Gavin P. Hayes, Ginevra L. Moore, Daniel E. Portner, Mike Hearne, Hanna Flamme, Maria Furtney, and Gregory M. Smoczyk. Slab2, a comprehensive subduction zone geometry model. *Science*, 362(6410):58–61, 2018. doi: 10.1126/science.aat4723.

[52] Mohammad Heidarzadeh, Tomoya Harada, Kenji Satake, Takeo Ishibe, and Tomohiro Takagawa. Tsunamis from strike-slip earthquakes in the Wharton Basin, northeast Indian Ocean: March 2016 Mw 7.8 event and its relationship with the April 2012 Mw 8.6 event. *Geophysical Journal International*, 211(3):1601–1612, 2017. doi: 10.1093/gji/ggx395.

[53] Tung-Cheng Ho, Kenji Satake, Shingo Watada, and Yushiro Fujii. Source estimate for the 1960 Chile earthquake from joint inversion of geodetic and transoceanic tsunami data. *Journal of Geophysical Research: Solid Earth*, 124(3):2812–2828, 2019.

[54] M. Hoshiba and T. Ozaki. *Earthquake early warning and tsunami warning of the Japan Meteorological Agency, and their performance in the 2011 off the pacific coast of Tohoku Earthquake (Mw9.0)*, pages 1–28. Springer Berlin Heidelberg, Berlin, Heidelberg, 2014.

[55] Gerald Hovis, William Popovich, 1957 Zervas, Chris Eugene, James R. Hubbard, H. H. Shih, and Peter J. Stone. Effects of hurricane isabel on water levels : data report, 2004. URL https://repository.library.noaa.gov/view/noaa/14665. Technical Report.

[56] Sergey Ioffe and Christian Szegedy. Batch normalization: Accelerating deep network training by reducing internal covariate shift. In *International conference on machine learning*, pages 448–456. PMLR, 2015.

[57] Kei Ioki and Yuichiro Tanioka. Re-estimated fault model of the 17th century great earthquake off Hokkaido using tsunami deposit data. *Earth and Planetary Science Letters*, 433:133 – 138, 2016. ISSN 0012-821X. doi: https://doi.org/10.1016/j.epsl.2015.10.009.

[58] IPET. Performance evaluation of the new orleans and southeast louisiana hurricane protection system: Final report of the interagency performance evaluation task force. Technical report, 2006.

[59] Jennifer L. Irish, Donald T. Resio, and Mary A. Cialone. A surge response function approach to coastal hazard assessment. part 2: Quantification of spatial attributes of response functions. *Natural Hazards*, 51(1):183–205, Oct 2009. ISSN 1573-0840. doi: 10.1007/s11069-009-9381-4.

[60] Chester P Jelesnianski. *SLOSH: Sea, lake, and overland surges from hurricanes*, volume 48. US Department of Commerce, National Oceanic and Atmospheric Administration …, 1992.

[61] Gaofeng Jia and Alexandros A. Taflanidis. Kriging metamodeling for approximation of high-dimensional wave and surge responses in real-time storm/hurricane risk assessment. *Computer Methods in Applied Mechanics and Engineering*, 261-262:24–38, 2013. ISSN 0045-7825. doi: 10.1016/j.cma.2013.03.012.

[62] Gaofeng Jia, Alexandros A. Taflanidis, Norberto C. Nadal-Caraballo, Jeffrey A. Melby, Andrew B. Kennedy, and Jane M. Smith. Surrogate modeling for peak or time-dependent storm surge prediction over an extended coastal region using an existing database of synthetic storms. *Natural Hazards*, 81(2):909–938, Mar 2016. ISSN 1573-0840. doi: 10.1007/s11069-015-2111-1.

[63] Osamu Kamigaichi. Tsunami Forecasting and Warning. In *Extreme Environmental Events: Complexity in Forecasting and Early Warning*, pages 982–1007. Springer New York, New York, NY, 2011. ISBN 978-1-4419-7695-6.

[64] Andrew B. Kennedy, Uriah Gravois, Brian C. Zachry, Joannes J. Westerink, Mark E. Hope, J. Casey Dietrich, Mark D. Powell, Andrew T. Cox, Richard A. Luettich Jr., and Robert G. Dean. Origin of the hurricane ike forerunner surge. *Geophysical Research Letters*, 38(8), 2011. doi: 10.1029/2011GL047090.

[65] Andrew B. Kennedy, Joannes J. Westerink, Jane M. Smith, Mark E. Hope, Michael Hartman, Alexandros A. Taflanidis, Seizo Tanaka, Hans Westerink, Kwok Fai Cheung, Tom Smith, Madeleine Hamann, Masashi Minamide, Aina Ota, and Clint Dawson. Tropical cyclone inundation potential on the hawaiian islands of oahu and kauai. *Ocean Modelling*, 52-53:54–68, 2012. ISSN 1463-5003. doi: 10.1016/j.ocemod.2012.04.009.

[66] P. C. Kerr, R. C. Martyr, A. S. Donahue, M. E. Hope, J. J. Westerink, R. A. Luettich Jr., A. B. Kennedy, J. C. Dietrich, C. Dawson, and H. J. Westerink. U.s. ioos coastal and ocean modeling testbed: Evaluation of tide, wave, and hurricane surge response sensitivities to mesh resolution and friction in the gulf of mexico. *Journal of Geophysical Research: Oceans*, 118(9):4633–4661, 2013. doi: 10.1002/jgrc.20305.

[67] Seung-Woo Kim, Jeffrey A. Melby, Norberto C. Nadal-Caraballo, and Jay Ratcliff. A time-dependent surrogate model for storm surge prediction based on an artificial neural network using high-fidelity synthetic hurricane modeling. *Natural Hazards*, 76 (1):565–585, Mar 2015. ISSN 1573-0840. doi: 10.1007/s11069-014-1508-6.

[68] Diederik P Kingma and Jimmy Ba. Adam: A method for stochastic optimization. *arXiv preprint arXiv:1412.6980*, 2014.

[69] T. Kotani, K. Tozato, S. Takase, S. Moriguchi, K. Terada, Y. Fukutani, Y. Otake, K. Nojima, M. Sakuraba, and Y. Choe. Probabilistic tsunami hazard assessment with simulation-based response surfaces. *Coastal Engineering*, 160:103719, 2020. ISSN 0378-3839. doi: 10.1016/j.coastaleng.2020.103719.

[70] Y. Krien, B. Dudon, J. Roger, and N. Zahibo. Probabilistic hurricane-induced storm surge hazard assessment in guadeloupe, lesser antilles. *Natural Hazards and Earth System Sciences*, 15(8):1711–1720, 2015. doi: 10.5194/nhess-15-1711-2015.

[71] Evgueni A Kulikov, Alexander B Rabinovich, and Richard E Thomson. Estimation of tsunami risk for the coasts of Peru and northern Chile. *Natural Hazards*, 35(2): 185–209, 2005.

[72] Aikaterini P. Kyprioti, Alexandros A. Taflanidis, Norberto C. Nadal-Caraballo, and Madison Campbell. Storm hazard analysis over extended geospatial grids utilizing

surrogate models. *Coastal Engineering*, page 103855, 2021. ISSN 0378-3839. doi: 10.1016/j.coastaleng.2021.103855.

[73] Christopher W Landsea and James L Franklin. Atlantic hurricane database uncertainty and presentation of a new database format. *Monthly Weather Review*, 141(10):3576–3592, 2013.

[74] Emily M Lane, Jose Borrero, Colin N Whittaker, Jo Bind, Catherine Chagué-Goff, James Goff, Derek Goring, Jo Hoyle, Christof Mueller, William L Power, et al. Effects of inundation by the 14th november, 2016 Kaikōura tsunami on banks Peninsula, Canterbury, New Zealand. *Pure and Applied Geophysics*, 174(5):1855–1874, 2017. doi: 10.1007/s00024-017-1534-x.

[75] Thorne Lay, Charles J Ammon, Hiroo Kanamori, Lian Xue, and Marina J Kim. Possible large near-trench slip during the 2011 Mw 9.0 off the Pacific coast of Tohoku Earthquake. *Earth, planets and space*, 63(7):32, 2011.

[76] Thorne Lay, Han Yue, Emily E. Brodsky, and Chao An. The 1 April 2014 Iquique, Chile, Mw 8.1 earthquake rupture sequence. *Geophysical Research Letters*, 41(11):3818–3825, 2014. doi: 10.1002/2014GL060238.

[77] Jun-Whan Lee, Jennifer L Irish, and Robert Weiss. Rapid prediction of alongshore run-up distribution from near-field tsunamis. *Natural Hazards*, 104(2):1157–1180, 2020. doi: 10.1007/s11069-020-04209-z.

[78] Randall J. LeVeque, David L. George, and Marsha J. Berger. Tsunami modelling with adaptively refined finite volume methods. *Acta Numerica*, 20:211–289, 2011. doi: 10.1017/S0962492911000043.

[79] Linlin Li, Adam D. Switzer, Chung-Han Chan, Yu Wang, Robert Weiss, and Qiang

Qiu. How heterogeneous coseismic slip affects regional probabilistic tsunami hazard assessment: A case study in the South China Sea. *Journal of Geophysical Research: Solid Earth*, 121(8):6250–6272, 2016. doi: 10.1002/2016JB013111.

[80] Linlin Li, Adam D Switzer, Yu Wang, Chung-Han Chan, Qiang Qiu, and Robert Weiss. A modest 0.5-m rise in sea level will double the tsunami hazard in Macau. *Science advances*, 4(8), 2018. doi: 10.1126/sciadv.aat1180.

[81] Ming Li, Fan Zhang, Samuel Barnes, and Xiaohong Wang. Assessing storm surge impacts on coastal inundation due to climate change: case studies of baltimore and dorchester county in maryland. *Natural Hazards*, 103(2):2561–2588, Sep 2020. ISSN 1573-0840. doi: 10.1007/s11069-020-04096-4.

[82] N. Lin, K. A. Emanuel, J. A. Smith, and E. Vanmarcke. Risk assessment of hurricane storm surge for new york city. *Journal of Geophysical Research: Atmospheres*, 115 (D18), 2010. doi: 10.1029/2009JD013630.

[83] Simon C. Lin, Tso-Ren Wu, Eric Yen, Hsin-Yen Chen, John Hsu, Yu-Lin Tsai, Chun-Juei Lee, and L.-F. Liu Philip. Development of a tsunami early warning system for the South China Sea. *Ocean Engineering*, 100:1–18, 2015. ISSN 0029-8018. doi: 10.1016/j.oceaneng.2015.02.003.

[84] Yi Liu and Jennifer L. Irish. Characterization and prediction of tropical cyclone forerunner surge. *Coastal Engineering*, 147:34–42, 2019. ISSN 0378-3839. doi: 10.1016/j.coastaleng.2019.01.005.

[85] Alberto M López-Venegas, Juan Horrillo, Alyssa Pampell-Manis, Victor Huérfano, and Aurelio Mercado. Advanced tsunami numerical simulations and energy considerations by use of 3D–2D coupled models: The October 11, 1918, Mona passage tsunami. *Pure and Applied Geophysics*, 172(6):1679–1698, 2015. doi: 10.1007/s00024-014-0988-3.

[86] Richard Albert Luettich, Joannes J Westerink, Norman W Scheffner, et al. Adcirc: an advanced three-dimensional circulation model for shelves, coasts, and estuaries. report 1, theory and methodology of adcirc-2dd1 and adcirc-3dl. Technical report, 1992. URL https://hdl.handle.net/11681/4618.

[87] Breanyn T. MacInnes, Robert Weiss, Joanne Bourgeois, and Tatiana K. Pinegina. Slip distribution of the 1952 Kamchatka Great Earthquake based on near-field tsunami deposits and historical records. *Bulletin of the Seismological Society of America*, 100 (4):1695–1709, 2010. ISSN 0037-1106. doi: 10.1785/0120090376.

[88] Kyle T Mandli, Aron J Ahmadia, Marsha Berger, Donna Calhoun, David L George, Yiannis Hadjimichael, David I Ketcheson, Grady I Lemoine, and Randall J LeVeque. Clawpack: building an open source ecosystem for solving hyperbolic PDEs. *PeerJ Computer Science*, 2:e68, 2016. doi: 10.7717/peerj-cs.68.

[89] M. Elizabeth Martin, Robert Weiss, Joanne Bourgeois, Tatiana K. Pinegina, Heidi Houston, and Vasily V. Titov. Combining constraints from tsunami modeling and sedimentology to untangle the 1969 Ozernoi and 1971 Kamchatskii tsunamis. *Geophysical Research Letters*, 35(1), 2008. doi: 10.1029/2007GL032349.

[90] T Chris Massey, Mary E Anderson, Jane McKee Smith, Julieta M Gomez, and Rusty Jones. Stwave: Steady-state spectral wave model user's manual for stwave, version 6.0. 2011.

[91] Nobuhito Mori, Katsuichiro Goda, and Daniel Cox. Recent Process in Probabilistic Tsunami Hazard Analysis (PTHA) for Mega Thrust Subduction Earthquakes. In *The 2011 Japan Earthquake and Tsunami: Reconstruction and Restoration*, pages 469–485. Springer, 2018.

[92] Iyan E Mulia, Aditya Riadi Gusman, and Kenji Satake. Alternative to non-linear model for simulating tsunami inundation in real-time. *Geophysical Journal International*, 214 (3):2002–2013, 2018. ISSN 0956-540X. doi: 10.1093/gji/ggy238.

[93] Raymond H. Myers, Douglas C. Montgomery, and Christine M. Anderson-Cook. *Response surface methodology: process and product optimization using designed experiments*. John Wiley & Sons, 2016.

[94] Norberto C. Nadal-Caraballo, Jeffrey A. Melby, Victor M. Gonzalez, and Andrew T. Cox. Coastal storm hazards from Virginia to Maine. Technical Report ERDC/CHL TR-15-5, U.S. Army Engineer Research and Development Center, Coastal and Hydraulics Laboratory, Vicksburg, MS, November 2015. URL https://hdl.handle.net/11681/7715.

[95] Norberto C. Nadal-Caraballo, Madison O. Campbell, Victor M. Gonzalez, Marissa J. Torres, Jeffrey A. Melby, and Alexandros A. Taflanidis. Coastal hazards system: A probabilistic coastal hazard analysis framework. *Journal of Coastal Research*, 95(SI): 1211–1216, Jun 2020. ISSN 0749-0208. doi: 10.2112/SI95-235.1.

[96] Futoshi Nanayama, Kenji Satake, Ryuta Furukawa, Koichi Shimokawa, Brian F Atwater, Kiyoyuki Shigeno, and Shigeru Yamaki. Unusually large earthquakes inferred from tsunami deposits along the Kuril trench. *Nature*, 424(6949):660–663, 2003.

[97] National Research Council. *Tsunami Warning and Preparedness: An Assessment of the U.S. Tsunami Program and the Nation's Preparedness Efforts*. The National Academies Press, Washington, DC, 2011. ISBN 978-0-309-13753-9. doi: 10.17226/12628.

[98] Jeffrey W. Nealon and William P. Dillon. Earthquakes and tsunamis in Puerto Rico and the US Virgin Islands. Technical report, US Geological Survey, 2001.

[99] Hal F. Needham and Barry D. Keim. Correlating storm surge heights with tropical cyclone winds at and before landfall. *Earth Interactions*, 18(7):1 – 26, 2014. doi: 10.1175/2013EI000527.1.

[100] NGDC. Data from "U.S. Coastal Relief Model - Puerto Rico." National Geophysical Data Center, NOAA. Available at https://dx.doi.org/10.7289/V57H1GGW. Deposited 1 January 2005. , 2005. URL https://www.ncei.noaa.gov/metadata/geoportal/rest/metadata/item/gov.noaa.ngdc.mgg.dem:290/html.

[101] NOAA. Service assessment: Hurricane isabel september 18-19, 2003. Technical report, National Weather Service, Silver Spring, Maryland, May 2004. URL https://repository.library.noaa.gov/view/noaa/6471.

[102] NOAA. Tides and currents, 2020. URL https://tidesandcurrents.noaa.gov/.

[103] NOAA National Centers for Environmental Information (NCEI). U.S. Billion-Dollar Weather and Climate Disasters, 2021. URL https://www.ncdc.noaa.gov/billions/.

[104] Yoshimitsu Okada. Surface deformation due to shear and tensile faults in a half-space. *Bulletin of the seismological society of America*, 75(4):1135–1154, 1985.

[105] Emile A. Okal and Costas E. Synolakis. Source discriminants for near-field tsunamis. *Geophysical Journal International*, 158(3):899–912, 2004. ISSN 0956540X. doi: 10.1111/j.1365-246X.2004.02347.x.

[106] Alexandre Paris, Emile A Okal, Cyrielle Guérin, Philippe Heinrich, François Schindelé, and Hélène Hébert. Numerical Modeling of the June 17, 2017 Landslide and Tsunami Events in Karrat Fjord, West Greenland. *Pure and Applied Geophysics*, pages 1–23, 2019. doi: 10.1007/s00024-019-02123-5.

[107] Hyoungsu Park and Daniel T. Cox. Probabilistic assessment of near-field tsunami hazards: Inundation depth, velocity, momentum flux, arrival time, and duration applied to seaside, oregon. *Coastal Engineering*, 117:79–96, 2016. ISSN 0378-3839. doi: 10.1016/j.coastaleng.2016.07.011.

[108] Hyoungsu Park and Daniel T Cox. Probabilistic assessment of near-field tsunami hazards: Inundation depth, velocity, momentum flux, arrival time, and duration applied to Seaside, Oregon. *Coastal Engineering*, 117:79–96, 2016. doi: 10.1016/j.coastaleng.2016.07.011.

[109] Hyoungsu Park, Daniel T Cox, and Andre R Barbosa. Probabilistic Tsunami Hazard Assessment (PTHA) for resilience assessment of a coastal community. *Natural Hazards*, 94(3):1117–1139, 2018. doi: 10.1007/s11069-018-3460-3.

[110] F. Pedregosa, G. Varoquaux, A. Gramfort, V. Michel, B. Thirion, O. Grisel, M. Blondel, P. Prettenhofer, R. Weiss, V. Dubourg, J. Vanderplas, A. Passos, D. Cournapeau, M. Brucher, M. Perrot, and E. Duchesnay. Scikit-learn: Machine learning in Python. *Journal of Machine Learning Research*, 12:2825–2830, 2011.

[111] Alessio Piatanesi, Stefano Tinti, and Ivan Gavagni. The slip distribution of the 1992 Nicaragua Earthquake from tsunami run-up data. *Geophysical Research Letters*, 23 (1):37–40, 1996. doi: 10.1029/95GL03606.

[112] Stéphane Popinet. A quadtree-adaptive multigrid solver for the Serre–Green–Naghdi equations. *Journal of Computational Physics*, 302:336–358, 2015. doi: 10.1016/j.jcp.2015.09.009.

[113] Edward N. Rappaport. Fatalities in the united states from atlantic tropical cyclones: New data and interpretation. *Bulletin of the American Meteorological Society*, 95(3): 341 – 346, 2014. doi: 10.1175/BAMS-D-12-00074.1.

[114] Harry Fielding Reid and Stephen Taber. The Porto Rico Earthquakes of October-November, 1918. *Bulletin of the Seismological Society of America*, 9(4):95–127, 1919.

[115] Donald T. Resio, Stanley J. Boc, Leon E. Borgman, Vince J. Cardone, Andrew W. Cox, William R. Dally, Robert G. Dean, D. Divoky, Emily. Hirsh, Jennifer L. Irish, David. Levinson, Alan W. Niedoroda, Mark D. Powell, Jay J. Ratcliff, Vann. Stutts, J. N. Suhayda, Gabriel R. Toro, Peter J. Vickery, and Joannes J. Westerink. White paper on estimating hurricane inundation probabilities. Technical report, U.S. Army Engineer Research and Development Center, Coastal and Hydraulics Laboratory, Vicksburg, MS, May 2007. URL https://hdl.handle.net/11681/22643.

[116] Ian N. Robertson, H. Ronald Riggs, Solomon C. Yim, and Yin Lu Young. Lessons from hurricane katrina storm surge on bridges and buildings. *Journal of Waterway, Port, Coastal, and Ocean Engineering*, 133(6):463–483, 2007. doi: 10.1061/(ASCE)0733-950X(2007)133:6(463).

[117] Fabrizio Romano, Alessio Piatanesi, Stefano Lorito, Cristiano Tolomei, Simone Atzori, and S Murphy. Optimal time alignment of tide-gauge tsunami waveforms in nonlinear inversions: Application to the 2015 Illapel (Chile) earthquake. *Geophysical Research Letters*, 43(21):11–226, 2016.

[118] Michele Romano, Shie-Yui Liong, Minh Tue Vu, Pavlo Zemskyy, Chi Dung Doan, My Ha Dao, and Pavel Tkalich. Artificial neural network for tsunami forecasting. *Journal of Asian Earth Sciences*, 36(1):29–37, 2009. ISSN 1367-9120. doi: 10.1016/j.jseaes.2008.11.003.

[119] J. A. Ruiz, M. Fuentes, S. Riquelme, J. Campos, and A. Cisternas. Numerical simulation of tsunami runup in northern Chile based on non-uniform k−2slip distri-

butions. *Natural Hazards*, 79(2):1177–1198, 2015. ISSN 15730840. doi: 10.1007/s11069-015-1901-9.

[120] Asbury H. Sallenger, Kara S. Doran, and Peter A. Howd. Hotspot of accelerated sea-level rise on the atlantic coast of north america. *Nature Climate Change*, 2(12): 884–888, Dec 2012. ISSN 1758-6798. doi: 10.1038/nclimate1597.

[121] Shinji Sassa and Tomohiro Takagawa. Liquefied gravity flow-induced tsunami: first evidence and comparison from the 2018 Indonesia Sulawesi earthquake and tsunami disasters. *Landslides*, 16(1):195–200, 2019. doi: 10.1007/s10346-018-1114-x.

[122] Kenji Satake. Inversion of tsunami waveforms for the estimation of a fault heterogeneity: Method and numerical experiments. *Journal of Physics of the Earth*, 35(3): 241–254, 1987.

[123] Kenji Satake. *Tsunamis, Inverse Problem of*, pages 9631–9644. Springer New York, New York, NY, 2009. ISBN 978-0-387-30440-3. doi: 10.1007/978-0-387-30440-3_570.

[124] Bernd Schurr, Günter Asch, Sebastian Hainzl, Jonathan Bedford, Andreas Hoechner, Mauro Palo, Rongjiang Wang, Marcos Moreno, Mitja Bartsch, Yong Zhang, et al. Gradual unlocking of plate boundary controlled initiation of the 2014 Iquique earthquake. *Nature*, 512(7514):299–302, 2014.

[125] Ignacio Sepúlveda, Philip L.-F. Liu, and Mircea Grigoriu. Probabilistic tsunami hazard assessment in south china sea with consideration of uncertain earthquake characteristics. *Journal of Geophysical Research: Solid Earth*, 124(1):658–688, 2019. doi: 10.1029/2018JB016620.

[126] Urip Setiyono, Aditya Riadi Gusman, Kenji Satake, and Yushiro Fujii. Pre-computed tsunami inundation database and forecast simulation in Pelabuhan Ratu, Indonesia.

Pure and Applied Geophysics, 174(8):3219–3235, Aug 2017. ISSN 1420-9136. doi: 10.1007/s00024-017-1633-8.

[127] Jian Shen, Harry Wang, Mac Sisson, and Wenping Gong. Storm tide simulation in the chesapeake bay using an unstructured grid model. *Estuarine, Coastal and Shelf Science*, 68(1):1–16, 2006. ISSN 0272-7714. doi: 10.1016/j.ecss.2005.12.018.

[128] Y. Peter Sheng, Vadim Alymov, and Vladimir A. Paramygin. Simulation of storm surge, wave, currents, and inundation in the Outer Banks and Chesapeake Bay during Hurricane Isabel in 2003: The importance of waves. *Journal of Geophysical Research: Oceans*, 115(C4), 2010. doi: 10.1029/2009JC005402.

[129] Fengyan Shi, James T Kirby, Jeffrey C Harris, Joseph D Geiman, and Stephan T Grilli. A high-order adaptive time-stepping TVD solver for Boussinesq modeling of breaking waves and coastal inundation. *Ocean Modelling*, 43:36–51, 2012. doi: 10.1016/j.ocemod.2011.12.004.

[130] Mahesh N Shrivastava, Gabriel González, Marcos Moreno, Hugo Soto, Bernd Schurr, Pablo Salazar, and Juan Carlos Báez. Earthquake segmentation in northern Chile correlates with curved plate geometry. *Scientific reports*, 9(1):1–10, 2019.

[131] Youn Kyung Song, Jennifer L. Irish, and Ikpoto E. Udoh. Regional attributes of hurricane surge response functions for hazard assessment. *Natural Hazards*, 64(2):1475–1490, Nov 2012. ISSN 1573-0840. doi: 10.1007/s11069-012-0309-z.

[132] Nitish Srivastava, Geoffrey Hinton, Alex Krizhevsky, Ilya Sutskever, and Ruslan Salakhutdinov. Dropout: a simple way to prevent neural networks from overfitting. *The journal of machine learning research*, 15(1):1929–1958, 2014.

[133] C.E. Synolakis and E.A. Okal. *1992–2002: Perspective on a Decade of Post-Tsunami Surveys*, pages 1–29. Springer Netherlands, Dordrecht, 2005. doi: 10.1007/1-4020-3331-1_1.

[134] Alexandros A. Taflanidis, Gaofeng Jia, Andrew B. Kennedy, and Jane M. Smith. Implementation/optimization of moving least squares response surfaces for approximation of hurricane/storm surge and wave responses. *Natural Hazards*, 66(2):955–983, 2013. ISSN 0921030X. doi: 10.1007/s11069-012-0520-y.

[135] Alexandros A. Taflanidis, Andrew B. Kennedy, Joannes J. Westerink, Jane Smith, Kwok Fai Cheung, Mark Hope, and Seizo Tanaka. Rapid assessment of wave and surge risk during landfalling hurricanes: Probabilistic approach. *Journal of Waterway, Port, Coastal, and Ocean Engineering*, 139(3):171–182, 2013. doi: 10.1061/(ASCE)WW.1943-5460.0000178.

[136] Nick R. Taylor, Jennifer L. Irish, Ikpoto E. Udoh, Matthew V. Bilskie, and Scott C. Hagen. Development and uncertainty quantification of hurricane surge response functions for hazard assessment in coastal bays. *Natural Hazards*, 77(2):1103–1123, Jun 2015. doi: 10.1007/s11069-015-1646-5.

[137] Kiran Kumar S. Thingbaijam, P. Martin Mai, and Katsuichiro Goda. New empirical earthquake source-scaling laws. *Bulletin of the Seismological Society of America*, 107 (5):2225–2246, 2017. ISSN 19433573. doi: 10.1785/0120170017.

[138] Ajimon Thomas, JC Dietrich, TG Asher, M Bell, BO Blanton, JH Copeland, AT Cox, CN Dawson, JG Fleming, and RA Luettich. Influence of storm timing and forward speed on tides and storm surge during hurricane matthew. *Ocean Modelling*, 137:1–19, 2019. ISSN 1463-5003. doi: 10.1016/j.ocemod.2019.03.004.

[139] Edward F. Thompson and Vincent J. Cardone. Practical modeling of hurricane surface wind fields. *Journal of Waterway, Port, Coastal, and Ocean Engineering*, 122(4):195–205, 1996. doi: 10.1061/(ASCE)0733-950X(1996)122:4(195).

[140] Vasily Titov, Alexander B Rabinovich, Harold O Mofjeld, Richard E Thomson, and Frank I González. The global reach of the 26 December 2004 Sumatra tsunami. *Science*, 309(5743):2045–2048, 2005. doi: 10.1126/science.1114576.

[141] Vasily V. Titov, Frank I. Gonzalez, E. N. Bernard, Marie C. Eble, Harold O. Mofjeld, Jean C. Newman, and Angie J. Venturato. Real-time tsunami forecasting: Challenges and solutions. *Natural Hazards*, 35(1):35–41, May 2005. ISSN 1573-0840. doi: 10.1007/s11069-004-2403-3.

[142] Elena Tolkova, Hitoshi Tanaka, and Min Roh. Tsunami observations in rivers from a perspective of tsunami interaction with tide and riverine flow. *Pure and Applied Geophysics*, 172(3-4):953–968, 2015. doi: 10.1007/s00024-014-1017-2.

[143] Gabriel R Toro, Donald T Resio, David Divoky, Alan Wm Niedoroda, and Chris Reed. Efficient joint-probability methods for hurricane surge frequency analysis. *Ocean Engineering*, 37(1):125–134, 2010.

[144] S Uri, Homa J Lee, Eric L Geist, and David Twichell. Assessment of tsunami hazard to the US East Coast using relationships between submarine landslides and earthquakes. *Marine Geology*, 264(1-2):65–73, 2009. doi: 10.1016/j.margeo.2008.05.011.

[145] USGS. Data from "Advanced National Seismic System (ANSS) Comprehensive Catalog of Earthquake Events and Products." Earthquake Hazards Program, U.S. Geological Survey. Available at https://doi.org/10.5066/F7MS3QZH. Deposited 1 January 2017, 2017. URL https://earthquake.usgs.gov/earthquakes/search/.

[146] Thaddeus Vincenty. Direct and inverse solutions of geodesics on the ellipsoid with application of nested equations. *Survey review*, 23(176):88–93, 1975.

[147] Thomas Wahl, Shaleen Jain, Jens Bender, Steven D. Meyers, and Mark E. Luther. Increasing risk of compound flooding from storm surge and rainfall for major us cities. *Nature Climate Change*, 5(12):1093–1097, Dec 2015. ISSN 1758-6798. doi: 10.1038/nclimate2736.

[148] Yong Wei, Christopher Chamberlin, Vasily V Titov, Liujuan Tang, and Eddie N Bernard. Modeling of the 2011 Japan tsunami: Lessons for near-field forecast. *Pure and Applied Geophysics*, 170(6-8):1309–1331, 2013. doi: 10.1007/s00024-012-0519-z.

[149] Amy Williamson, Andrew Newman, and Phil Cummins. Reconstruction of coseismic slip from the 2015 Illapel earthquake using combined geodetic and tsunami waveform data. *Journal of Geophysical Research: Solid Earth*, 122(3):2119–2130, 2017. doi: 10.1002/2016JB013883.

[150] Jonathan D. Woodruff, Jennifer L. Irish, and Suzana J. Camargo. Coastal flooding by tropical cyclones and sea-level rise. *Nature*, 504(7478):44–52, Dec 2013. ISSN 1476-4687. doi: 10.1038/nature12855.

[151] Yusuke Yokota, Kazuki Koketsu, Yushiro Fujii, Kenji Satake, Shin'ichi Sakai, Masanao Shinohara, and Toshihiko Kanazawa. Joint inversion of strong motion, teleseismic, geodetic, and tsunami datasets for the rupture process of the 2011 Tohoku earthquake. *Geophysical Research Letters*, 38(7), 2011. doi: 10.1029/2011GL050098.

[152] Han Yue, Thorne Lay, Luis Rivera, Chao An, Christophe Vigny, Xiaopeng Tong, and Juan Carlos Báez Soto. Localized fault slip to the trench in the 2010 Maule, Chile Mw = 8.8 earthquake from joint inversion of high-rate GPS, teleseismic body waves,

InSAR, campaign GPS, and tsunami observations. *Journal of Geophysical Research: Solid Earth*, 119(10):7786–7804, 2014. doi: 10.1002/2014JB011340.

[153] Amir Zainali, Roberto Marivela, Robert Weiss, Yongqian Yang, and Jennifer L Irish. Numerical simulation of nonlinear long waves in the presence of discontinuous coastal vegetation. *Marine Geology*, 396:142–149, 2018. doi: 10.1016/j.margeo.2017.08.001.

[154] Jize Zhang, Alexandros A. Taflanidis, Norberto C. Nadal-Caraballo, Jeffrey A. Melby, and Fatimata Diop. Advances in surrogate modeling for storm surge prediction: storm selection and addressing characteristics related to climate change. *Natural Hazards*, 94 (3):1225–1253, Dec 2018. ISSN 1573-0840. doi: 10.1007/s11069-018-3470-1.

[155] Yinglong J. Zhang, Robert C. Witter, and George R. Priest. Tsunami–tide interaction in 1964 Prince William Sound tsunami. *Ocean Modelling*, 40(3-4):246–259, 2011. doi: 10.1016/j.ocemod.2011.09.005.

[156] Tong Zhou, Lingsen Meng, Yuqing Xie, and Jiayuan Han. An adjoint-state full-waveform tsunami source inversion method and its application to the 2014 Chile-Iquique tsunami event. *Journal of Geophysical Research: Solid Earth*, 124(7):6737–6750, 2019. doi: 10.1029/2018JB016678.

Appendices

Appendix A

Chapter 2

A.1 Design of experiments

The tsunamigenic-earthquake scenarios were designed in a three-level full factorial. The level of the design of experiments (DoE) was determined based on preliminary simulations where 60 cases were considered as follows. We set a reference case where the fault parameters are as follows: $LON = 66.4°W$, $LAT = 19.3°N$, $STR = 90°$, $DIP = 20°$, $RAK = 90°$, $LEN = 90km$, $WID = 40km$, $SLP = 3m$, $DEP = 20km$, which are the same as the central level values used in Table 2.1. Based on the reference case, we performed 60 simulations, varying each of the six fault parameters (LAT, LEN, WID, DIP, SLP, DEP) one at a time through a uniformly distributed array of 10 values within the parameter's range shown in Table 2.1. The 60 simulations show that the 2nd order polynomial model, which requires at least three-level data, is enough to fit the fault parameters to the OS formula's coefficients a and b (Fig. A.1).

A.2 Sensitivity test

While developing the TRRF for northern Puerto Rico, we encountered numerical model stability issues with four simulations (0.5% of simulations) among the 729 scenarios. The stability issue occurred when the LAT is 19.6°, earthquake magnitude (LEN, WID, SLP)

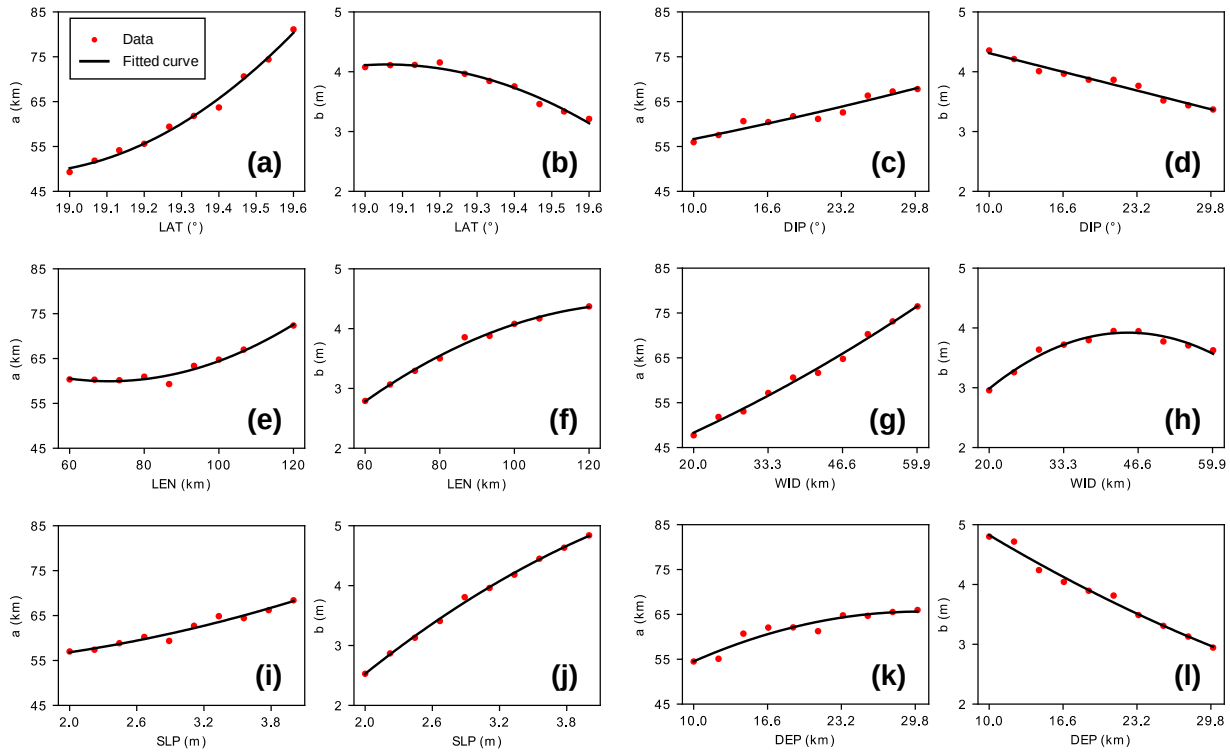

Figure A.1: The OS formula coefficients (a and b) variation in terms of RSM parameters: (a,b) epicenter latitude, (c,d) dip angle, (e,f) fault length, (g,h) fault width, (i,j) slip, (k,l) top-edge fault depth. The red dots represent the simulated coefficients and the black line represents the best-fitting curve based on the 2nd-order polynomial model.

is relatively large, DIP is shallow, and DEP is deep (Table A.1). Even though it is difficult to fully interpret the reason of this stability problem, we think that one of the reasons may be that some part of the fault lies in the Puerto Rico Trench where the water depth abruptly changes, and the grid resolution used in this study may not be sufficiently resolved for the case when the fault lies in steep slopes (Fig. 2.2). In order to test whether building the TRRF with 725 instead of 729 simulations affected the accuracy of the TRRF, we conducted a sensitivity test as follows. We randomly chose four simulations among the 725 successful simulations. We built the TRRF with 721 simulations, where the four randomly chosen scenarios were intentionally removed. We tested this TRRF based on the 100 simulation cases used in Test 4, which were never used in developing the TRRF and whose fault parameters were selected

Table A.1: Fault parameter condition of four cases that shows model stability issue.

	Case 1	Case 2	Case 3	Case 4
$LON(°W)$	66.4	66.4	66.4	66.4
$LAT(°N)$	19.6	19.6	19.6	19.6
$STR(°)$	90	90	90	90
$DIP(°)$	10	10	20	20
$RAK(°)$	90	90	90	90
$LEN(km)$	90	90	120	120
$WID(km)$	60	60	60	60
$SLP(m)$	4	4	4	4
$DEP(km)$	20	30	20	30

randomly. We repeated this procedure 10 different times. The result of the sensitivity test shows that the impact on accuracy of building the TRRF without four additional simulations is negligible (the largest difference of $NRMSE = 1.27\%$).

Appendix B

Chapter 3

B.1 TRRF training, calibration, and validation

To train the TRRF model for the northern Chile coastal region, 729 ($= 3^6$) tsunamigenic-earthquake scenarios were simulated. The 729 scenarios were generated in three-level factorial design (low, central, high) of six fault parameters (LON, DIP, LEN, WID, SLP, DEP) as listed in Table 3.1. The range of the epicenter longitude LON was determined based on the historical earthquake records in the northern Chile region (Fig. 3.1). The range of the fault length LEN, fault width WID, and slip SLP was set considering the moment magnitude ($M_W = 8.2$) of the 2014 Iquique earthquake. The minimum LEN and the minimum WID were set to 90 km and 40 km, respectively, considering the uncertainty (1σ) of Blaser et al. [11]'s scaling law. The maximum LEN was set to 180 km based on the assumption that the uniform slip distribution is applicable up to 180 km. The maximum WID was limited to 90 km considering the distance between the plate boundary and the coastline. The range of the dip angle DIP and the depth of the top edge DEP were determined based on the tectonic characteristics of the northern Chile region [23, 49, 130]. In order to apply the Okal and Synolakis [105]'s empirical formula, the strike angle (STR) was set parallel to the coastline, and the rake angle (RAK) was set to the angle that makes the strike direction perpendicular to the coastline. The epicenter latitude (LAT) was fixed to the near point of the city of Iquique ($20°S$). The initial free surface displacement was

calculated using the Okada [104]'s equations assuming an instantaneous fault rupture. The bathymetry and topography data were from the 15 arc-second dataset [35]. The bottom drag coefficient of a quadratic drag law was fixed to 10^{-4}. Two hours of tsunami propagation and inundation were simulated to capture the late arrival peak run-up that could be caused by the edge waves [14]. The maximum water level was interpolated bilinearly onto a regular grid (0.004° intervals). The origin was set to (20°S, 71°W) and it was used as a reference point in the Vincenty [146]'s formula to change the coordinate system from a spherical coordinate system to a Cartesian coordinate system.

To calibrate the TRRF model, we systemically simulated two groups of scenarios. First, 75 scenarios were simulated where the fault parameters were selected as follows. We set 15 reference scenarios by randomly selecting seven fault parameters (LAT, LON, DIP, LEN, WID, SLP, DEP). For each reference scenario, five scenarios were generated where STR is 340°, 350°, 0°, 10°, and 20°, respectively, while RAK was fixed to 90°. Secondly, 100 scenarios were simulated where the fault parameters were selected as follows. We set 10 reference scenarios by randomly selecting the seven fault parameters (LAT, LON, DIP, LEN, WID, SLP, DEP). For each reference scenario, ten scenarios were generated where STR is 340°, 350°, 0°, 10°, and 20°, respectively, while RAK varies from 70° to 110° at intervals of 10°. Based on the simulation results, the TRRF model was calibrated as follows:

$$\theta = \begin{cases} 0.637STR - 0.063RAK - 133.65°, \ 340° \leq STR < 360° \\ 0.637STR - 0.063RAK + 95.67°, \ 0° \leq STR \leq 20° \end{cases} \tag{B.1}$$

$$\lambda = -0.147RAK + 103.23° \tag{B.2}$$

where θ is the adjusted strike angle and λ is the adjusted rake angle, used to consider the

case where the strike direction is not parallel to the coastline and/or the slip direction is not perpendicular to the coastline. More details on the calibration procedure and how the values (θ and λ) are used to estimate the tsunami run-up distribution can be found in Lee et al. [77].

To validate the TRRF model, we simulated additional 20 scenarios where the fault parameters were randomly selected within the range in Table 3.1. The range of six fault parameters (LON, DIP, LEN, WID, SLP, DEP) was set to the same range used in the TRRF training. The range of LAT was set based on the historical earthquake activities, including the 2014 Iquique earthquake. The range of STR was set based on the Slab model [51]. And we assumed that the RAK can vary $90° \pm 20°$. To generate scenarios similar to the 2014 Chile earthquake, we limited the scenarios to the cases where the maximum run-up was larger than 3 m. The fault parameters of 20 scenarios are listed in Supplementary Table S1. A comparison of tsunami run-up distribution between the TRRF model and the Basilisk model shows that the TRRF model can produce reliable run-up predictions (the range of $NRMSE$: $6.00\% - 13.92\%$, mean $NRMSE = 7.90\%$).

B.2 Step 2 example result

In step 2, the TRRF-INV model defines the estimation order from the most sensitive fault parameter (which shows the largest $\Delta\overline{NRMSE}$) to the least sensitive fault parameter (which shows the smallest $\Delta\overline{NRMSE}$). For example, in the case shown in Fig. B.1, the estimation order is LAT ($\Delta\overline{NRMSE} = 17.77\%$ *point*), SLP ($\Delta\overline{NRMSE} = 14.54\%$ *point*), LEN ($\Delta\overline{NRMSE} = 4.05\%$ *point*), WID ($\Delta\overline{NRMSE} = 1.65\%$ *point*), LON ($\Delta\overline{NRMSE} = 1.52\%$ *point*).

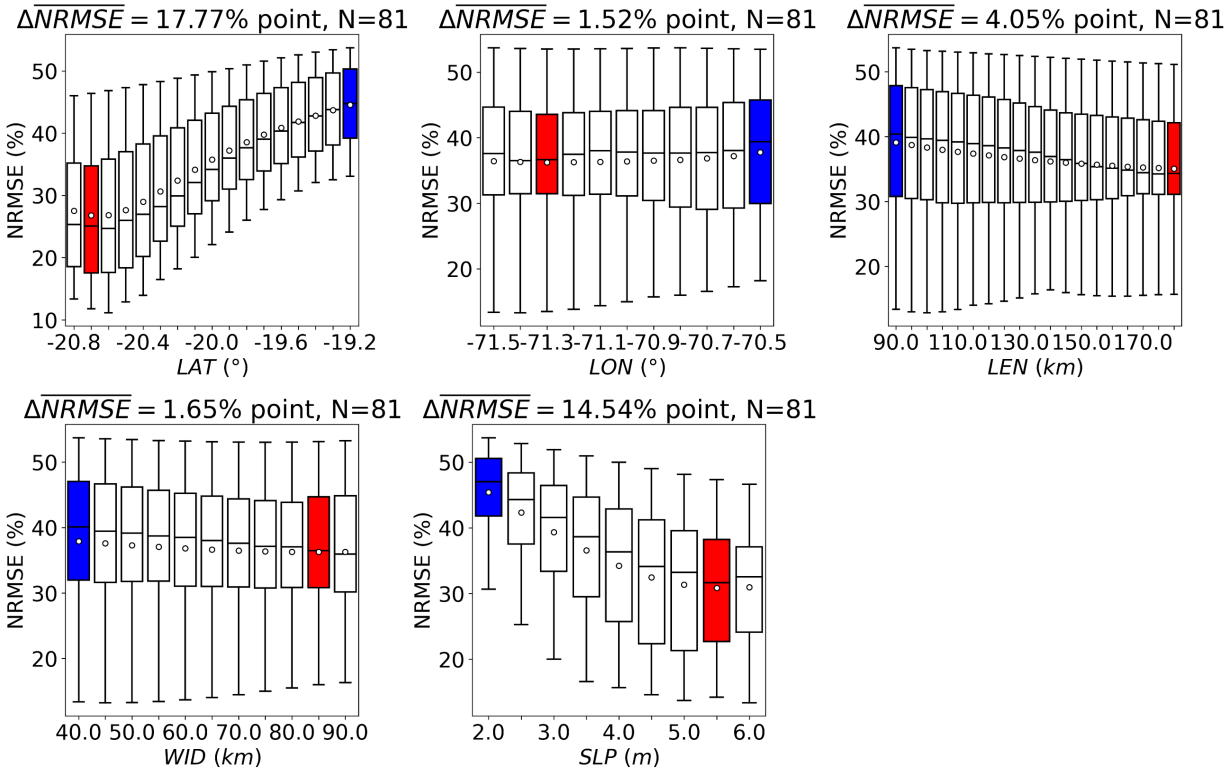

Figure B.1: Example of step 2 result of the TRRF-INV model. The boxes that show the maximum and the minimum values of mean $NRMSE$ are colored in blue and red, respectively. The maximum difference of mean $NRMSE$ ($\Delta\overline{NRMSE}$) is denoted on top of each figure. Each box-whisker plot consists of 81 scenarios (a combination of 3-level values of four fault parameters). The box symbol shows the interquartile range (box boundary), median (horizontal line), and mean (circle). The lower(upper) whisker is defined as 1.5 times the interquartile range below(above) the first(third) quartile.

B.3 Step 3 example result

In step 3, the TRRF-INV model estimates the fault parameters until one of the two stop conditions is satisfied. For example, in the case shown in Fig. B.2, the number of scenarios in the base group to estimate the fault length (LEN) at the fourth iteration ($j = 4$) is 6 (a combination of one LAT, two LON, three WID, and one SLP). Since the number of scenarios is smaller than the threshold ($N_Threshold = 10$), the TRRF-INV model stops iteration and saves the estimated fault parameters at the third iteration ($j = 3$).

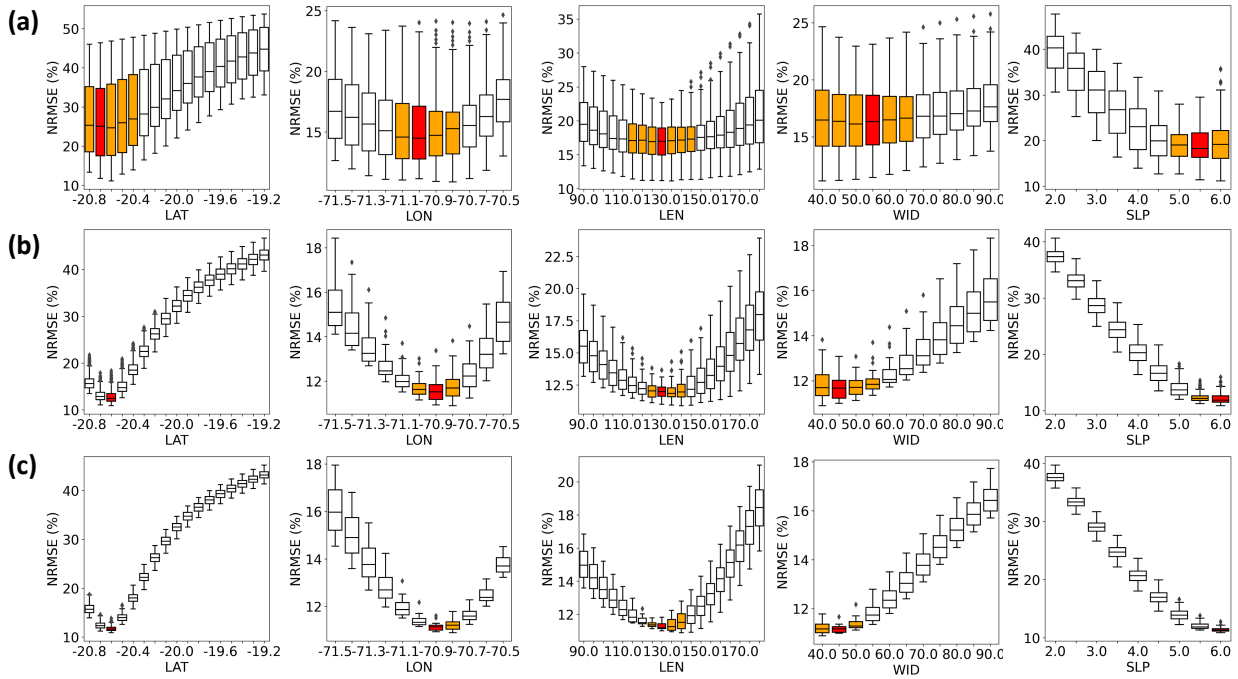

Figure B.2: Example of step 3 result of the TRRF-INV model: (a) First iteration ($j = 1$), (b) Second iteration ($j = 2$), (c) Third iteration ($j = 3$). The box that shows the minimum value of mean $NRMSE$ (or the base group) are colored in red. The orange boxes represent the other groups that show no statistically significant difference of mean $NRMSE$ compared to that of the red box (p-value > 0.05).

B.4 Determination of α value

To determine the α value of Eq. 3.8, we investigated the performance of the TRRF-INV model depending on the α values ($\alpha = 0.1, 0.2, 0.3, 0.4$) as shown in Fig. B.3. For each α value, we generated 20 random scenarios by selecting 20 random points for each of the base scenario (Table B.1). As the α value increases, the computational time of the TRRF-INV model increases because the number of filtered scenarios (N_s) increases. Moreover, as the α value increases, the errors of the fault length (LEN) and the tsunami run-up distribution ($NRMSE_t$) increase. However, the largest error of the epicenter latitude (LAT) and the lowest success rate (SR) were shown when $\alpha = 0.1$. Therefore, we set the α value to 0.2 to balance the computational time and the accuracy of the TRRF-INV model.

Table B.1: Fault parameters of 20 base scenarios used in TRRF validation

Case	LON(°)	LAT(°)	STR(°)	DIP(°)	RAK(°)	LEN(km)	WID(km)	SLP(m)	DEP(km)
1	-71.014	-20.524	345	16	110	179.811	41.865	5.25	29.951
2	-71.233	-20.398	348	26	83	172.022	68.695	5.74	29.562
3	-70.823	-20.751	352	21	86	167.842	42.393	3.1	28.999
4	-71.165	-19.371	353	28	77	129.866	65.061	4.03	20.031
5	-71.044	-20.485	351	21	103	173.901	51.095	5.67	20.522
6	-71.094	-20.426	345	28	75	166.512	67.971	4.54	25.825
7	-71.162	-19.666	342	28	101	129.111	56.462	5.31	28.811
8	-70.71	-20.144	356	19	86	90.764	66.365	5.35	23.486
9	-71.374	-19.602	351	18	75	179.105	78.485	4.79	21.613
10	-70.707	-19.646	348	26	83	92.349	72.572	5.53	29.49
11	-70.951	-19.297	342	10	76	146.129	55.054	4	21.968
12	-71.067	-20.585	354	14	96	110.688	86.154	4.63	20.716
13	-71.105	-20.216	359	24	74	174.122	74.148	5.12	28.06
14	-70.93	-20.7	341	18	92	90.632	56.604	5.73	24.128
15	-70.973	-19.3	351	15	74	125.876	43.515	5.64	29.623
16	-70.695	-19.887	351	26	105	150.03	83.605	5.9	21.355
17	-71.003	-19.351	355	19	73	170.244	41.594	5.98	23.094
18	-71.496	-20.669	355	22	93	125.553	81.77	4.12	21.539
19	-71.29	-20.487	344	28	83	112.349	68.636	5.09	22.504
20	-70.585	-20.649	351	16	103	179.536	48.157	4.1	25.457

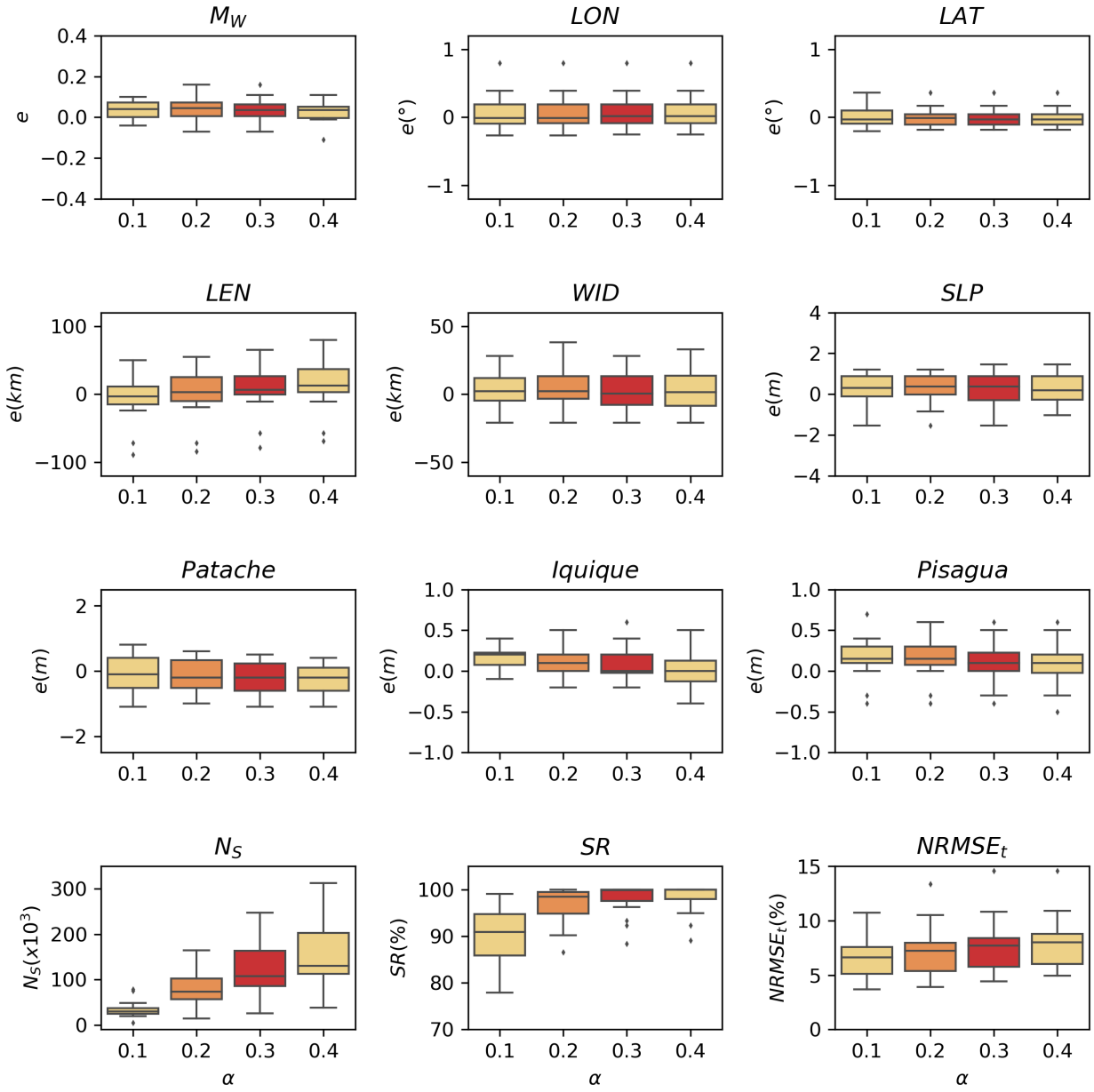

Figure B.3: Performance of the TRRF-INV model depending on the α value of Eq. (8). The error (e) is defined as the estimated value minus the true value. Each box-whisker plot consists of 20 random scenarios. The box symbol shows the interquartile range (box boundary), median (horizontal line). The lower(upper) whisker is defined as 1.5 times the interquartile range below(above) the first(third) quartile. The data beyond the whiskers is plotted as an outlier (diamond).

Appendix C

Chapter 4

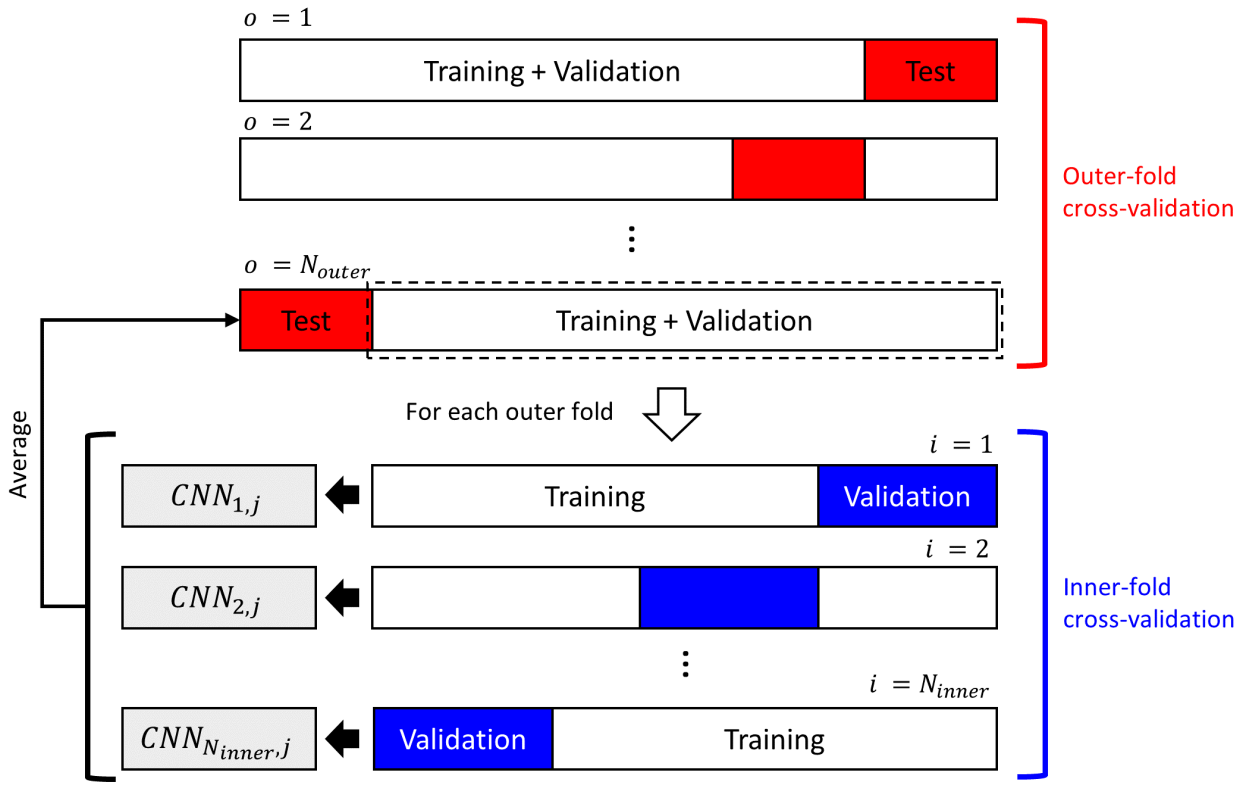

Figure C.1: Nested- K-fold cross-validation. For each outer-fold, we separated 10% data as a test set. For each inner-fold, we used 20% data as a validation set to prevent overfitting, and we used the average estimate of convolutional neural network (CNN) models as an output. Note that we shuffle the data before splitting into training set, validation set, and test set.

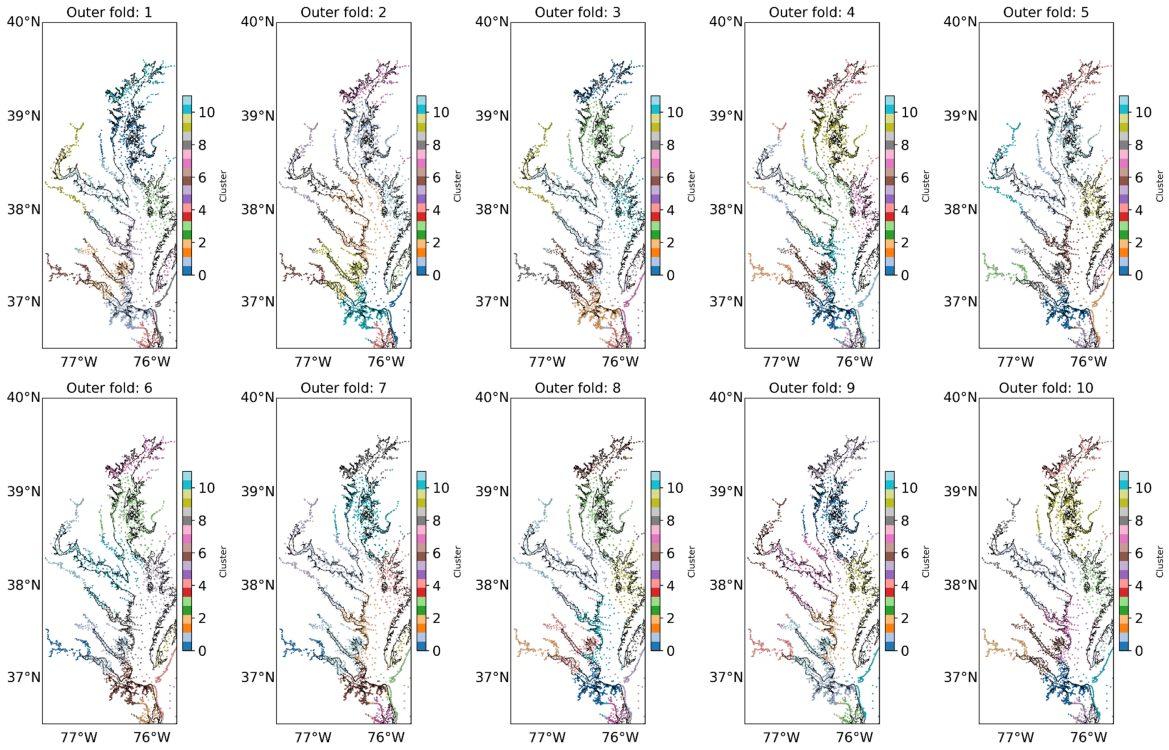

Figure C.2: Spatial distribution of clusters for each outer-fold. Each color represents a different cluster.

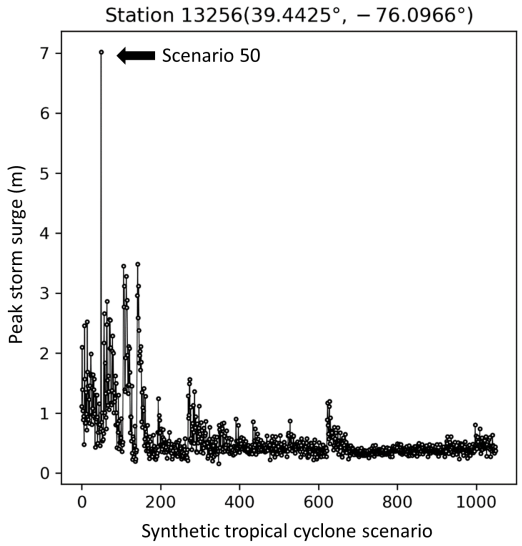

Figure C.3: Peak storm surges of station 13256.

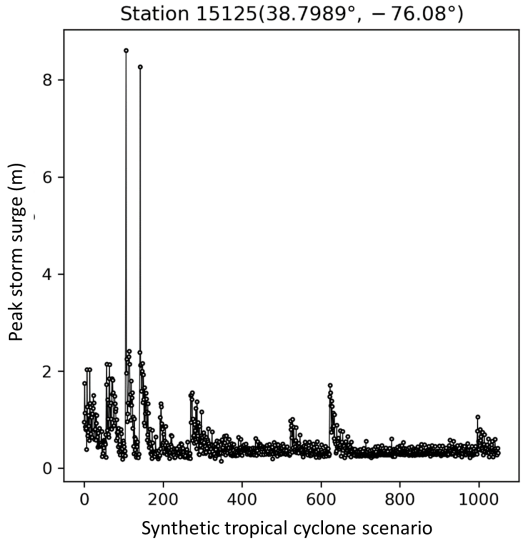

Figure C.4: Peak storm surges of station 15125.

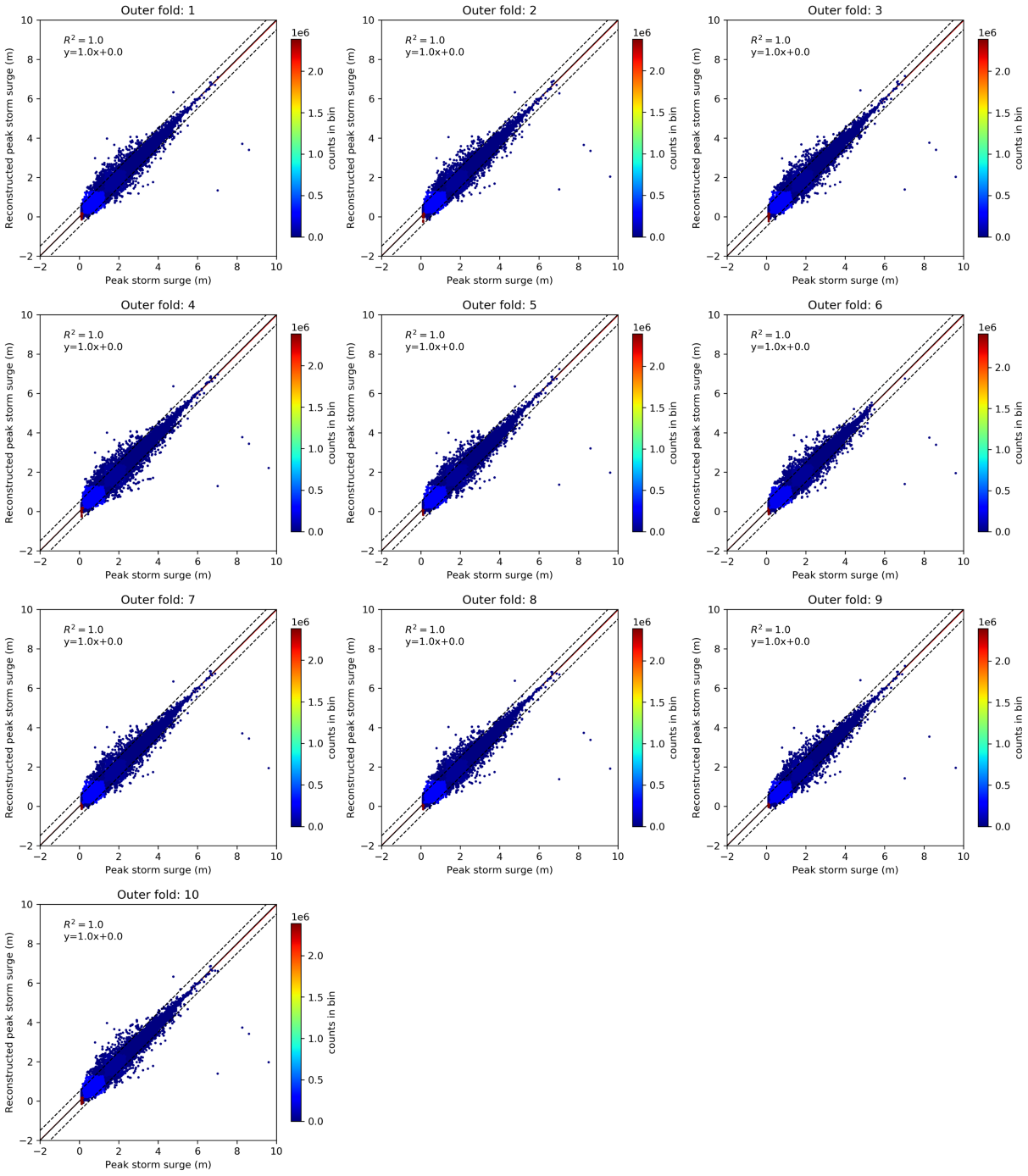

Figure C.5: Comparison between the peak storm surges of NACCS (x-axis) and the peak storm surges reconstructed using five principal components (y-axis) for each outer fold. The black line represents the equal line, the black dashed lines indicate ±0.5 m about an exact match, and the red line is linear regression solution.